UNIVERSITÄT PADERBORN
Die Universität der Informationsgesellschaft

Fakultät für Naturwissenschaften - Department Physik

Coherent Optoelectronic Control of Single Excitons

Dem Department Physik der Universität Paderborn zur Erlangung des akademischen Grades eines Doktors der Naturwissenschaften vorgelegte

Dissertation

von **Dipl.-Phys. Steffen J. Michaelis de Vasconcellos**

Paderborn, 2009

Promotionskommission

Prof. Dr. Torsten Meier (Vorsitzender)
Prof. Dr. Artur Zrenner (1. Gutachter)
Prof. Dr. Cedrik Meier (2. Gutachter)
Dr. Christof Hoentzsch

Tag der Einreichung: 18. November 2009

Tag der mündlichen Prüfung: 16. Dezember 2009

Zusammenfassung

Die kohärente Zustandsmanipulation eines einzelnen Quantensystems ist eine fundamentale Bedingung für die Herstellung von Geräten zur Quanteninformationsverarbeitung. In den letzten Jahren wurden dafür viele verschiedene Qubit Implementierungen vorgeschlagen und deren grundlegende kohärente Kontrolle konnte demonstriert werden. In Bezug auf die Wechselwirkung mit Photonen ist das Exziton-Qubit von besonderem Interesse für Anwendungen im Bereich der kohärenten Optoelektronik. Bisher wurde die kohärente Kontrolle dieses Qubit Systems im Wesentlichen mit ultraschnellen Laserpulsen realisiert. Insbesondere Einzel-Quantenpunkt Photodioden wurden dabei für eine Reihe kohärenter Experimente verwendet, zum Beispiel zur Untersuchung von Rabi-Oszillationen und Ramsey-Fringes, sowie der Demonstration einer CROT Quantengatter Funktionalität.

In dieser Arbeit wird ein neues Schema zur kohärenten optoelektronischen Manipulation eines Exziton-Qubits entwickelt. Dieses Schema verwendet einen optisches Takt und ein dazu synchrones, elektrisches Signal, das die kohärente Manipulation steuert. Die experimentelle Realisierung kombiniert dabei moderne Pikosekunden-Lasertechniken mit synchroner elektrischer Operation im kohärenten Regime. Die Experimente werden an einem einzelnen Exziton in einem InGaAs-Quantenpunkt in einer GaAs-Photodiode durchgeführt.

Zur Bestätigung der experimentellen Daten wurde ein detailliertes theoretisches Modell entwickelt. Diese Modell basiert auf den optischen Blochgleichungen und beinhaltet einen 2-Stufen Relaxationsmechanismus, der charakteristisch ist für den Tunnelprozess des Exzitons aus einem Quantenpunkt in einer Photodiode. Zur Überprüfung des Modells wurden die Simulationsergebnisse mit den Daten von früher entwickelten Experimenten verglichen. Das vorgestellte Modell erlaubt dabei eine tiefergehende Analyse der früheren Ergebnisse als es bisher möglich war. Desweiteren wird im Rahmen des Modells die leistungsabhängige Dämpfung der Rabi-Oszillationen bei tiefen Temperaturen untersucht.

In dieser Arbeit werden außerdem noch CdSe/ZnSe Quantenpunktphotodioden eingeführt. Dieses Materialsystem besitzt ein höheres Einschlusspotenzial für das Exziton und größere Coulombkorrelationsenergien als das InGaAs/GaAs System und ist daher ein Kandidat für kohärente Manipulationen bei erhöhten Temperaturen. Die Ergebnisse der spannungsabhängigen Photolumineszenz deuten an, dass es möglich ist CdSe/ZnSe Photodioden herzustellen mit denen weitere kohärente Experimente durchgeführt werden können.

Abstract

The coherent state manipulation of single quantum systems is a fundamental requirement for the implementation of quantum information devices. In the past, many different qubit implementations have been proposed, and basic coherent control has been demonstrated. Concerning the interaction with photons, exciton qubits are of particular interest for coherent optoelectronic applications. Until now, coherent manipulations of exciton qubits in semiconductor quantum dots have been performed mostly by ultrafast laser pulses. In particular, single quantum dot photodiodes have been used for a variety of coherent experiments, for example Rabi-oscillations, Ramsey fringes, and CROT quantum gate operation.

In this work, a new scheme for the coherent optoelectronic manipulation of an exciton qubits is developed. The scheme employs an optical clock signal and a synchronous electric gate signal, which controls the coherent manipulation. The experimental realization combines state of the art picosecond laser techniques with synchronous electric operation in the coherent regime. The experiments are performed using a single exciton, confined in a InGaAs QD in a GaAs photodiode.

To verify the experimental data, a detailed theoretical model is developed. The model is based on the optical Bloch equations and includes a two-step relaxation mechanism, which is characteristic for the tunneling of the quantum dot exciton in a photodiode. To confirm the model, results from previously developed experiments are compared to the model. Thereby, the model allows a more detailed analysis of the previous results. In particular, the evaluation of the heavy-hole tunneling time from the cw saturation spectroscopy is now more reliable. Furthermore, detailed analysis of the excitation dependent damping of the Rabi-oscillations at low temperature is given in the context of the theoretical model.

In this thesis, also CdSe/ZnSe QD photodiodes are introduced. This material system provides higher confinement and Coulomb correlation energies than the InGaAs/GaAs system and therefore is a candidate for coherent operation at elevated temperatures. The results of the voltage dependent photoluminescence measurements indicate, that it is possible to provide working CdSe/ZnSe QD photodiodes for future coherent photocurrent experiments.

Contents

1 Introduction

Richard Feynman's famous talk "There's plenty of room at the bottom", given 50 years ago at the annual meeting of the American Physical Society in 1959,[1] is maybe the earliest propose to use the laws of quantum mechanics for building a computer:

> *When we get to the very, very small world—say circuits of seven atoms—we have a lot of new things that would happen that represent completely new opportunities for design. Atoms on a small scale behave like nothing on a large scale, for they satisfy the laws of quantum mechanics. So, as we go down and fiddle around with the atoms down there, we are working with different laws, and we can expect to do different things. We can manufacture in different ways. We can use,* not just circuits*, but some system involving the* quantized energy levels*, or the* interactions of quantized spins*, etc.*

With this talk Feynman had set a big challenge, although nobody at this time had a clue how it should be possible to gain control over single quantum systems or to compute with them. Nevertheless, the idea of miniaturization was, is, and probably will be one of the dominating topics in applied science in the 20th and 21st century and remarkable achievements have been made.

Semiconductor technology thereby played a key role and the continuous advances in this field led to smaller and smaller and ever faster devices; in 2009 microprocessors with a structure size of 32 nm and clock speeds beyond 3 GHz are in mass production,[2] and chips with even smaller structure sizes are announced to be available in 2011.[3] These current semiconductor devices are primarily based on 'classical' physics, where all currents can be regarded as a continuous charge distribution. However, the quantum properties of nanostructured semiconductors will surely play an important role in future miniaturization steps. The challenge for future developments will therefore be to combine the conventional design with the quantum effects.

For optoelectronic applications, as well as for fundamental research, low dimensional semiconductor structures have attracted a lot of attention. Since the early 1970s, molecular beam epitaxy (MBE)[4] enabled to grow low dimensional semiconductor structures with an outstanding high precession and quality.

The reduction of the degree of freedom of the charge carriers in one of more dimensions influence significantly the density of states in these structures. This unique possibility led to the development of new devices like the quantum well laser[5] and the discovery of fundamental effects like the quantum Hall effect in a two-dimensional electron gas.[6]

Nowadays it is possible to fabricate semiconductor structures, which exhibit a confinement of the charge carriers in all three spacial dimensions. These zero dimensional (0D) objects are

called quantum dots (QDs) and have been intensively studied within the last two decades. The three dimensional confinement in a QD results in the appearance of discrete 'atomic-like' energy levels, making QDs interesting object for different optoelectronic devices like QD lasers,[7–9] photodetectors,[10] QD enhanced solar cells,[11] and most recently proposed QD-based terahertz optoelectronic devices.[12]

Another amazing feature of QDs is, that they can provide access to a single quantum system, incorporated in a solid state device. This single quantum system can be, for example, the spin of a single electron or an exciton, which is used in this thesis. The possibility to access and control a single quantum system has become of particular importance in the context of quantum information processing (QIP). QIP "is the study of the information processing tasks that can be accomplished using quantum mechanical systems"[13] and has been established as a new concept in theoretical computer science and physics.

The ultimate goal of quantum information science is the creation of an universal quantum computer which would be capable to run quantum algorithms to solve some mathematical problems, such as factoring exponentially faster than the best known algorithm running on a classical computer. A quantum computer consist basically of quantum bits (qubits), represented by a single (two-level) quantum system, and quantum logic gates, which manipulate one or more qubits in a coherent fashion. Today there are a few physical implementations of quantum computers, but only with a very limited number of qubits. The maybe most exciting demonstration of a quantum computer was the implementation of Shor's factoring algorithm using nuclear magnetic resonance to factorize $15 = 3 \cdot 5$.[14] Unit now it is really doubtful whether it will ever be possible to build a system with hundreds or thousands of qubits, which seems to be the requirement for an effective quantum computer.

However, other parts of the quantum information technology, like quantum cryptography have reached first commercial applications. Quantum cryptography, also known as quantum key distribution (QKD), guarantees a secure communication between two parties by using the quantum mechanical properties of a (single) photons (e. g. by using the BB84 protocol[15]). Up to now only point-to-point connections have been established, limited to less than 200 km. A big step forward will be a quantum communication network, which requires a quantum repeater. This device is essentially a small (few qubit) quantum computer with a single photon in- and output.

In this thesis the coherent optoelectronic control of a single exciton is studied. The exciton is confined in a QD and, in the context of QIP, can be regarded as a qubit. The exciton qubit provides an excellent coupling to the light field, thus allowing for ultrafast control of its population with resonant picosecond laser pulses. Previously, it was demonstrated that the qubit can reach every quantum state if it is coherently controlled by laser pulses with a defined phase, intensity, and detuning. The highlight of the work presented here is the demonstration of the coherent control of the quantum phase of an exciton qubit by electric interaction. The new scheme employs an optical clock signal and a synchronous electric gate signal, which controls the coherent manipulation. In principle, this approach can easily be scaled to parallel optical clocking of an array of single quantum systems with individual electric control by functional gate pulses, which is an important step forward for future quantum devices.

Outline of This Thesis

This thesis starts with an introduction into the physics of self-assembled quantum dots in chapter two. The basic properties of these quantum dots are discussed, regarding growth methods, basic optical properties, and spectroscopic methods. The chapter closes with a short review of the basic properties of InGaAs/GaAs single quantum dot photodiodes.

The basic concepts of quantum computation and quantum information processing are briefly explained in chapter three, to set a fundament for the further discussion in the next chapters.

In chapter four the details of the experimental setup are explained.

The results from photoluminescence experiments on CdSe/ZnSe QD photodiodes are presented in in chapter five. This research has been done in a close collaboration with Marina Panfilova from the group of Prof. K. Lischka.

The theoretical model derived in chapter six is one main part of this work. It describes the exciton two-level system in a single quantum dot. The model is based on the optical Bloch equations, but in order to model the exciton system in a quantum dot quantitatively, the basic equations are extended by a phenomenological approach.

In order to confirm the theoretical model, it is compared to cw and coherent experiments, performed by photocurrent spectroscopy. In chapter seven the outstanding coincidence between the theory and the experiment is presented.

The highlight of this thesis is presented in chapter eight, where the coherent optoelectronics control of an exciton is demonstrated.

A conclusion of the results and achievements of this work, together with an outlook presenting the perspective of furture investigations based on this work is given in chapter nine.

2 Fundamental Remarks on Quantum Dots

Quantum dots are semiconductor nanostructures who exhibit a three dimensional confinement for charge carriers. This results in the formation of discrete energy levels, similar to those of single atoms. Within the last two decades a large variety of different quantum dot systems has been investigated by research groups all over the world. The presumably three most important systems are gate defined quantum dots, colloidal quantum dots, and self-assembled quantum dots (figure 2.1):

- QDs defined by gate structure above a two dimensional electron gas (2DEG) are very often used for quantum transport measurements.[19] These structures provide the possibility to fill the QD deterministically with electrons and to control a single electron spin coherently.[20]
- Colloidal QDs are synthesized from precursor compounds dissolved in solutions by a self-organizing process. They possess good optical properties, although the surface may lead to disadvantageous effects (e.g. blinking). These QD can be incorporated in different materials, and are especially useful in bio-medical applications.[17,21] As recently shown by the group of K. Lischka, it is also possible to incorporate colloidal QDs into epitaxial grown structures.[22]
- Self-assembled quantum dots (SAQD) are grown by MBE. They can be fabricated with an amazingly low defect density and in a couple of different material systems. They are the most commonly used system for optical and optoelectronic investigations so far.

Within this thesis, mainly coherent experiments on excitons in self-assembled InGaAs/GaAs QD are discussed. Additionally, in Chapter 5, basic investigations on CdSe/ZnSe quantum dots, incorporated in the intrinsic region of a photodiode, are presented.

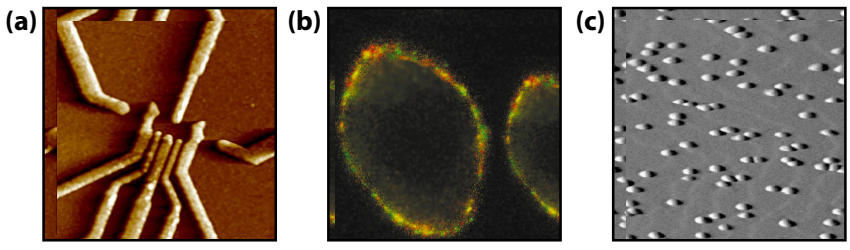

Figure 2.1: (a) Gate defined QD.[16] (b) Colloidal QDs labeling cell microtuboles.[17] (c) AFM image of a sample with self-assembled QDs.[18]

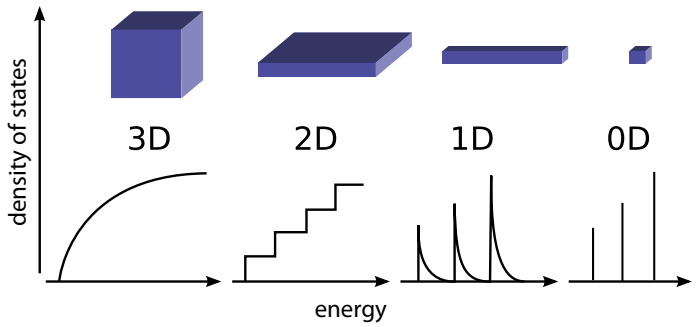

Figure 2.2: Density of states of the conduction band for different geometries (figure according to [25])

2.1 Self-Assembled Quantum Dots

2.1.1 Fabrication

Self-assembled quantum dots are usually grown by MBE in the Stranski-Krastanov growth mode.[23] For the formation of quantum dots during heteroepitiaxial growth, materials with different lattice constants are necessary. The process starts with the epitaxial growth of a thin two-dimensional layer (wetting layer, WL) on top of the host material. When a critical thickness is reached, the accumulated strain is released by the formation of coherently strained small islands. Afterwards, the islands are overgrown by the host material. This formations process leads to islands that are almost free of defects and have a very high optical quality. The size of the islands, their position and density are subjects to statistical distributions.

In practice, the island formation process depends critically on many different parameters, for example the substrate temperature and the growth rate. By changing the growth parameters, the statistical distributions of position, density and size of the quantum dots can be influenced within certain constraints. A lot of experience is necessary to fabricate high quality samples.

There are several approaches to overcome the issue of randomly positioned quantum dots. They mostly rely on pre-structuring of the sample, for example by focused ion beam (FIB) implantation end etching, prior to the Stranski-Krastanov growth, which leads to a more controlled growth.[24]

2.1.2 Energy States of Self-Assembled Quantum Dots

Creating a confinement in one or more dimension of a semiconductor results in a drastic change of the density of states of the conduction and valence band, as schematically shown in figure 2.2. In the zero dimensional system (QD), the density of states is represented by δ-functions, analogous to the states of an atom.

A concrete theoretical calculation of the energy states is very difficult, because the energy spectra depend strongly on the QD geometry and potential barrier, which both are influenced by the growths conditions. However, by assuming very simple geometries a model system which allow for a good qualitative insight into the physics of QDs can be derived.

For self-assembled quantum dots commonly a lens shape geometry is assumed. Thereby, the dimension in growth direction (z-direction) is significantly smaller than the lateral dimensions. This means that the wave function of the electron is strongly confined to the lowest subband of the narrow quantum well of the WL.[26] Higher subband states can be neglected. In the lateral dimensions the confinement potential can be assumed to be harmonic. Usually, the potential is not equal in x and y direction due to a small asymmetry in the QD shape and crystal structure. The resulting energy splitting is called fine structure splitting (FSS). Therefore, the energy levels equal those of an anisotropic two-dimensional oscillator with the two quantum numbers n_x and n_y:[27,28]

$$E_{n_x,n_y}(\delta) = \hbar\omega\left[(n_x + 1/2)\sqrt{\delta} + (n_y + 1/2)/\sqrt{\delta}\right] \tag{2.1}$$

The ratio $\delta = \omega_x/\omega_y$ denotes the asymmetry. For the symmetric case ($\delta = 1$) the energy states are $(N + 1)$-fold degenerated, with $N = n_x + n_y = 0, 1, 2, \ldots$ Each state has a twofold spin degeneracy, and so, respecting the Pauli principle, the shells can be filled with $2, 4, 6, \ldots$ electrons. Analogous to atomic physics the energy levels are classified by their total angular momentum $L = |n_x - n_y| = 0, 1, 2, \ldots$ as s-, p-, d-,…shell.

For the hole states, all of the above assumptions are also valid. Additionally, it has to be taken into account that the valence bands of the light and heavy holes are degenerated at the Γ-point of the Brillouin zone in a bulk semiconductor. But for the lower energy levels of the QD, only the heavy holes are relevant, because the quantization energy depends on the effective mass.

When filling the QD with electrons and holes, the Coulomb interactions between the charge carriers have to be considered. These interaction leads to a renormalization of the single particle energy levels.

2.1.3 Excitons in Self-Assembled Quantum Dots

Subject of interest in optical spectroscopy of QDs are (most commonly) excitons. The simplest occupancy that can be assumed is the uncharged *exciton*, often denoted with X or $1X$. It is formed by an electron in the conduction band and a hole in the valence band (figure 2.3(a)). When electron and hole both occupy the s-shell, this state is called single exciton ground state. This state will be of special importance throughout the whole thesis, because when using resonant excitation, this state can be regarded as a two-level system.

The exciton can also be created in excited states, where, for example, electron and hole occupy a state in the p-shell, as shown in figure 2.3(b). The excited exciton states underlie a fast relaxation (ps-timescale) into the exciton ground state.[29]

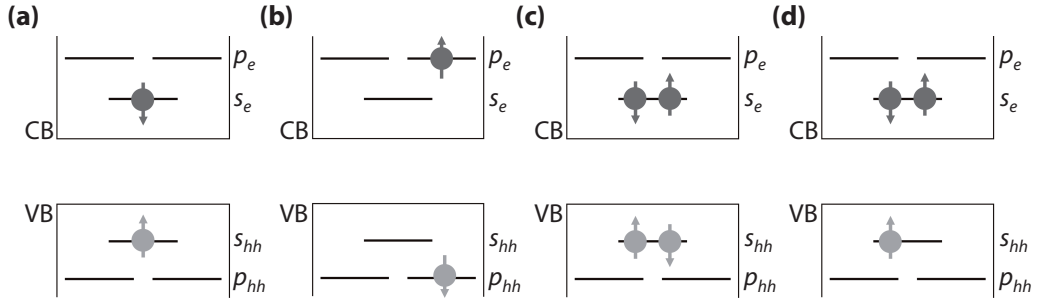

Figure 2.3: Schematic illustration of different QD occupations: (a) Exciton (X), (b) p-shell exciton(X_p), (c) Biexciton ($2X$), (d) Single charged exciton (X^-)

If a second exciton is confined in the QD this exciton complex is called *biexciton* (XX or $2X$). As the s-shell is two-fold spin degenerated, both excitons can occupy the same shell (figure 2.3(c)). In an optical spectrum, the recombination of the second exciton (in presence of the first one) is labeled as biexciton line. Due to the renormalization by the exciton-exciton binding energy, this line appears most often at a lower energy than the single exciton line. In self-assembled InGaAs QDs this line has typically an energetic difference to the transition of the single exciton ground state of 2-3 meV. In CdSe QDs, the binding energy is much higher. Here an energetic difference of 20-25 meV is typical.[30]

When confining an additional electron in the quantum dot, the transition energy of the exciton is also shifted due to Coulomb and exchange interactions. The exciton-electron complex is then called *negatively charged exciton* X^-. Adding more than one electron, higher charged excitons are created $X^{2-}, X^{3-}, \ldots$ When holes are confined instead of electrons, the exciton complexes are called, *positively charged excitons* X^{n+}. The single charged exciton (X^-) is illustrated in figure 2.3(d).

For the resonant excitation of an exciton, as well as for the spontaneous emission of a photon, optical selection rules apply. Optical dipole transitions require a change in the total angular momentum of ±1. Therefore, one has to take into account the total angular momentum of the involved valence and conduction band: The heavy hole band is characterized by the total angular momentum $j = 3/2$, i. e. $m_j = \pm 3/2$, while the conduction band is characterized by $j = 1/2$, i. e. $m_j = \pm 1/2$.[31] Therefore, in the first order optical interband transitions are only allowed between QD levels that have the same angular momentum (i. e. from the same shell, e. g. $s_{hh} \rightarrow s_e$). Regarding the quantum number m_j, only combinations of electron and hole resulting in a total spin of ±1 are optically allowed. This spin can be transferred by a circular polarized photon. Those combinations resulting in a total spin of ±2 cannot couple to the light field, and therefore are called *dark* excitons.

2.2 Quantum Dot Spectroscopy

For a single QDs, discrete optical transition lines are expected due to its discrete energy structure. However, if an ensemble of hundreds up to several ten-thousands QDs is investigated, the spectrum shows an inhomogeneously broadened distribution of superimposed peaks. This results from the statistical size distribution due to the self organized growth, since the size of the QD directly influences the transition energy of its excitonic states. The full width at half maximum (FWHM) of the optical emission of the ground state transitions of an ensemble of QDs depends strongly on the material system and the growth conditions. A typical value for InGaAs QD is 100 meV, whereas narrow broadenings down to 18.4 meV have been achieved for this material system.[32]

In many situations—and also in this thesis—it is desirable to investigate a single QD. This requires, as a matter of fact, a sample with a low areal QD density of $10^{10}\,\mathrm{cm}^{-2}$ (= $100\,\mu\mathrm{m}^{-2}$) or less. Further, the investigated region of the sample must be restricted to a region of 0.1-1 $\mu\mathrm{m}^2$, which can be achieved by a near field shadow mask in combination with a μ-photoluminescence setup. The shadow mask consists of a nontransparent aluminum layer with holes of a few 100 nm in diameter and is usually fabricated by e-beam lithography and wet or dry etching. By using a μ-photoluminescence setup with a very high spatial resolution it is possible to investigate single QDs even on unstructured samples, if they exhibit an extremely low QD density (1 QDs/μm and less). However, even on those samples it is advantageous to use a shadow mask to relocate the same QD from time to time. In the following the major methods of QD spectroscopy on single QDs are briefly introduced.

2.2.1 Photoluminescence and Electroluminescence

A very basic characterization method and most commonly used is the photoluminescence (PL) spectroscopy. Thereby, charge carriers are excited by a laser, whose energy is (usually) above the band gap of the host material. The charge carriers subsequently relax into the lowest energy states of the QDs followed by a spontaneous emission. The relaxation process is very fast, which means that nearly all charge carriers relay into the lowest energetic states before they recombine. With classical PL spectroscopy one can therefore only observe the electronic ground states. The number of the charge carriers, which can relax into the QD, is subject of a Possionian statistic. By recording the PL versus the incident power, it is possible to distinguish between the exciton and biexciton transitions, because the intensity of the latter one increases stronger with increasing excitation power.

It is also possible to record the PL signal with a time-resolving method to determine the radiative recombination time. Hereby the sample is excited with a short laser pulse and the subsequent PL is recorded with a streak camera or another time-resolving detector.

When the QDs are embedded in a p-i-n-diode structure, it is possible to inject electrons and holes directly into the QDs. By modern lithography techniques structures with an active region of less than 1 $\mu\mathrm{m}^2$ can be created, which allow for investigations on a single QD.[33,34] The resulting *electroluminescence* spectra are comparable with PL spectra.

2.2.2 Absorption Techniques

The traditional PL method has some drawbacks. Especially, excited (single) exciton states of a QD do not appear in the PL spectrum due to the fast relaxation into the ground state. To gain access to these states, absorption techniques have to be applied. Furthermore, accessing the coherent quantum properties of excitons in QDs is not possible with the PL technique due to the incoherent relaxation process. For coherent measurements the exciton state under investigation therefore has to be excited resonantly, usually by ultrafast laser pulses. To determine the quantum state after the coherent excitation, different methods have been developed. A couple of these methods utilize the signal of the inherent decay of the exciton to measure the population of the exciton two-level system.

The basic PL method can be enhanced to a *photoluminescence excitation* (PLE) measurement, which is basically an absorption method. Thereby the luminescence of the QD exciton ground state (or, depending on the structure of the sample, of charged exciton states) is detected while the excitation energy is tuned through the region of the excited states. If the excitation is in resonance with an excited exciton state, an exciton will be created and subsequently relax into its ground state and recombine. The technique is quite simple to integrate into an existing PL setup, as it has been done in our lab.[35] Besides the energetic position of the excited exciton states, also information about the relaxation process is in principle accessible. A big advantage of the PLE spectroscopy is, that other QDs, which might also absorb light, do not contribute to the signal.

For excited states the detection of the luminescence of a lower state can be used in coherent experiments, which is a common method.[35,36] However, it seems hardly possible to access the coherent properties of the exciton ground state with an all-optical method, because in this case the resonant excitation is superimposed with the radiative decay of the exciton. Nevertheless, R. Melet et al. have recently observed Rabi oscillations of the exciton ground state in a rather complicated all-optical experiment by combining spatially resolved spectroscopy with a 1D waveguiding geometry (see figure 2.4b).[37]

Beside these techniques, direct absorption measurements of a single QD have been carried out by several groups. The absorption of a single QD is very weak (about 0.1% of the incident light is absorbed at resonance), therefore usually a differential measurement method has to be used (e. g. Stark shift modulation,[38,39] optical modulation,[40] etc.). With this direct absorption method the ground state as well as the excited exciton states can be investigated and parameters like the microscopic oscillator strength can be evaluated quantitatively. Therefore the results of this method can be very well compared to theoretical calculations.

A more complex, but very powerful method is the Four-Wave Mixing (FWM) technique (figure 2.4a), which is often used to investigate the coherent properties of quantum dot ensembles. The dephasing dynamics of different exciton states in QDs can be investigated by using a sensitive transient FWM technique in heterodyne detection. By combining the technique with a polarization control of the excitation pulses, Borri et al. achieved to measure fine-structure splittings and biexciton binding energies with high accuracy.[41] With the FWM,

it is possible to observe Rabi oscillations of the ground state exciton in a QD ensemble.[42] Langbein et al. also used the technique to investigate individual quantum systems.[43,44]

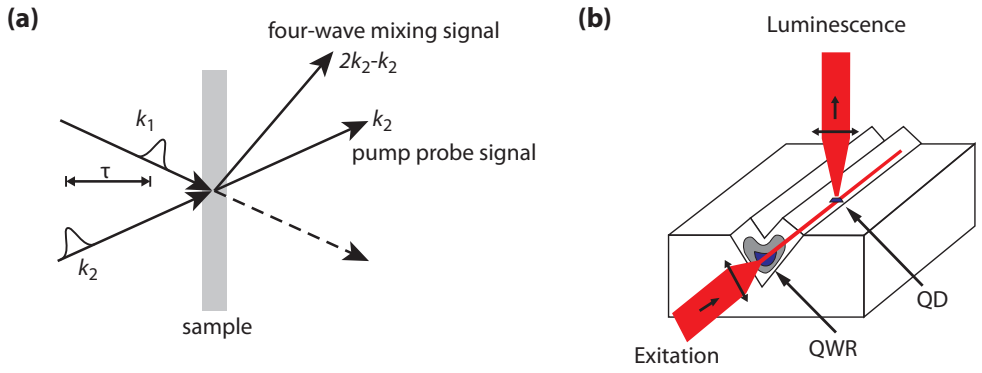

Figure 2.4: (a) In a FWM experiment the diffracted signal is detected, while in a pump-probe experiment the linear response is measured (figure derived from [31]). (b) Using a guided excitation through a quantum wire, R. Melet et al. observed Rabi-oscillations of the ground state in an all-optical experiment (figure taken from [37]).

2.2.3 Photocurrent Spectroscopy

Another important absorption technique—and the key technique in this work—is the *photocurrent spectroscopy*. Thereby the QD is again resonantly excited, but instead of a radiative recombination, the charge carriers are forced to tunnel out of the QD and contribute to a photocurrent (PC) which is detected with a high resolution current measurement.[45,46] Compared to the other absorption techniques, the optical setup is very simple because only the excitation has to be focused onto the sample and neither the luminescence nor the transmitted light has to be collected. The largest restriction of the method is the necessity of an appropriate sample structure. The QD has to be incorporated into a photodiode structure (usually a n-i-Schottky diode or a p-i-n diode), which allows to apply an electric field with a strength that the charge carriers can tunnel out from the QD, as explained later in section 2.3.2. The detection efficiency of the current measurement is nearly 100%, so that the signal strength primarily depends on the ratio between tunneling and radiative recombination. To acquire the spectral shape of a resonance, it is—in principle—possible to tune either the excitation energy or the exciton energy (e. g. via the Stark shift), but the later one usually provides a much higher spectral resolution (here less than 0.5 μeV).

The method is capable to investigate the ground state and the excited states of excitons, but it is most often only applied to the ground state. The real strength of the photocurrent method is its application in the coherent spectroscopy, where it allows for a quantitative measurement

of the quantum state of the exciton. A detailed theoretical model of the PC from a single QD is presented in chapter 6.3.2.

2.3 Single Quantum Dot Photodiodes

Incorporating quantum dots into the active region of a photodiode structure allows for optical and electrical access to the exciton in a single QD. In this section the basic (incoherent) properties of such a device are presented using the example of the well understood InGaAs QD photodiode.

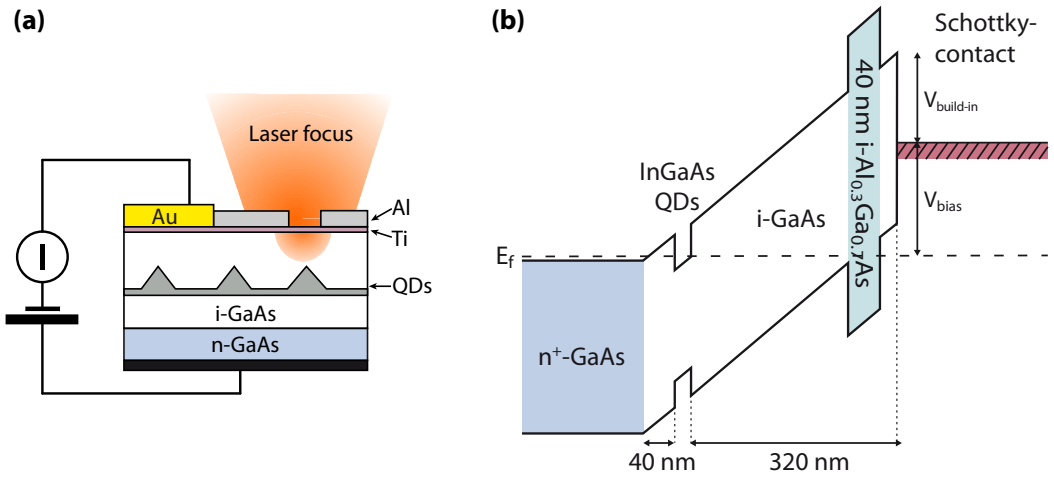

Figure 2.5: (a) Schematic layer structure of a GaAs Schottky photodiode with InGaAs QDs embedded in the intrinsic region. (b) Band diagram of the GaAs photodiode used in this work with an applied reverse bias voltage.

2.3.1 Sample Structure and Electric Field

The photodiode structure is basically always the same. Figure 2.5 shows the schematic structure of a typical photodiode. Above highly doped back contact, an intrinsic layer is grown. On top of this layer a Schottky contact is processed. The QDs are embedded in the intrinsic region during the growth. To address only a single QD by the laser excitation, a near field shadow mask restricts the excitation region.

An important feature of the QD photodiode is, that it is possible to apply a vertical electric field to the quantum dot. For a n-i-Schottky diode with a highly doped back contact, the electric field can be calculated as a function of the bias voltage V_{bias} and the distance d between

the back contact and the Schottky contact:

$$F = \frac{V_{build\text{-}in} + V_{bias}}{d} \tag{2.2}$$

The build-in voltage of the Schottky diode is approximately half of the band-gap; for a GaAs Schottky diode with a titanium Schottky gate $V_{build\text{-}in} = 0.75\,V$ is presumed. The formula is only correct for moderate voltages and as long as there is no current flow and no charges are trapped inside the QDs or the wetting layer, so a careful treatment is necessary. However, for the interesting reverse bias voltage region (here between 0 V and 2 V) the equation can certainly be applied.

2.3.2 Tunneling

If a QD is located in the intrinsic region of a photodiode, an exciton in the QD can decay via two competing processes: radiative recombination and tunneling. The radiative recombination time (for InGaAs QDs about 400-600 ps) of an exciton in a small QD (i.e. a QD with a small height) does not depend very strongly on the electric field, and can here assumed to be a constant for a specific QD. Instead of recombining, the electron and hole can tunnel through the barrier to the back contact or the Schottky contact, respectively (see figure 2.6). The tunneling time depends on the barrier—which is strongly field dependent—and on the effective mass of the charge carrier. The tunneling time of the electron and the (heavy) hole can differ by a factor of more than 10, because the hole has a much higher effective mass. Nevertheless, after the electron (which has the shorter tunneling time) has tunneled, the single hole has no counterpart to recombine and therefore tunnels subsequently. A rough estimation of the dependencies of the tunneling rate can be given by the Wentzel-Kramer-Brillouin approximated expression

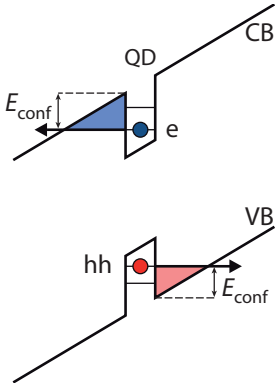

Figure 2.6: Tunneling of electron and hole from a QD.

$$\frac{1}{\tau_t} = \frac{\hbar}{8m^* a^2} \exp\left(\frac{-4\sqrt{2m^*}}{3eF\hbar}(E_{conf})^{3/2}\right), \tag{2.3}$$

but neither the confinement energy E_{conf} nor the height of the QD a can be measured directly and small variations of these parameters result in a considerable change of the tunneling time. However, the dependence of the tunneling time from the external field $1/\tau_t \propto \exp(-1/F)$ depicts the experimental results very well.

The ratio between tunneling decay and radiative recombination is simply determined by the according time constants. At a certain electric field, the tunneling time becomes shorter

than the radiative recombination time. This means, that the probability of the exciton to tunnel from the QD becomes greater than the a radiative recombination.

2.3.3 Quantum Confined Stark Effect

The quantum confined Stark effect (QCSE) is an essential effect for the photocurrent spectroscopy. It enables the tuning of the energy of the exciton ground state (of course, other states are also effected) via the bias voltage with a very high accuracy. It is a well known effect in QDs, and also in quantum wires[47,48] and quantum wells.[49–51] Here only the influence of an electric field $\boldsymbol{F}$ in vertical (z-)direction is discussed, as the lateral field remains constant in the photodiode structures. Therefore, the treatment of the QCSE in QDs is analogous to that of a quantum well.

As mentioned above in section 2.1.2, only the lowest energy state of the quantization in z-direction is taken into account. As an intuitively explanation, the wave functions of electrons and holes in a QD are shifted and slightly deformed by the electric field, as schematically shown in figure 2.7. For moderate field strength and depending on the polarizability α, a field induced dipole moment $\boldsymbol{\mu} = \alpha \boldsymbol{F}$ is induced which results together with the permanent dipole moment $\boldsymbol{\mu}_{\mathrm{el}}$ of the exciton in a reduction of the transition energy. In a first approximation, the decrease of the energy is therefore quadratic with increasing electrical field:

$$E_X = E_X(F = 0) - \boldsymbol{\mu}_{\mathrm{el}} \boldsymbol{F} - \alpha F^2, \tag{2.4}$$

where $\boldsymbol{\mu}_{\mathrm{el}}$ is the permanent dipole moment and α the polarizability.[52] This is only a coarse approximation, however it reflects the behavior of the QCSE in the InGaAs/GaAs QD photodiodes very well. For very high electric field, the induced dipole moment is limited due to the confinement of the electron and hole inside the dimensions of the QD. Then the QCSE is linear with increasing electric field.

For a more exact description, the reduction of the Coulomb-interaction (due to an increased

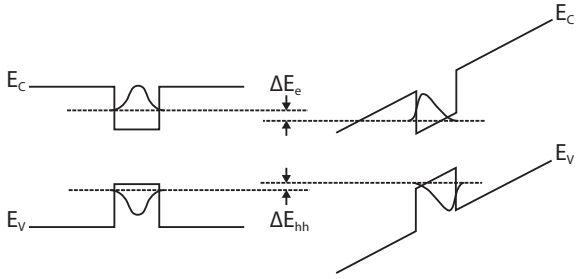

Figure 2.7: Deformation of the electron and hole wave functions due to the external electric field. Thereby, the transition energy of the exciton is reduced.

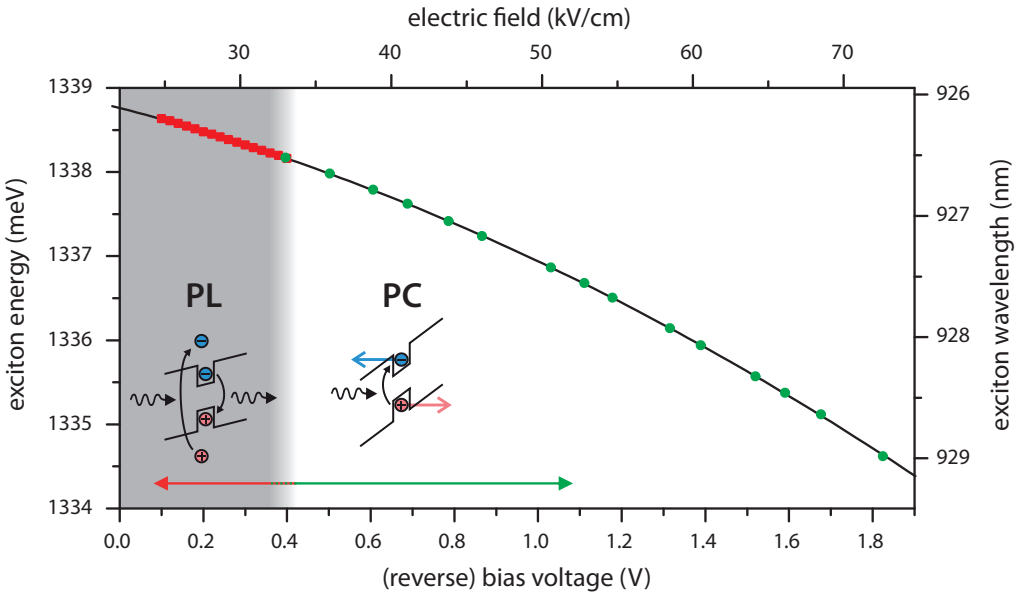

Figure 2.8: The QCSE of the exciton ground state, recorded in the photoluminescence and photocurrent regime. The experimental data is fitted with a parabola.

electron–hole distance) and the change of the quantization energy have to be taken into account. Thereby, a more complicated behavior can appear.[45,52–54]

The QSCE allows for a very accurate tuning of the transition energy; the adjustment fidelity depends only on the stability of the voltage source.[55] At lower electric fields (below 32 kV/cm), at which the optical recombination processes are dominating, the QCSE can be observed in the PL. At higher fields, the tunneling probability increases. Then the energy of the exciton transition can be measured by PC spectroscopy. Figure 2.8 shows the QSCE of a QD in the InGaAs/GaAs photodiode, which continuously covers the PL and PC region. Therein, the energy is plotted against the bias voltage, which is—referring to equation 2.2—proportional to the electric field.

2.3.4 Voltage Dependent Photoluminescence and Charging Effects

In a photodiode structure it is possible to investigate the PL in dependence of the applied bias voltage and the electric field, respectively. As explained above, thereby the energy of the exciton transitions are shifted due to the QCSE and the transition from the PL to the tunneling regime can be observed. In addition, one can observe a charging of the exciton due to tunneling of electrons into the QD at certain bias voltages. The mechanism behind this can be explain as follows. In thermal equilibrium, the Fermi level is determined by the

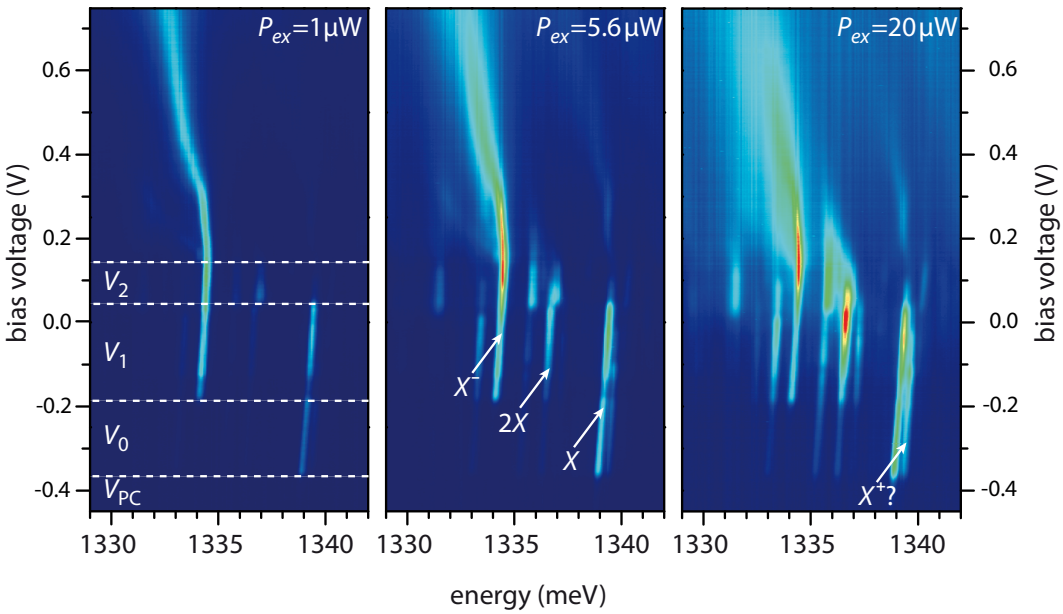

Figure 2.9: Voltage dependent photoluminescence of a single QD (some weaker line may arise from a different QD) at different excitation power. The color coding of the luminescence intensity is the same for all three diagrams.

n-doped back contact. By applying an external bias voltage V_{bias} the electron energy levels of the quantum dot can be shifted relative to the Fermi level. For increasing bias voltage the band flattens and the electron levels are subsequently shifted below the Fermi level of the back contact. This results in an occupation of the QD with electrons.[45,56–58]

A detailed discussion of the PLV spectra can be found in the dissertation of F. Findeis,[18] therefore only a brief description will be presented here. Figure 2.9 shows three color plots of the voltage dependent PL of a single InGaAs/GaAs QD (Sample 120799.2b δ), recorded for different excitation powers. The signal originates mainly from a single QD, but at higher excitation power contributions that may originate from a second QD are visible. The indicated excitation power can only be referred as relative power, because the reflection and absorption of the excitation by the µ-PL setup and the shadow mask is unknown.

In the bias voltage region V_{PC} (below -0.35 V), the luminescence of the QD if effectively quenced. Here all captured charge carriers tunnel from the QD before recombining. This is the voltage region where the photocurrent spectroscopy can be used to investigate the optical properties of the QD.

At low excitation power, between ca. -0.35 V and -0.2 V (region V_0) only one peak appears in the spectrum. It originates from the neutral exciton transition. Above -0.2 V (region V_1)

a second peak arises. In this voltage region the single electron state of the *s*-shell of QD is below the Fermi level of the *n*-doped back contact. Therefore, an electron can tunnel into the QD. Although the *s*-shell is two-fold degenerated, a second electron cannot tunnel into the dot, due to the Coulomb blockade. If now an electron-hole pair is captured, relaxes into the lowest energy state and recombines, the emitted photon has the energy of the X^- exciton. This states is separated by about 5 meV from the ground state. Further, it is also possible that a single hole is captured, resulting in the appearance of the neutral exciton state X also in this voltage region. Close to the ground state, about 0.5 meV above, an accompanying state is visible. This state could be tentatively assigned to the positive charge exciton X^+, created from the biexciton state $2X$ if one electron tunnels *out* from the QD.

The power dependence of the lines is an additional indicator for the identification of the states. With increasing excitation power a pronounced line arises at an energy, which is 2.7 meV lower than that of the ground state. The intensity of this line increases faster with the excitation power than the intensity of the ground state, which is a clear signature of the biexciton state $2X$.

Above a reverse bias voltage of about 0.05 V (region V_2), the two electron state is shifted below the Fermi level. Here two electrons can occupy the QD, and therefore the luminescence can be expected (at low excitation) from X^- (one hole capture) and X^{2-} (exciton capture). The neutral exciton cannot be created efficently, hence the line vanishes in this region. A doubtless assignment of the here appearing lines is very difficult and not subject of this thesis. At 0.15 V the signature of the spectrum changes again and especially the X^- becomes blurred with increasing bias voltage, possibly due to charging of the wetting layer.

2.3.5 High Resolution Photocurrent Spectroscopy

The basic principle of the photocurrent spectroscopy is the resonant absorption of photons and subsequent tunneling of the charge carriers from the QD. A cw Ti:Sapphire laser is tuned close to the resonance of the previously with PLV measurements analyzed QD. Then the exciton resonance is tuned through the laser energy by utilizing the QCSE.

The spectral line width of the laser is much smaller than the homogenous line width of the QD, therefore, the spectral resolution depends only on the tuning of the exciton energy by the bias voltage. In figure 2.10 the resonances of the neutral exciton X are recorded for different laser wavelengths. At low bias voltage the FSS is fully resolved, at high voltages the lines are lifetime broadened due to the faster tunneling and the FSS cannot be resolved any more. In the inset of figure 2.10 a highly resolved PC spectrum of the ground state is shown. The FSS can be resolved easily. The voltage scale on the top is converted to an energy scale via the QCSE. The peaks can then be fitted with a Lorentzian curve with a very good agreement.

The line width is influenced by two effect: the lifetime due to the tunneling and a power broadening. Both effects will be discussed in the theoretical section. The doublet line structure visible at low voltages can be further investigated by using a linear polarized excitation. On rotating the orientation of linear polarization each peak can be clearly suppressed with respect

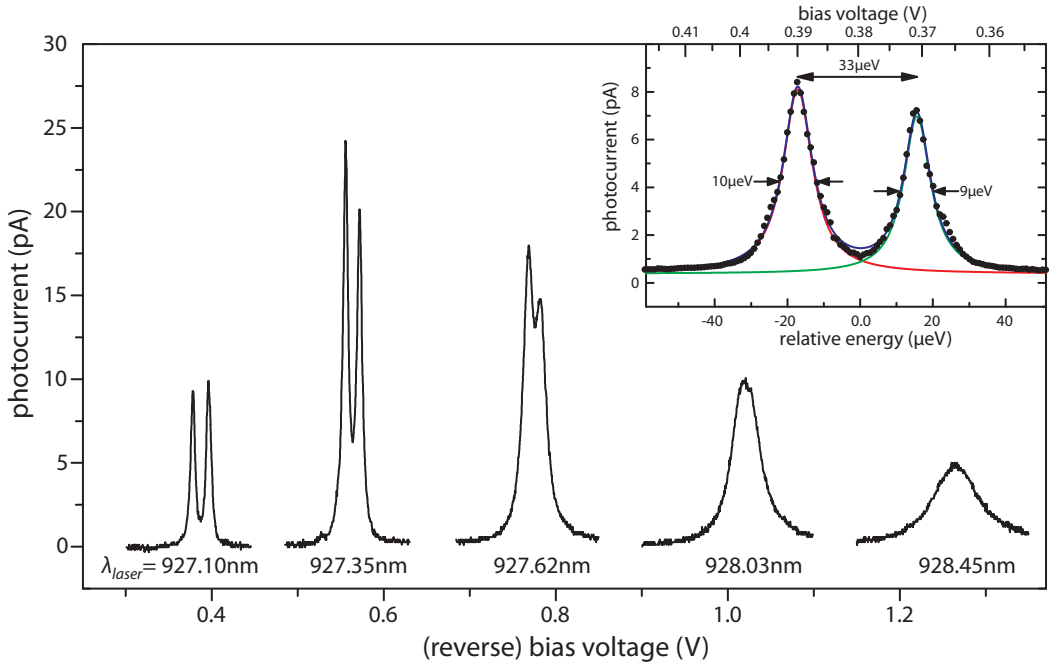

Figure 2.10: Photocurrent resonances of a single QD for different excitation energies. *Inset:* A highly resolved PC spectrum. The bias voltage scale on the top axis, is converted to the relative energy on the bottom axis via the QCSE.

to the other. This can be explained by a slight shape asymmetry, present in almost any self assembled QDs, resulting in an energy splitting caused by the electron–hole exchange interaction, which is commonly known as fine structure or asymmetry splitting in the literature (see section 2.1.2, and references [59, 60]).

2.3.6 Electrically Connected Quantum System

The single QD photodiode structure allows for optical and electrical access to a single quantum system, represented by an exciton in a QD. The new parameters, bias voltage V_{bias} and photocurrent I_{PC} allow for an electrical measurement of the occupancy of an optical isolated QD via the tunneling effect. At the same time, the energy of the exciton transition can be tuned by the quantum confined Stark effect. With resonant ps laser excitation of the (single) exciton ground state of the QD, the exciton state can be described as a two-level system.[(a)] Under these conditions, a single QD photodiode can be regarded as an unique coherent optoelectronic device, with the possibly of coherent optical and electrical control, as discussed later.

[(a)] A detailed description of this two-level system is given in chapter 6

3 Introduction into Quantum Information

The intention of this chapter is to give a brief overview about quantum information processing (QIP) and to define the basic terms used throughout this thesis. Good reviews of this field are given for example in the textbooks [13, 61–63].

3.1 Historical Overview

The roots of quantum information processing go back to the 1960s, when R. Landauer investigated the heat dissipation of logical operations. He found, that the only logical operations which require dissipation of energy are irreversible ones. Later on, C. Bennet discovered the possibility of reversible, dissipation-less computation and T. Toffoli invented the classical two bit CNOT and three bit Toffoli gate, whereas the latter is an universal gate for digital computation. This means, that all algorithms that can be solved by a Turing machine can be efficiently solved by a sequence of this gate. These developments are fundamental prerequisites for QIP, because in a quantum computer all quantum logical operations have to be reversal, else the quantum state is destroyed.

In the early 1980s, P. Benioff showed that it is possible to build a classical Turing machine by using a quantum mechanical Hamiltonian,[64] and R. Feynman proposed, that a quantum computer might be able to be more than a classical computer. He suggested, that such a computer would be especially useful to simulate the dynamics of another quantum system.[65,66] In 1985, the concept of a *universal quantum computer* was fully developed by David Deutsch.[67,68] He remarked, that such a computer includes a *quantum parallelism*, "a method by which certain probabilistic tasks can be performed faster by an universal quantum computer than by any classical restriction of it."[67] In 1991 he proposed the first quantum algorithm (Deutsch-Josza algorithm[69]), which demonstrated the theoretical advantage of a quantum computer over a classical computer.

The interest in quantum computation increased strongly in 1994, when P. Shor invented the first quantum algorithm which can factorize integers exponentially faster than the fastest known classical algorithm.[70,71]

Physical implementations for qubits have been proposed since the early 1990s in various different systems, e. g. in trapped ions, nuclear spins, flux quanta, polarized photons, excitons, etc., and exciting progress by experimental groups have been made. Nevertheless, the today achieved functionality is only rudimentary. New concepts for the coherent manipulation and interconversion of qubits have to be invented to establish quantum information as an useful and efficient technology.

3.2 Qubits

The building blocks of quantum information science are qubits. Unlike a classical digital bit, which can take only the two values "0"and "1", a quantum mechanical two-level system, here called *qubit*,[(a)] can exist in a complex superposition of its quantum mechanical states $|0\rangle$ and $|1\rangle$. The quantum state of a qubit can be mathematically written as a vector in a two-dimensional Hilbert space, given by

$$|\psi\rangle = \alpha\,|0\rangle + \beta\,|1\rangle\,, \tag{3.1}$$

where α and β are complex numbers that satisfy the condition $|\alpha|^2 + |\beta|^2 = 1$. Apart from a global, not measurable phase, this is equivalent to

$$|\psi\rangle = \cos(\theta/2)\,|0\rangle + e^{i\phi}\sin(\theta/2)\,|1\rangle\,, \tag{3.2}$$

where $0 \leq \theta \leq \pi$ and $0 \leq \phi < 2\pi$. Using this parametrization, the qubit state can easily visualized in spherical coordinates on the Bloch sphere, introduced in chapter 6. Thereby, the parameters θ and ϕ are corresponding to the altitudinal angle and the azimuthal angle, respectively.

Due to the fundamental laws of quantum mechanics, it is not possible to determine the complete information about the quantum state of a qubit. When measuring a qubit as defined in Equation 3.1, the *probability* to get either the result $|0\rangle$ or the result $|1\rangle$ is $|\alpha|^2 = \cos^2(\theta/2)$ and $|\beta|^2 = \sin^2(\theta/2)$, respectively.

In the next section it is described, how the quantum state of a single qubit can be manipulated. However, it is obvious, that for a functional quantum computer, more than one qubit is required. A two-qubit system has four basis states $|00\rangle$, $|01\rangle$, $|10\rangle$, and $|11\rangle$. The two-qubit system can also be in a superposition of these four states, thus the total quantum state is given by

$$|\psi\rangle = \alpha_{00}\,|00\rangle + \alpha_{01}\,|01\rangle + \alpha_{10}\,|10\rangle + \alpha_{11}\,|11\rangle\,, \tag{3.3}$$

where $|\alpha_{ij}|^2$ is the probability to get the result $|ij\rangle$ from a measurement of the two-qubit system in total. Of course it is possible to measure only one qubit of the two-qubit system. If, for example, one measures the first qubit and gets the result '$|0\rangle$', the system is left in the state

$$|\phi'\rangle = \frac{\alpha_{00}\,|00\rangle + \alpha_{01}\,|01\rangle}{\sqrt{|\alpha_{00}|^2 + |\alpha_{01}|^2}}. \tag{3.4}$$

A special and and important two-qubit state is the *Bell state* or *EPR pair*, given by

$$\frac{|00\rangle + |11\rangle}{\sqrt{2}}. \tag{3.5}$$

[(a)] The term *qubit* was coined by B. Schumacher in 1995.[72]

If one measures the first qubit of this state, one obtains '$|0\rangle$' with the probability of 1/2 leaving the two-qubit system in the post-measurement state $|00\rangle$, or '$|1\rangle$' with the probability of 1/2 leaving the system in the state $|11\rangle$. Thus, the measurement of the second qubit will always give the same result as the measurement of the first one. The Bell state is thereby the simplest example of *entanglement* and it cannot be written as a product of two one-qubit states. Such entangled states have applications in the *quantum cryptography* and *quantum teleportation*.

For an efficient quantum computer a large number of qubits, assembled in a *qubit register* is necessary.

3.3 Single Qubit Gates

Classical computers operate with logical gates like AND, OR, and NOT, which preform the manipulation of the information according to a truth table. For example, the NOT gate changes the state of a bit from $0 \to 1$ and vice versa. Analogous to the classical logic gates, quantum logic gate, or just quantum gates can be defined. Due to the fact that quantum logical operation have to be reversible, they can be described by an unitary operator $\hat{U}$ acting on the quantum state vector $|\psi\rangle$ of a qubit. In the following, the most important quantum gates are introduced.

One of the simplest quantum gates is the NOT gate, which, analogous to the classical NOT, switches the state $|0\rangle$ to $|1\rangle$ and vice versa. However, it act of course also on a superposition of states, in the manner that $|0\rangle$ and $|1\rangle$ change their role:

$$\alpha\,|0\rangle + \beta\,|1\rangle \xrightarrow{\text{NOT}} \alpha\,|1\rangle + \beta\,|0\rangle\,. \tag{3.6}$$

This operation can be represented by the unitary matrix

$$\hat{U}_{\text{NOT}} = \begin{pmatrix} 0 & 1 \\ 1 & 0 \end{pmatrix}, \tag{3.7}$$

which denoted as X in many textbooks due to historical reasons.[(b)] One immediately sees, that $U^2_{\text{NOT}} = \mathbb{I}_2$,[(c)] thus applying a NOT gate twice results in the original state.

The maybe most famous single qubit quantum gate is the *Hadamard* gate, whose matrix representation is

$$H = \frac{1}{\sqrt{2}} \begin{pmatrix} 1 & 1 \\ 1 & -1 \end{pmatrix}. \tag{3.8}$$

If applied to the ground state $|0\rangle$, the resulting state is a coherent superposition

$$H\,|0\rangle = \frac{1}{\sqrt{2}}\,|0\rangle + \frac{1}{\sqrt{2}}\,|1\rangle\,. \tag{3.9}$$

[(b)] This matrix is the same as the Pauli matrix σ_x.

[(c)] $\mathbb{I}_2$ denotes the two-dimensional identity matrix $\begin{pmatrix} 1 & 0 \\ 0 & 1 \end{pmatrix}$.

This operation is very often the initial operation in quantum algorithms. In the quantum interference experiments, performed on the exciton qubit system described in the chapters 6 and 8, the first laser pulse acts also like a Hadamard gate, enabling the qubit's quantum interference property.

The Hadamard gate is sometimes regarded as something like the square root of the NOT gate, because it rotates half the pathway of a NOT gate, but applying the Hadamard gate twice is the identity operation $\mathrm{H}^2 = \mathbb{I}_2$. However, the difference is only a constant phase factor $-\pi/2$, and in many experiments the absolute phase cannot be controlled, thus it is generously neglected.

The last single qubit gate which is regarded here is the *arbitrary phase shifter gate*. It acts only on the phase of the qubit, rotating it by an angle of ϕ. Its unitary matrix is given by

$$P(\phi) = \begin{pmatrix} 1 & 0 \\ 0 & e^{i\pi\phi} \end{pmatrix}. \tag{3.10}$$

It has been proven mathematically, that any unitary operation on a single qubit can be approximated as a series of operation by the Hadamard gate together with the $\pi/8$ phase shifter gate. However, an arbitrary phase shifter gate is is very useful to simplify some quantum algorithms (i. e. reduce the number of gate operations) and for fault-tolerant quantum computation.[13] A strong motivation for the experiments presented in chapter 8 was to create such a gate for the exciton qubit system, where the phase angle can be controlled by an electric signal.

3.4 Two Qubit Gates

In order to build a quantum circuit, it is necessary to couple two (or more) qubits. For this purpose one has to build two-qubit gates. The prototype and most important two-qubit gate is the *controlled-NOT* (CNOT) gate. It has two qubit inputs; the first qubit is called *control qubit* and the second one *target qubit*. The CNOT performs the following: If the control qubit is 0, the target bit keeps its current state. If the control qubit is 1, then the target bit is flipped according to the NOT gate operation. Like every quantum gate, the CNOT gate can be represented by an unitary matrix. Because it acts on a two-qubit state, it is described by a 4×4 matrix:

$$\hat{U}_{\mathrm{CNOT}} = \begin{pmatrix} 1 & 0 & 0 & 0 \\ 0 & 1 & 0 & 0 \\ 0 & 0 & 0 & 1 \\ 0 & 0 & 1 & 0 \end{pmatrix}. \tag{3.11}$$

The CNOT gate forms, together with the Hadamard gate and the phase shifter gate, an universal set of quantum gates. With such an universal set it is possible to perform in principle every thinkable quantum algorithms.[73–76]

An important application of the CNOT gate is the creation of entanglement between two

qubits. Using the quantum circuit shown in figure 3.1b, the state of the two qubits is transformed into a Bell state.

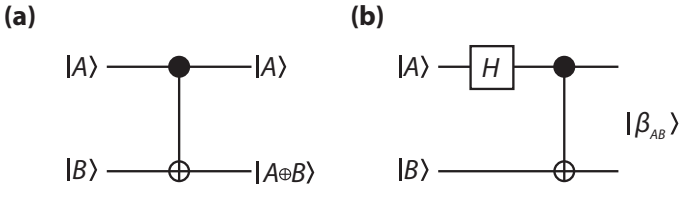

Figure 3.1: (a) Graphical representation of the CNOT gate. (b) Quantum circuit to create an entanglement between two qubits. (c) "Truth table" of the circuit in (b)

Another important two-qubit gate, is the SWAP gate. It simply exchanges the quantum state of two qubits. This operation might be very useful for a physical implementation of a quantum computer, if, for example the qubits are lined up in a row and can only be measured at one position or only one position in an in-/outport for photon qubits. The matrix representation of the SWAP gate is given by:

$$\hat{U}_{\text{SWAP}} = \begin{pmatrix} 1 & 0 & 0 & 0 \\ 0 & 0 & 1 & 0 \\ 0 & 1 & 0 & 0 \\ 0 & 0 & 0 & 1 \end{pmatrix} \tag{3.12}$$

There are of course more (to be exact: an infinite number) two (and more) qubit gates, and especially the controlled-phase shifter gate and the three qubit Toffoli gate are often used to describe quantum algorithms. However, the CNOT gate is universal and quite simple, so the research for physical implementations of two-qubit gates focuses mainly on this gate.

3.5 Quantum Algorithms and Applications

3.5.1 Quantum Algorithms

A quantum algorithm is an algorithm, where each step is performed on a quantum computer. Each algorithm starts with the initialization of the qubits in a qubit register. The steps of the quantum algorithm are composed of quantum gates acting on one or more qubits. After the quantum operations are performed, the final states of the qubits are measured, yielding the result of the algorithm. Many quantum algorithms are only probabilistic algorithms, in the sense that they give the correct answer only with a high probability.

In the following the Deutsch-Josza algorithm is briefly explained, and it is commented on the basic strategies of the important Grover and Shor algorithms.

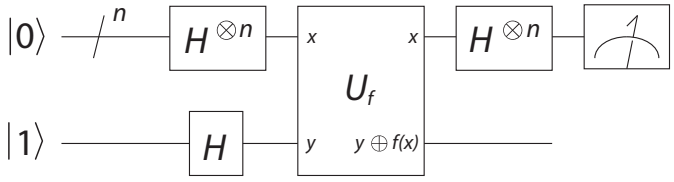

Figure 3.2: Quantum circuit implementation of the general Deutsch-Jozsa algorithm. The upper wire represents a set of n qubits.

Deutsch-Josza Algorithm

One of the first and simplest invented quantum algorithms is the Deutsch-Jozsa algorithm. The original deterministic version quantum algorithm was developed by D. Deutsch and R. Jozsa,[69] and further improved by R. Cleve et al.[77] to the general Deutsch-Jozsa algorithm, which is presented here. It is an example of a deterministic quantum algorithm, producing always the correct answer. It solves the problem, whether the *oracle* function

$$f : \{0,1\}^n \to \{0,1\} \tag{3.13}$$

is either constant (returning the same result for all inputs) or balanced (returning 1 for half of the inputs and 0 for the other half). The best classical algorithm has to evaluate the function f for n inputs $2^{n-1}+1$ times.

The steps of the algorithm are shown in figure 3.2. The algorithm requires $n+1$ qubits, from which n are initialized in the $|0\rangle$ state (query register) and the last qubit in the $|1\rangle$ state (answer qubit). The first step of the algorithm is to apply a Hadamard gate to all qubits, bringing the system in the superposition state

$$|\Psi\rangle = \frac{1}{\sqrt{2^{n+1}}} \sum_{x\in\{0,1\}^n} |x\rangle \left(|0\rangle - |1\rangle\right). \tag{3.14}$$

Thus, a superposition of all values is stored in the query register, and the answer qubit is in the superposition state ($|0\rangle$-$|1\rangle$). Afterwards, the function f, implemented as a quantum oracle is evaluated using $U_f : |x, y\rangle \to |x, y \oplus f(x)\rangle$, giving

$$|\Psi\rangle = \frac{1}{\sqrt{2^{n+1}}} \sum_{x=0}^{2^n-1} (-1)^{f(x)} |x\rangle \left(|0\rangle - |1\rangle\right). \tag{3.15}$$

A second Hadamard gate on all qubits in the query register transforms the qubits to their final state:

$$|\Psi\rangle = \frac{1}{\sqrt{2^{n+1}}} \sum_z \sum_x (-1)^{xz+f(x)} |z\rangle \left(|0\rangle - |1\rangle\right). \tag{3.16}$$

The following measurement of the qubits in the query register will yield 0s if the function constant. For a balanced function, at least one qubit will yield 1.

In summary, a quantum computer can solve this problem with only one evaluation of the function f, due to the parallel evaluation by the superposition state. However, this quantum algorithm solves only a theoretical problem, but it gives the idea that the quantum parallelism can be used to solve mathematical problems more efficiently than a classical computer.

Grover Algorithm

The Grover algorithm is a quantum algorithm for searching an unsorted database with N entries. L. Grover showed, that it needs only $\mathcal{O}(\sqrt{N})$ steps on a quantum computer, whereas on a classical computer $\mathcal{O}(N)$ steps are necessary.[78] The algorithm utilizes an oracle function O, which can be written as

$$|x\rangle \xrightarrow{O} (-1)^{f(x)} |x\rangle , \tag{3.17}$$

where $f(x) = 1$, if x is the solution of the search problem, else $f(x) = 0$. So, the oracle function marks the solution of the search problem by a phase shift. The algorithm cannot provide the location of the solution, but through its iterative procedure the amplitude of the solution is increased while all other database states are decreased. Thus, the Grover algorithm is a probabilistic algorithm.

Shor Algorithm

The most famous quantum algorithm is Shor's factoring algorithm. The interest in this algorithm arises from the fact, that the security of public-key encryption is based on the mathematical problem of factoring large numbers. The runtime of best classical algorithm (the general number field sieve algorithm[79]) is approximately $\mathcal{O}(\exp((\log N)^{1/3}(\log\log N)^{2/3}))$. By using a quantum computer, this can be dramatically reduced to $\mathcal{O}(\log N^2)$.

The algorithm has a classical and a quantum part. The classical part converts the problem of factoring N into the problem of finding the multiplicative order of an arbitrary element of $\mathbb{Z}_N^\times$, which is a cyclic group related to N. The quantum part of the algorithm is based on the quantum version of the discrete Fourier transform, to find the order of $\mathbb{Z}_N^\times$. The quantum Fourier transform performs the same transformation as the (classical) fast Fourier transform, but it uses the quantum parallelism for speedup.

The Shor algorithm represents a crucial breakthrough, because it offers an exponential speed-up over both deterministic and probabilistic classical algorithms for an important mathematical problem.

3.5.2 Quantum Key Distribution and Quantum Repeater

Quantum Key Distribution (QKD) is a method of securely distributing a cryptographic key by using a quantum communication channel. Subsequently, this key can used to encrypt and

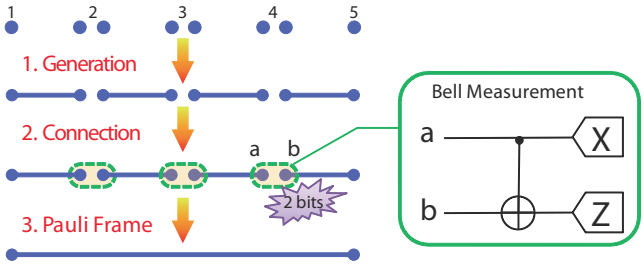

Figure 3.3: Sketch of an idealized quantum repeater (taken from [84]).

decrypt messages using one-time-pad cryptography over a classical communication channel.

The easiest method for QKD is the BB84 protocol.[80] It is based on polarization coding of qubits, using four quantum states from two conjugate Hilbert space bases. For example, a classical bit can be encoded in the basis of horizontal ('0') and vertical ('1') polarization of single photons. A second, conjugate basis can be provided by the diagonal polarization, +45° ('0') and +45° ('1'). The sender (often called Alice), sends now a sequence of photons to the receiver (Bob), with each photon encoded in a randomly chosen basis. Bob measures the polarization state of the single photons, and because he doesn't have any information about the basis which was selected by Alice, he choses also a random basis. After the transmittance Alice and Bob compare the chosen bases, and whenever they have chosen the same basis, they can use the transmitted bit for a cryptography key. To check for the presence of eavesdropping, Alice and Bob afterwards compare a part of their keys. If someone has intercepted and replaced photons from on the communication between Alice and Bob, the two keys differ, because the eavesdropper cannot estimate the correct basis to send his photon.

Other QKD protocols have been invented, for example using entangled-photon pairs or a third conjugate basis. A fundamental problem of all QKD protocols is, that—in contrast to classical computation—a quantum channel cannot be amplified. This prevents today the application of QKD over long distances, because of absorption of photons in the transmission channel and loss of coherence and entanglement. To overcome this issue, a new device—a quantum repeater is proposed.[81–83]

Figure 3.3 shows a schematic sketch of a quantum communication channel equipped with a series of ideal quantum repeaters. Each repeater consist of two stationary qubits. In a first step, Bell pairs are generated and exchanged between neighboring repeaters. By measurement in the Bell basis one remote Bell pair between the stations 1 and 5 is created.[84] This enables a secure communication over much longer distances. However, building a quantum repeater is quite difficult. It requires not only coherent control over a few stationary qubits, but also the interconversion of photon qubits ("flying qubits") to and from the stationary qubits.

4 Experimental Setup and Techniques

In this chapter the general experimental setup of the different experimental methods are explained. It introduces the basic techniques and the sample structures.

4.1 Low Temperature Microscope

Basically all experiments described in this thesis require a high spatial resolution and a temperature of only a few kelvin. The central unit of the experimental setup is therefore a sample holder with a low temperature microscope, which can be dipped into a liquid helium dewar (temperature T = 4.2 K). At the lower end of the sample holder the low temperature microscope (figure 4.1) is mounted. It consists of a microscope objective and a piezo driven xyz-positioner. The sample is mounted on this positioner and can thereby be accurately positioned (with a step size of less than 250 nm at low temperatures) below the microscope objective. Although the objective is interchangeable, for the most experiments an infinity corrected objective from Zeiss[(a)] is used.

Electrical connections from the sample holder head to the low temperature microscope provide control of the nanopositioner and allow for electrical control and measurements of

[(a)] Zeiss Epiplan, 100x, NA=0.75 , working distance 0.95 mm.

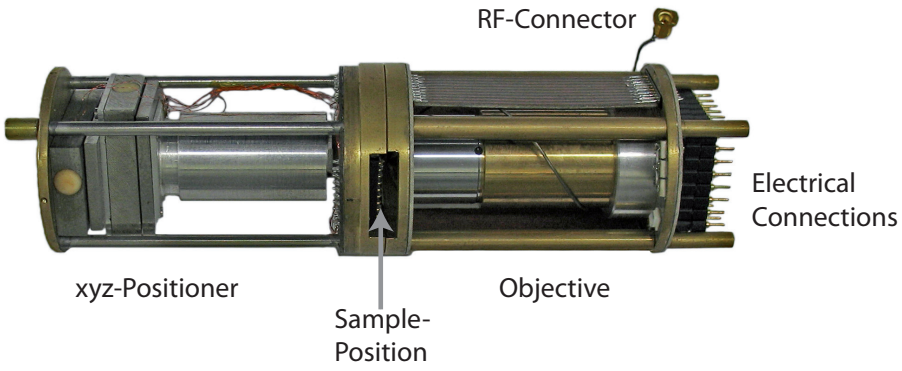

Figure 4.1: Low temperature microscope with the high NA objective in the upper part and the xyz-positioner in the lower part.

the sample. For the high resolution PC measurements shielded cables are available and a semi-rigid cable allows the connection of a radio frequency signal to the sample.

Before cooling the sample holder in the liquid helium, the lower part is enclosed in a stainless steel tube, which is evacuated and filled with helium gas at a low pressure (approximately 1 mbar) to ensure heat transfer.

The upper part of the sample holder (figure 4.2) consist of a breadboard for flexible mounting of different optical components. An imaging unit allows to monitor an image of the sample on a TV screen. This makes it easy to position the structure under the microscope objective. The laser excitation is steered in a free space setup to the head of the sample holder. A beamsplitter splits the excitation into two beams; one is directed down to the sample, while the other is used to record the intensity with a photodiode or powermeter. The beamsplitter lets also pass a part of the luminescence from the sample to a multimode fiber coupler. From there the light is guided via a multimode optical fiber to the spectrometer. For some experiments, the fiber coupler is exchanged by a mirror to achieve a free space setup in the detection path. By exchanging the beamsplitter the setup can be optimized for different experiments. For example, a non-polarizing beamsplitter cube is used for polarization sensitive experiments, while for PL measurements an uncoated pellical beamsplitter is optimal suited (reflection of the laser excitation 8 %, transmission of the luminescence 92 %).

4.2 Photoluminescence Spectroscopy

As explained in chapter 2.2, the photoluminescence spectroscopy is usually the method of choice for a first investigation of a QD sample. It is based on the principle of excitation of charge carriers by light and the subsequent relaxation of them into the lowest states of the QDs. The light resulting from the recombination of electron and hole is analyzed with a spectrometer.

4.2.1 Excitation

For a basic characterization of QD samples the charge carriers are usually excited in the host material of the QDs. Therefore, the excitation energy has to be higher than the band gap of this material. For InGaAs QD embedded in GaAs usually a red Helium-Neon laser (633 nm, 1.96 eV) is used. The CdSe QDs, investigated in chapter 5, are embedded in ZnSe, which has a band gap of about 2.8 eV at 4 K. Therefore a semiconductor laser diode[(b)] with a wavelength of 404nm, equivalent to 3.07 eV, is used as excitation source. The intensity of the excitation is adjusted to the appropriate level by different neutral density filters and a computer controlled, continuously variable metallic filter wheel.

[(b)] Coherent VioFlame™

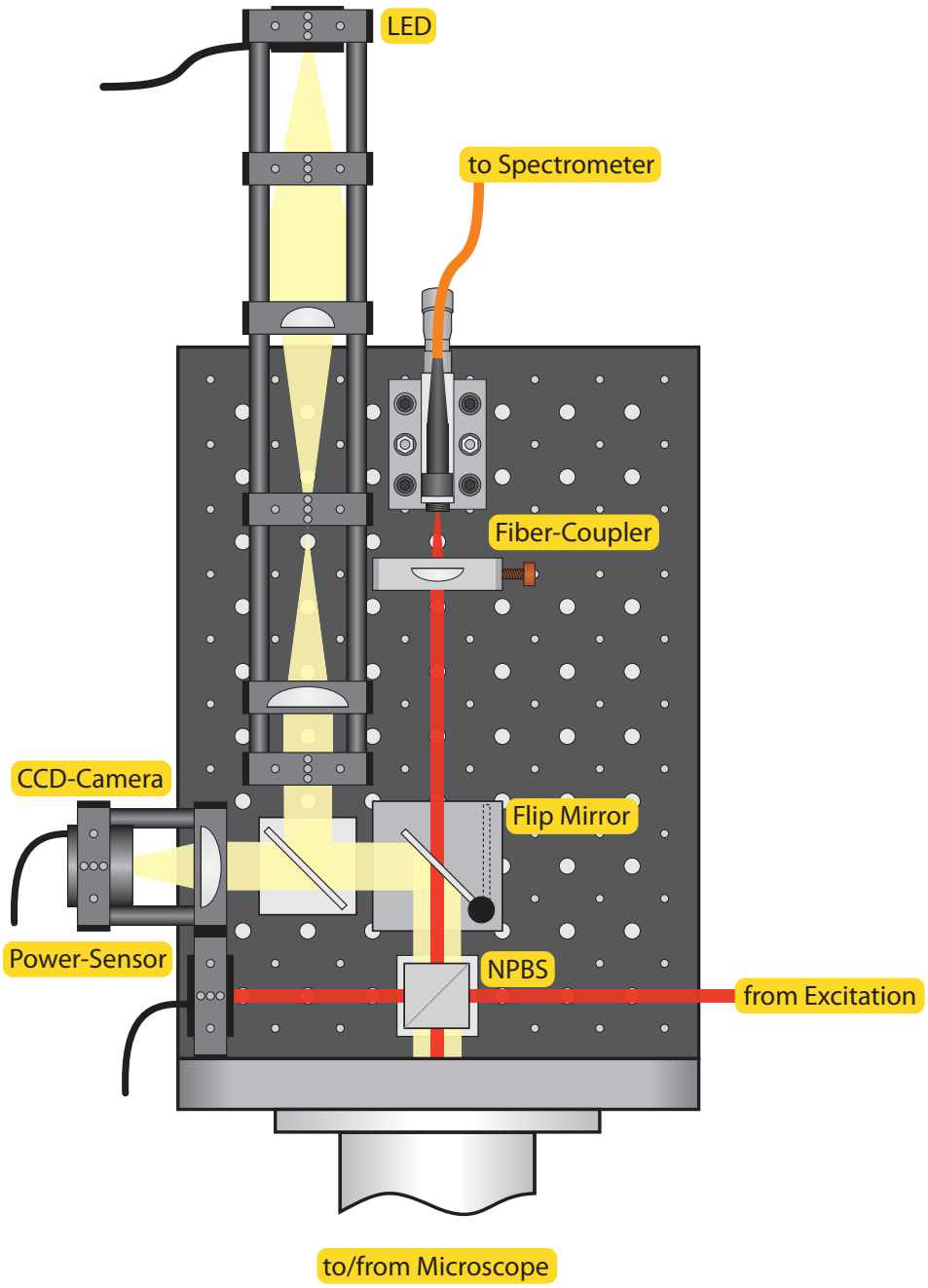

Figure 4.2: Head of the sample holder with the usually mounted optical components. The electrical connections to the sample and piezo positioner are attached on the rear panel.

4.2.2 Detection

The collected luminescence of the sample is dispersed by a spectrometer and detected by a multichannel camera. For all experiments presented within this thesis, Acton spectrometers with a focal length f_L of 500 mm[(c)] and at least two different diffraction gratings (g = 300 $^1/_{\text{mm}}$ and g = 1200 $^1/_{\text{mm}}$, both blazed at 750 nm) are used. A liquid nitrogen cooled silicon charge coupled device (CCD)[(d)] is mounted on each spectrometer. The more sensitive CCD can detect light with wavelength from 200 nm up to 1075 nm. The quantum efficiency in the most interesting wavelength range for InGaAs QD spectroscopy from 920 to 960 nm is approximately 65 %. In the range of the CdSe QD (about 550 nm) the quantum efficiency is slightly higher, approximately 70 %. The maximum spectral resolution of the setup is determined by the spectrometer geometry, slit width of the spectrometer entrance, the dispersion of the used grating in the spectrometer, the pixel size of the CCD-Camera and the central wavelength. In case of the fiber based setup, the entrance slit is formed by the core diameter of the optical fiber. For high resolution measurements a multimode fiber with a core diameter of 50 µm is used, which fits very well to the resolution of the spectrometer in this case. The maximum achievable resolution is then 80 µeV at 950 nm (InGaAs QDs) and 280 µeV at 550 nm (CdSe QDs).

In the PL signal from a few QDs, the line width of the dots is usually much smaller than the resolution of the spectrometer, and the separation of the lines from single QD is much higher than the resolution. Therefore, the resolution of the setup is sometimes not the crucial parameter, and it is better to use a fiber with a bigger core diameter which makes it easier to couple the luminescence into the fiber. A good compromise, and extensively used here in most experiments here, is a multimode fiber with a core diameter of 105 µm.[(e)]

4.3 Photocurrent Spectroscopy

The photocurrent (PC) technique has three major benefits. First, it allows for very high resolution measurements, only limited by the accuracy of the applied bias voltage of the diode and the line width of the resonant laser excitation. Second, and this is here the most important point, it is possible to investigate the coherent properties of the QD ground state driven by a resonant laser field, which is very difficult with other techniques. Third, it allows for a quantitative quantum measurement.

[(c)] Acton 500i or Acton 2505i
[(d)] Princeton Instruments SPEC-10 400R/LN or SPEC-10 400BR/LN
[(e)] Thorlabs Multimode VIS-IR Fiber AFS105/125Y, NA=0.22, Core 105 µm

4.3.1 Excitation and Pulse Preparation

Laser system

For the resonant excitation of the QD states, two titanium sapphire laser (Ti:Sa)[(f)] systems are available. They are pumped by diode-pumped Nd:YVO_4-ring-lasers,[(g)] which provide a very stable and high quality pump beam at 532 nm with a maximum power of 6.5 W and 10.5 W, respectively.

The laser systems feature a broad tuning range from less than 700 nm up to more than 980 nm. They can be (quasi-)continuously tuned by a Lyot-filter, but by doing so small mode jumps and the intensity variation appear. The systems are designed as ultrafast oscillators, providing 1.5–4 ps[(h)] laser pulses with a repetition rate of 80 MHz. The pulse length cannot be tuned directly, but it can be influenced via different parameters in the adjustment. To analyze the pulse length, a part of the laser beam is directed into an autocorrelator.[(i)] There is a strong evidence, that the pulse is transform limited and has a hyperbolic secant envelope. This is based on the one hand on the autocorrelation signal and on the other hand on the spectrum of the laser pulse. By assuming this pulse form, the width of the autocorrelation signal can be converted into the temporal pulse width. It is also possible to operate the laser systems as tunable cw laser sources with a narrow line width for high resolution measurements.

The maximum power of the Ti:Sa lasers is approximately 1 W and 3 W, but for pulsed operation at 920 nm the maximum power is lower, about 300 mW and 1 W, respectively. This is more than enough for the excitation of the QDs in the coherent experiments. The laser beam is therefore attenuated by a set of neutral density filters and a continuously variable metallic filter wheel.

The laser beam has a horizontal polarization, but for many experiments in this thesis the polarization has to be adjusted in order to suppress quantum beating due to the excitation of both fine structure splitted exciton lines.[85] Therefore, a $\lambda/2$-wave plate is inserted into the beam path to rotate the polarization accordingly.

Michelson Interferometer

In most of the coherent experiments a double pulses excitation is essential. The delay time t_{delay} and the optical phase relation between the two pulses has to be tuned very precisely to achieve reliable results. This is realized by a Michelson interferometer, whose one interferometer mirror has a fixed position, while the other is mounted on a high-precision linear positioner. This positioner consists of a motorized linear stage with a travel range of 300 mm for the coarse delay and a thereon attached closed-loop nanopositioner with a travel range of 500 µm for the fine delay. The coarse delay has a precession of 0.1 µm while the fine delay

(f) Coherent Mira Optima 900-D
(g) Coherent Verdi V6 or V10
(h) The systems can also be configured as femtosecond lasers, then providing 80–250 fs laser pulses.
(i) APE 'Mini', 'PulseCheck' or 'Carpe'

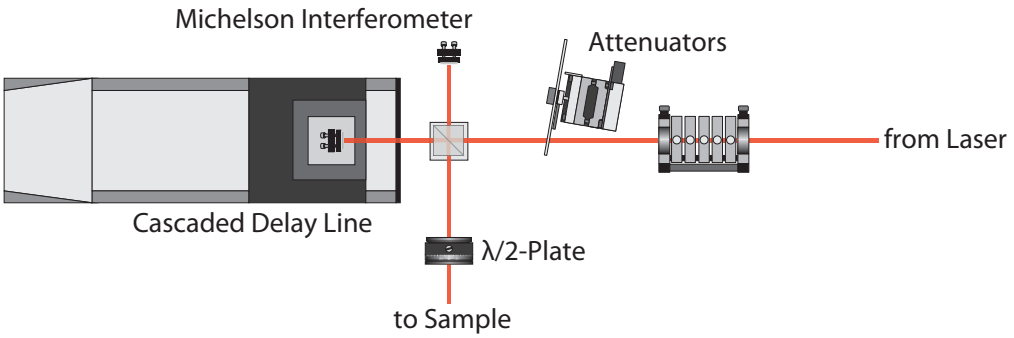

Figure 4.3: The laser beam is attenuated to the appropriate level and passes then the Michelson interferometer two create the double pulses. A $\lambda/2$-plate is used to change the orientation of the linear polarized light from the laser. This is necessary to suppress the quantum beats, which else could appear due to the FSS of the exciton line.

achieves a nominal repeatability of 5 nm. The time delay between the two pulses is adjusted by driving the coarse delay a certain distance from the zero point (the point, at which both light paths have the same (optical) length). The precision of the delay time depends critically on the determination of this zero point. To find this position, the following simple procedure is executed: The two laser pulses show only (optical) interference if they are overlapping each other. Hence, the coarse delay is slowly varied while the intensity at the interferometer output is recorded. Thereby the zero point can be found quickly with an accuracy of less than 50 µm, corresponding to an uncertainty of the delay time of 0.3 ps. With more effort the precession of the determination of zero point could certainly be improved, but this is usually not necessary.

In nearly all double-pulse experiments, the optical phase relation between the two laser pulses is an important parameter. With the present setup, it is not possible to control the phase in an absolute manner, but for a given delay time the phase can be continuously changed by the nanopositioner.

4.3.2 Current Measurement

The PC signal is very low in the coherent experiments presented in this thesis. It will be shown later, that the maximum expected PC from a coherent manipulation, e. g. by a so called π-pulse, produces a current signal of only 12.81 pA for a laser repetition frequency of 80 MHz. In practice, the PC is even lower, because not all charge carriers tunnel out from the QD. Additionally, a current up to 50 pA from incoherent absorption is superimposed with the relevant signal.

To measure these low currents with high accuracy a transimpedance amplifier with a very large amplification of 1 GV/A or 10 GV/A is used. Most experiments have been performed

with a home build amplifier, based on the ultralow input bias current operational amplifier AD549 from Analog Devices.[86] The electric circuit is displayed in figure 4.4. The choice of the feedback resistor is mainly influenced by the resulting bandwidth and noise level. Here, a feedback resistor R_f with a resistance of 1 GΩ is used, resulting in a current to voltage conversion of 1 mV/pA. An additional capacitor parallel to R_f suppresses oscillation or gain peaking of the amplifier. The dominating noise of the amplifier is the Johnson noise of the feedback resistor. The noise is transferred to the output without amplification, but rolled off by the bandwidth limit of the circuits transresitance. This leads to a root mean square output noise (RMS) of[87]

$$E_{\mathrm{noR}} = \sqrt{2k_B T R_f \pi \mathrm{BW}_t}, \tag{4.1}$$

where k_B is the Boltzman's constant and T the temperature of the resistor in Kelvin. Because the signal increases linear with the feedback resistor, the signal-to-noise ratio of the setup improves by $\sqrt{R_f}$ for an increasing feedback resistance. A measurement of the noise level from the amplifier reveals a RMS noise of 22 fA.

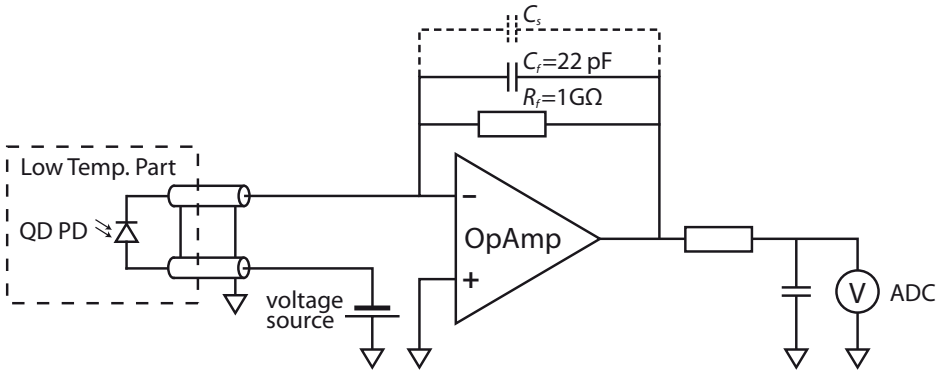

Figure 4.4: Schematic circuit diagram of the photocurrent setup with the transimpedance amplifier in the center. The photodiode symbol on the left adumbrates the sample.

The bandwidth of the transimpedance amplifier is determined by the feedback resistor R_f, the phase compensation capacitance C_f, and the stray capacitance C_S, parallel to C_f:

$$\mathrm{BW}_t = \frac{1}{2\pi R_f (C_S + C_f)}, \tag{4.2}$$

The amplifier circuit has a bandwidth of approximately 15 Hz. Additionally the output of the amplifier is equipped with a low-pass filter matched with the analog to digital converter.

The circuit has a very high impedance and high sensitivity, thus it requires a good shielding and an effective power supply bypassing. To reduce the external noise, it is battery powered and enclosed in a metal housing with good grounding and the only external electrical connections

are those to the sample. These connections are all over coaxial cables and as short as possible. The data transfer to the computer is provided by fiber-optic communication.

As an alternative to the home build system, a commercial high gain current amplifier from FEMTO is available[(j)]. It includes a sophisticated electrical circuit, which achieves a gain of 10 mV/pA at a bandwidth of 200 Hz. The noise of this system is roughly the same as for the home build one, but the higher bandwidth allows for faster measurements if the subsequent electronics is adapted accordingly. However, this improvement has not been carried out yet.

The voltage signal from the amplifier is measured by an integrating analog to digital converter (ADC)[(k)] with a resolution of 15.625 µV/bit and a full scale of ±512 mV. Thus, the resolution is slightly higher than the noise level of the amplifier.

4.4 Photon Correlation Measurement

The proof of a single photon emission is done by performing photon correlation measurements based on a Hanbury-Brown and Twiss (HB-T) setup (figure 4.5). The luminescence of the single photon emitter must be spectrally filtered to avoid cross-correlations with other sources (e. g. the excitation or other emitters), or other states of the same quantum emitter. For this purpose, the HB-T setup is mounted behind the spectrometer. Thereby a very good filtering is achieved, but the weak light throughput is disadvantage. The light coming from the spectrometer is collimated and splitted by a 50 : 50 non-polarizing beam splitter cube. Both parts are coupled into multimode optical fibers and guided to two similar single photon counting modules (SPCM)[(l)]. For each registered photon the SPCM sends an electrical pulse to a time to digital converter[(m)], which has a time resolution of 40 ps. This resolution is about a factor 10 higher than the time resolution of the SPCM. By recording the time difference between a registered photon at the first SPCM and a photon at the second SPCM, it is possible to create a histogram which is closely related to the second order correlation function. A simplified explanation that such a setup can distinguish between a true single photon emitter and a conventional light source can be given as follows. A single photon can not be split into two parts and therefore can only be transmitted *or* reflected. Thus, it will be detected only by *one* SPCM. If now the light truly is a sequence of single photons, the two detectors will never register a photon at the same time and the histogram will show a dip at zero time difference.

4.5 Coherent Electric Control Experiments

The experiments presented later in chapter 8, featuring the coherent electric control of the exciton phase, require an electric signal, synchronous to the optical excitation. In this work

[(j)] Model LCA-200-10G
[(k)] Maxim MAX132[88]
[(l)] SPCM-AQRH-16-FC, a Si APD Single Photon Counting Module with <25 dark counts/s and FC receptacle
[(m)] PicoQuant Timeharp 200

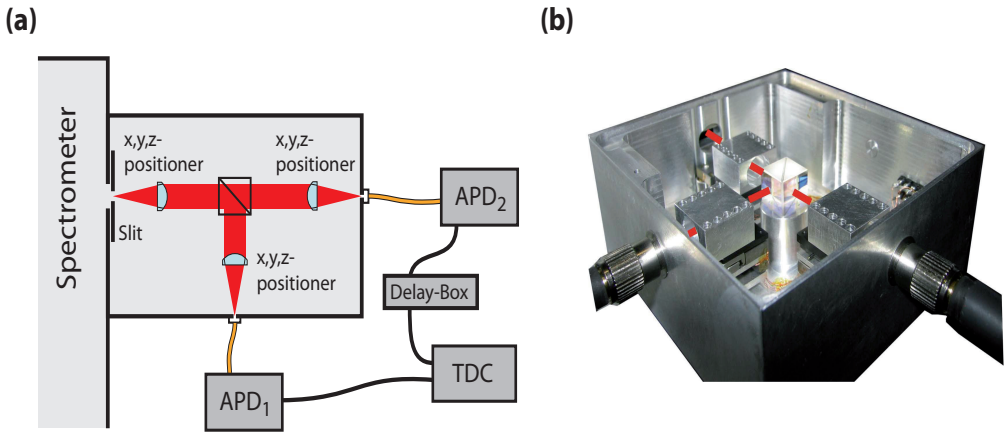

Figure 4.5: (a) Schematic illustration of the Hanbury-Brown and Twiss setup for the photon correlation measurements. (b) Picture of the real setup.

two types of signals have been used. In the first approach, a very short electric pulse was created and applied to the QD photodiode. This signal underlies a significant dispersion, broadening a 400 ps electric pulse to more than a nanosecond, due to the too large capacity of the QD photodiode. As an alternative signal, which provides basically the same effect on the quantum system, a 2.4 GHz radio frequency (RF) signal is created from the laser reference. A block diagram for both circuits is shown in figure 4.6a-c.

Short electric pulse generation

To create a synchronous electric pulse the signal of a fast photodiode is utilized (figure 4.6a). This photodiode is by default integrated in the Ti:Sapphire laser and usually used to monitor the modelocking of the laser. In a first step, the provided signal is converted to a sine wave with the frequency of the laser repetition. This is achieved by amplifying the signal from the photoreceiver by 40 dB, running the amplifier into saturation. The resulting square wave is transformed to a sine wave by a low-pass filter.

The principle of the short pulse creation, depicted in figure 4.6d, is quite simple. However, the implementation requires a very good layout of the printed circuit board and well selected electric components, due to the high frequencies. The sine wave is fed into a first fast comparator, resulting in a square wave. The voltage level of the square wave depends only on the comparator output voltage. From this square wave only the rising edge is relevant here. By changing the control voltage, applied to the second input of the comparator, the point in time of the rising edge of the square wave can be shifted in respect to photodiode signal. The maximum time shift depends on the voltage amplitude of the sine, and is here in the order of

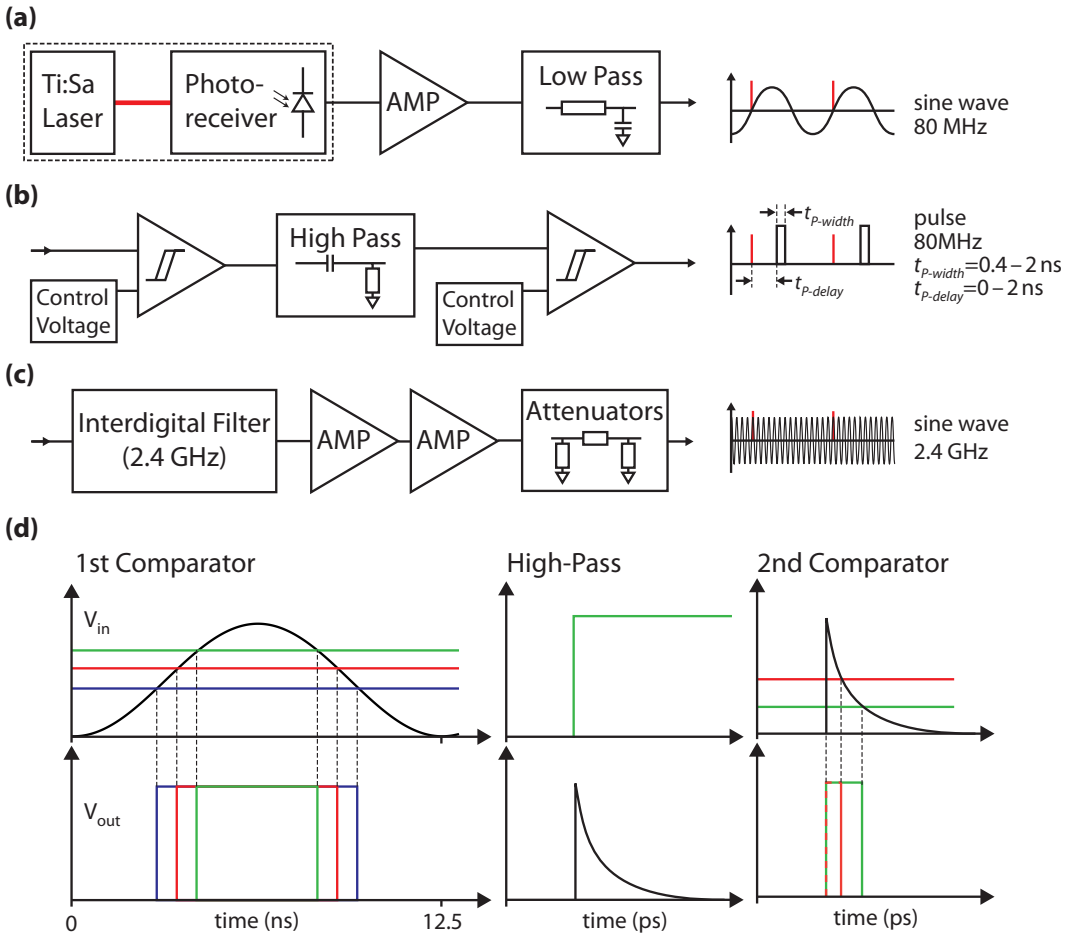

Figure 4.6: Creation of the fast electric signal as a block diagram: (a) Deriving the sync signal from the laser. (b) Creation of the short electric pulse. (c) By filtering the 2.4 GHz signal is created from the pulse. (d) Schematic drawing of the short pulse generation.

a few nanoseconds. Afterwards, the square wave output is filtered by a high pass filter, leading to a sharp peak. By means of the second comparator, this peak is transformed into the short voltage pulse. By adjusting the control voltage of the second comparator, the length of the voltage peak can be adjusted. This setup achieves a minimum pulse length of 400 ± 20 ps. The jitter of the rising edge of the short pulse as well as the jitter of the pulse length are in the order of 10 to 20 ps. This is close to the resolution of the 6 GHz real-time oscilloscope, which was used to develop and control the setup. For further improvements of the circuit layout, a 20 GHz sampling oscilloscope has been recently purchased.

Radio Frequency Signal Generation

To avoid the dispersion of the short electric pulse a 2.4 GHz signal was used as an alternative. Of course, this signal underlies the same dispersion, but as it consists only of a single frequency, only the amplitude and phase is affected. The signal is derived as the 30th harmonic of the laser repetition frequency (80 MHz), enabling a synchronous sequence of the optical pulses and the electric signal.

The signal is created directly from the short electric pulse by utilizing with an interdigital filter,[(n)] with a very strong suppression of other frequencies. Afterwards, the signal is amplified by two cascaded 30 dB amplifiers from Mini-Circuits.[(o)] The peak to peak voltage amplitude of the 2.4 GHz exceeds 2 V at the amplifier output, and can be reduced by a series of attenuators to the appropriate level for the experiment.

By adjusting the control voltage of the first comparator, the signal can be shifted continuously in time for more than one period, referred as phase shift of the electric signal in chapter 8.

4.6 Samples

4.6.1 InGaAs Quantum Dot Photodiode

All presented coherent measurements in this thesis refer to a particular InGaAs QD, located in a sample grown in 1999. This QD was also inversitgated in the scope of the PhD theses of S. Stufler, P. Ester and M. C. Hübner.[35,89,90] The sample was developed at the Walter Schottky Institute (WSI) in Garching, and was optimized for PC spectroscopy. It was designed in such a way, that no charge carriers permanently resist in the QD in the PC bias voltage regime. A detailed description of the individual processing steps and sample parameters can be found in the PhD thesis of F. Findeis (sample 120799.2).[18]

The structure of the n-i-photodiode is shown in figure 4.7(a). After the growth of a n^+-doped GaAs, containing an AlAs/GaAs super-lattice, a n-doped GaAs layer with a doping concentration of 5×10^{18} cm^{-3} was deposited. Subsequently to this back contact, a 40 nm thick

[(n)] ID-Elektronik GmbH, Customized 13 cm Interdigitalfilter
[(o)] 10–2500 MHz Amplifier ZKL-2R5

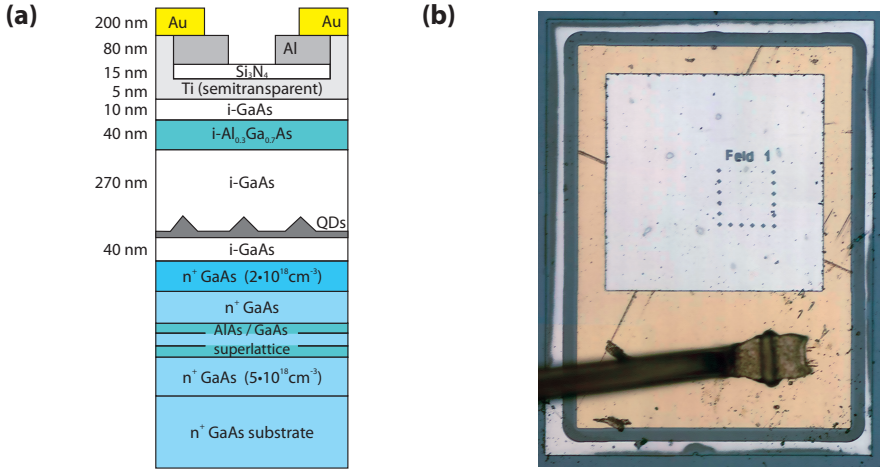

Figure 4.7: (a) Layer structure of the sample (b) Microscope image of a photodiode on the sample

layer of intrinsic GaAs was grown. On top of this layer, the InGaAs QDs were grown. The areal density of the QDs is low enough to achieve optical access to a single QD by means of the later processed shadow mask. Afterwards, 270 nm intrinsic GaAs, 40 nm of $Al_{0.3}Ga_{0.7}As$ and a 10 nm capping layer were deposited. On top of the semitransparent Schottky gate (5 nm Ti) a near field shadow mask was processed. For this step, a 20 nm thin Si_3N_4 layer was deposited, serving as an etch stop. The shadow mask material is a 80 nm aluminum layer, in which apertures with a diameter of 100 nm to 500 nm were etched by using e-beam lithography and reactive ion etching techniques. In contrast to the selective optically excitation of individual QDs, the electrical access to the QDs is not selective. All QDs in the photo diode (about 12 million QDs in this structure) are electrically contacted in parallel. Figure 4.7(b) shows a microscope image of the sample. The photodiode has an area of $300 \times 400\,\mu m^2$. On the gold metalization on the left the bond wire is visible. The shadow mask is located in the right area, between the bigger markers.

The intrinsic region of this structure is 360 nm broad and the build-in voltage $V_{build\text{-}in}$ of the GaAs-Schottky contact is approximately 0.75 V. Hence, the electric field can be calculated (following equation 2.2) by

$$F \approx 27.78 \cdot 10^3 V_{bias} \frac{1}{\mathrm{cm}} + 20.8 \frac{\mathrm{kV}}{\mathrm{cm}}, \tag{4.3}$$

where V_{bias} denotes the applied bias voltage.

During this work samples from the group of D. Reuter (Universität Bochum) with the same semiconductor layer structure were also investigated. However, in these samples no

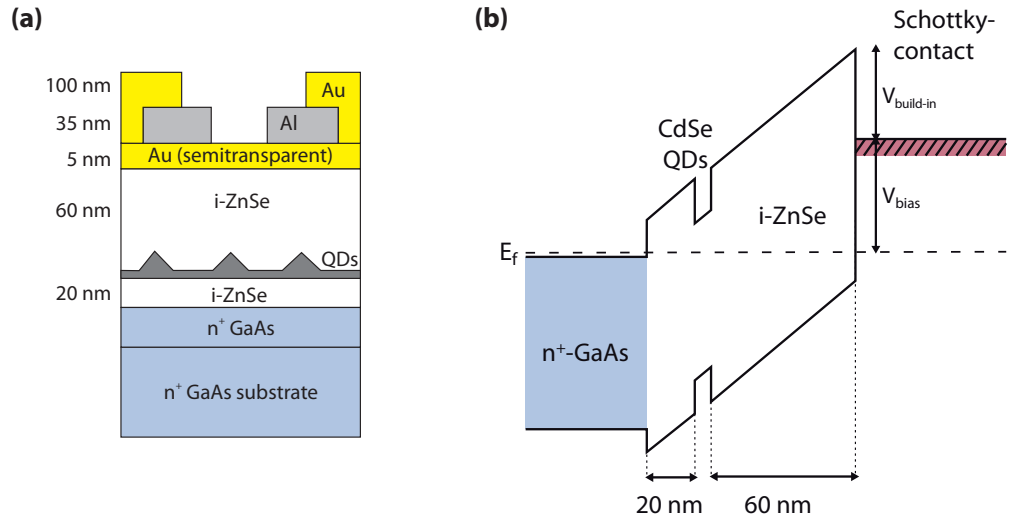

Figure 4.8: (a) Layer structure of the sample used for the voltage dependent PL. (b) Simplified band diagram of this CdSe QD PD. The diagram is not to scale and the band bending at the heterojunction is neglected.

appropriate QD (concerning spectral position and spacial and spectral isolation) has been discovered, yet. In the future, the samples from Bochum will surely play an important role.

4.6.2 CdSe Quantum Dot Photodiode

The CdSe/ZnSe QD photodiode structures are grown in the group of K. Lischka. These structures are a completely new development, therefore a couple of different samples were grown to find an optimal structure. However, the basic layer sequence is the same for all samples. Figure 4.8a shows a schematic cross section of the multilayer structure. The samples were grown using standard MBE on a *n*-doped (2×10^{18} cm^{-3}) (0 0 1) GaAs substrate.The substrate is overgrown with a doped GaAs layer of about 200 nm to achieve a good surface quality. At first a layer of intrinsic ZnSe was deposited, in most of the samples.[(p)] The thickness of this layer varied in the different samples from 20 nm to 40 nm. In the newest samples optimized for the PC spectroscopy an additional n-doped ZnSe layer was grown at first. These samples are explained in detail in the thesis of M. Panfilova.[91]

For the QDs, a thin layer of CdSe was grown on top of the intrinsic ZnSe. The 3D Stranski–Krastanov CdSe dot formation was induced by a thermal activation process and in-situ controlled by reflection high energy electron diffraction (RHEED) measurements.[92] For an optimal areal density of QD, the thickness of the CdSe layer was about 2.1 monolayers, but

[(p)] The latest samples are grown with a *n*-doped ZnSe layer at first, to reduce the band bending at the heterojunction.

within the different samples the nominal thickness of the layer ranged from 2 to 3 monolayers. The areal density was not a very critical parameter in these first studies, because even for a higher QD density spectrally separated lines arise at the low energy tail of the ensemble. In none of the samples a QD density comparable to the low density InGaAs QD samples was found. Finally, the QDs were capped with a layer of intrinsic ZnSe with a thickness of 50 to 60 nm The Schottky barriers of the samples were established by a 5 nm thick semi-transparent gold layer on top of the structures. For spatial isolation of single QDs an aluminum shadow mask was fabricated using e-beam lithography. The Ohmic back contacts were processed with indium on the GaAs substrate.

To calculate the electric field in this structure, again equation 2.2 is used. However, one has to be very carefully in this case, as the band diagram (figure 4.8b) exhibit a heterojunction between the GaAs and the ZnSe. Regarding the QCSE in the experimental data, there is a strong evidence, that for an excitation above the ZnSe band gap the electric field is reduced at the position of the QDs. This effect might be a result of the heterojunction, but there is no proof of this these.

5 Voltage Dependent Photoluminescence of CdSe Quantum Dots

In principle, CdSe quantum dots may provide advantages over InGaAs for quantum information processing purposes. Due to the larger band gap of this II-VI material system,[(a)] the confinement energy of electron and hole is significantly larger than in the III-V semiconductor material systems. Moreover, the Coulomb correlation energies are also about ten times higher, thus it should be possible to manipulate these quantum dots with femtosecond laser pulses without affecting the biexciton state of the QD.

In this chapter, the PL properties of single CdSe QD in a photodiode are investigated. The research has been performed in a close collaboration with Marina Panfilova and Alexander Pawlis form the group of Klaus Lischka. Further measurements, featuring a first evidence of a resonant photocurrent signal, will be presented in the PhD thesis of M. Panfilova.[91]

5.1 Ensemble Photoluminescence

The PL observed in the unstructured region of the sample is inhomogeneously broadened to about 70 meV, as shown in figure 5.1a. The broadening exhibits a slight asymmetry; towards the low-energy tail of the PL spectrum the QD density decreases and separated lines appear. By using the shadow mask apertures the excited region of the sample is further restricted to a small area and clearly separated lines are observed. These arise probably from just a few QDs. However, due to the higher Coulomb correlation energies in the II-VI semiconductors, the lines from different states of a single QD cover a larger energy range as compared to the III-V system. This increases the probability that the spectra from different dots are overlapping; making an identification of the different lines from a single dot much more difficult.

5.2 Spectral Jitter

For some QDs a spectral jitter over time is observed (see figure 5.1b), which is a well-know effect in CdSe QDs. Localized charge carriers in the nanoenvironment of the QD are held responsible for this behavior. However, the jitter did not appear always and not on every dot. Especially the PL of later grown samples does not show this jitter, proving the enhancement of the structural properties due to optimized growth conditions and improved sample processing.

[(a)] The band gap of ZnSe at 4 K is about 2.8 eV

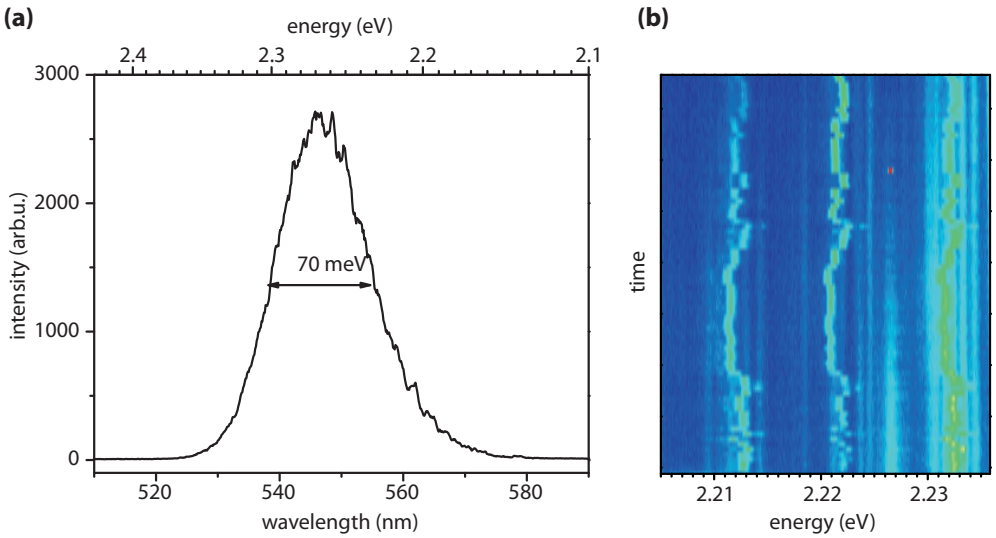

Figure 5.1: (a) PL of the QD ensemble in the unstructured region of the sample. (b) Spectral jitter of the transition lines. The spectrum is recorded through a shadow mask. The timescale of the jitter is in the order of one second, which is the integration time of the CCD in this experiment.

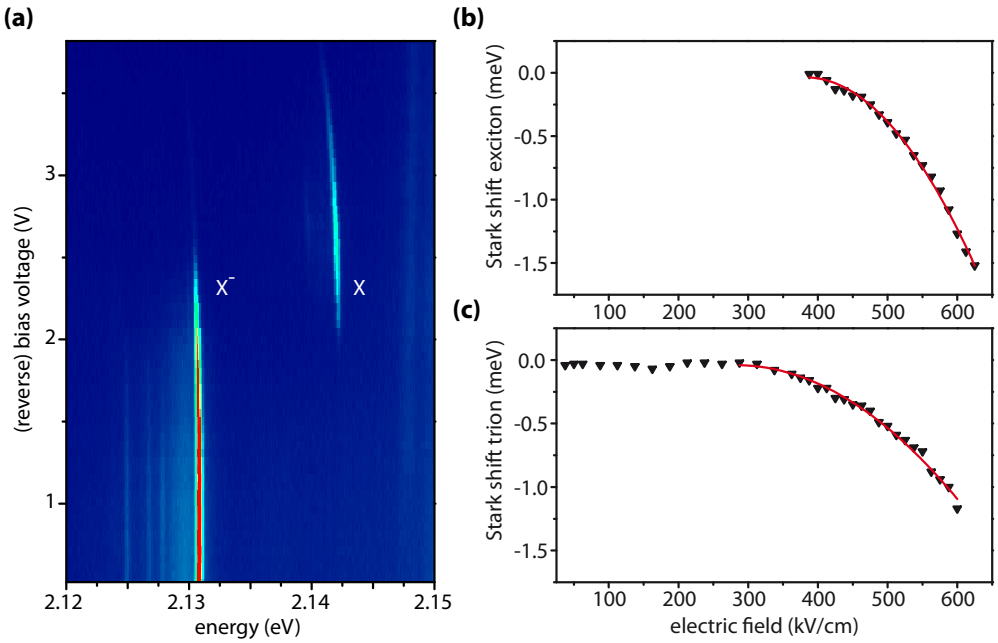

Figure 5.2: (a) PLV. (b) and (c): Energy shift of exciton and negative charged exciton due to the QCSE.

The effect is used to identify lines originating from the same QD analog to Patton et al.,[93] by assigning those transitions which show the same jitter to the different exciton states of an individual dot. However, the measurements presented in the following sections are recorded from spectral lines which do not show this jitter, as it prevents a detailed analysis.

5.3 Single QD Photoluminescence

5.3.1 Voltage Dependent PL

Figure 5.2a shows a two-dimensional map of the luminescence, in which two spectral lines as a function of the bias voltage are visible. The lines seem to arise from a single QD and are separated by 11 meV (at a bias voltage of 2.2 V). To identify the exciton state, from which these line originate, results from other groups and the band diagram of the photodiode (see chapter 4.6.2) are taken into account.

A strong luminescence line is observed at zero bias voltage. In this case band calculations indicate that the energy of the lowest conduction band state of the QD is below the Fermi level of the back contact. Therefore, electrons from the substrate can tunnel into the QD and occupy the single electron state. Hence, the dominate line in the PL at moderate excitation intensities originates from the recombination of the negative charged exciton, labeled with X^- in the diagram.

With increasing reverse bias voltage the conduction band ground state is lifted above the Fermi level, which favors the radiative recombination of the neutral exciton, which arises for reverse bias voltages larger than 2 V. However, there is a non-zero probability that two electrons occupy the QD even in this bias voltage region. Therefore, the spectral line of exciton transition is accompanied by the charged exciton line. The two lines are separated by the electron–exciton binding energy which is determined to be 11 meV, in agreement with the results in reference [94]. At high bias voltages the intensities of both, X and X^-, are consequently reduced, since the tunneling process is here competing with the radiative decay of the excitons. For voltages higher than 3.8 V the PL is effectively quenched due to the tunneling. This principally confirms the possibility of photocurrent measurements with single dots on our samples, however the IV characteristic of this sample shows a too large background current at this bias voltage.

The observed line widths of both excitonic transitions are in the range of 280 µeV, limited by the spectral resolution of our setup. However, a slight increase of the line width is observed at reverse voltages above 2 V. This broadening may arise from the reduced exciton lifetime due to the additional tunneling, but also from interaction with charge carriers from the increasing background current.

5.3.2 Stark Effect

A central feature observed in the PLV spectrum, shown in figure 5.2a, is the quantum-confined Stark effect (QCSE). The vertical electric field F at the QD, which is responsible for the QCSE, can be calculated according to equation 2.2. In this sample, the distance between the Schottky contact and the doped back contact is 80 nm. For the build-in voltage of the ZnSe-Schottky diode, a value of 1.4 V is assumed.

The Stark effect is evaluated for both exciton lines. The upper diagram in figure 5.2b shows the Stark shift of the exciton transition and the lower one the shift of charged exciton transition as a function of the electric field strength. In the region between approximately 300 and 600 kV/cm one can observe a quadratic dependence for both transitions as expected for the common QCSE. Optimal agreement with the measured data is obtained by fitting the data by the function given in equation 2.4 in this electric field range. For the exciton the polarizability α is found to be 10 ± 1 μeV/(kV/cm)^2 and for the charged exciton $\alpha = 25 \pm 2$ μeV/(kV/cm)^2 is derived from the fit. For low electric field strength the exciton transition vanishes due to the formation of the charged exciton. For the charged exciton state, a significant deviation from the common Stark effect is observed below a field strength of 300 kV/cm. In this region the transition energy is nearly independent of the applied bias voltage. This behavior is can be explained in two different ways: Either an anomalous Stark effect appears, similar to the theoretical prediction for a lateral field by S. Ritter et al.,[53] or the electric field is screened in this voltage region. Recent measurements support the latter assumption, because the behavior of spectral lines seems to depend strongly on the energy of the excitation, and thereby on the number of additional charge carriers, which may screen the electric field.

5.4 Photon Correlation Measurements

In order to confirm that the spectral lines originate from single quantum emitters, correlation measurements were performed on several spectral lines. A typical normalized correlation spectrum is shown in figure 5.3. Due to the exponential state decay, the data can be fitted with the expression

$$g^{(2)}(t) = (1 - g^{(2)}(t0)) \times \exp\left(\frac{-|t - t_0|}{t_c}\right), \tag{5.1}$$

where $g^{(2)}(t0)$ corresponds to the minimum correlation value and t_c is the convolution of the decay time with the response time of the single photon counters. The time-axis is afterwards corrected, so that $t_0 = 0$ ns.

From the correlation data in figure 5.3 $g^{(2)}(t_0) = 0.4$ is obtained, which is a clear evidence that the line arises from a single quantum emitter. However, stray light from the laser excitation and other sources create a substantial background in the correlation measurement, which limits the achievable $g^{(2)}(t_0)$. The parameter t_c, which gives an upper limit for the radiative lifetime of the state is determined to be 900 ± 100 ps, which is a typical value for the largest CdSe Stranski–Krastanov dots.[95]

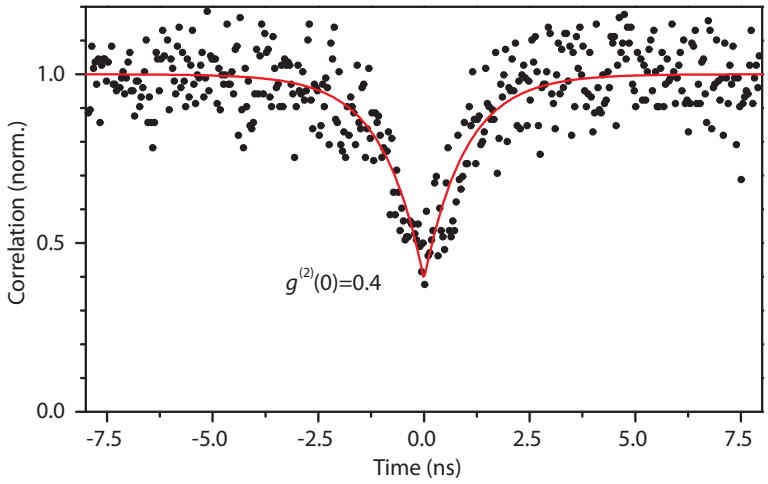

Figure 5.3: Photon correlation measurement after interband excitation at zero bias voltage. The correlation data is fitted with the expression for an exponential state decay.

5.5 Towards Photocurrent Measurements

The investigations of CdSe/ZnSe photodiodes show the expected fundamental effects: charging of the exciton state, observation of the QCSE and a reduction of the luminescence due to tunneling. Thus, this basic research opens a new material system for coherent spectroscopy in the PC regime.

At the beginning of theses experiments with the CdSe/ZnSe QD photodiodes, the reverse current of the Schottky diodes was to high for their application in PC spectroscopy. With great efforts the processing of the Schottky diodes was optimized, so that now good Schottky diodes can be fabricated. However, resonant PC spectroscopy is not easy in this spectral region, especially because tunable cw laser source with a narrow bandwidth are rare in this spectral region. Usually, cw experiments are utilized to align the photocurrent measurement setup and are necessary to evaluate the Stark shift in the PC regime before the coherent properties can be investigated with picosecond laser excitation. Nevertheless, first evidence of a resonant PC signal has been observed[96] and further experiments are planned.

6 The QD Exciton Two-Level System

The concept of two-level systems (TLS) is a simple, but important model system of quantum mechanics. The approach is widely utilized to describe the behavior of many different systems. In several situations the interaction between light and matter (e. g. atomic systems, excitons in semicondutors,…) can be reduced to the concept of the TLS. The theory for a two-level atom interacting with a light field is conceptual the same as for a spin 1/2 system in a magnetic field, developed by I. I. Rabi[97] and F. Bloch[98] in the first half of the 20th century. The basic theory is treated in many textbooks, e.g. in references [99–102]. In the first part of this chapter (6.1 and 6.2), the basic theory of TLS is presented. The derivation of the basic equations follows closely the approaches in [31] and [100]. In the derivation, the interaction between light and matter is treated in a semiclassical theory, i.e., the quantum mechanical properties of the TLS are considered, whereas the light field is treated as a classical field.

The second part of the chapter (6.3) extends the basic equations to the model of an exciton in a QD photodiode. Therefore, the damping mechanisms, which occur for an exciton in a QD photodiode are modeled within the density matrix equations. Although these extensions are only phenomenological, their physical background is discussed. Additionally, the theoretical quantities of the density matrix are mapped to the experimental quantity – the photocurrent.

6.1 Basic Theory of Two-Level Systems

In this work the TLS is represented by the ground state of the QD ("empty" QD), denoted as $|0\rangle$ and the single exciton ground state, denoted as $|X\rangle$ or more general as $|1\rangle$. Apart from the phenomenological damping due to radiative recombination, all interactions with the surrounding and other eigenstates of the QD are neglected within this first part. The Hamiltonian of the undisturbed system is

$$\hat{H}_0 = |0\rangle\, \hbar\omega_0\, \langle 0| + |1\rangle\, \hbar\omega_1\, \langle 1| \tag{6.1}$$

with $\hbar\omega_0$ and $\hbar\omega_1$ being the eigenenergies of the ground state and the excited state, respectively. Their energy separation is $\hbar\omega_{10} = \hbar\omega_1 - \hbar\omega_0$. A schematic sketch of the TLS is illustrated in figure 6.1a.

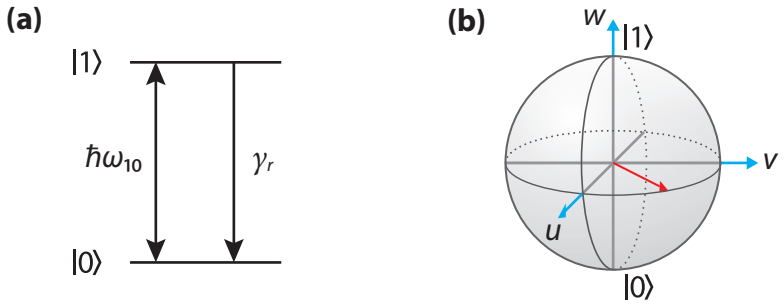

Figure 6.1: (a) two-level system with the states $|0\rangle$ and $|1\rangle$. The transition is driven by a light field at resonance. The system can underlies a spontaneous decay with the decay rate γ_r. (b) Representation of the quantum state on the Bloch sphere.

6.1.1 Representation of a Two-Level System

The quantum state of a two-level system can be described by its density matrix

$$\hat{\rho} = \begin{pmatrix} \rho_{00} & \rho_{01} \\ \rho_{10} & \rho_{11} \end{pmatrix}. \tag{6.2}$$

The diagonal elements ρ_{00} and ρ_{11} of the density matrix represent the occupancy of the lower and upper level of the TLS, respectively. The non-diagonal elements ρ_{10} and ρ_{01} are called coherences of the system. For them the relation

$$\rho_{01}(t) = \langle 0|\,\hat{\rho}(t)\,|1\rangle = \rho_{10}^{*}(t) \tag{6.3}$$

is obtained.

The quantum mechanical state of the TLS can be visualized on the Bloch sphere, shown in figure 6.1b. In an undamped system, the identities $\rho_{00} + \rho_{11} = 1$ and $\rho_{10} = \rho_{01}^{*}$ are valid, and therefore the system can be displayed on the surface of an unit sphere by using the following definition of the Bloch vector $\boldsymbol{R} = (u, v, w)$:[(a)]

$$u = \tilde{\rho}_{10} + \tilde{\rho}_{01} \quad = 2\Re(\tilde{\rho}_{10}) \tag{6.4}$$

$$v = i(\tilde{\rho}_{10} - \tilde{\rho}_{01}) = 2\Im(\tilde{\rho}_{10}) \tag{6.5}$$

$$w = \rho_{11} - \rho_{00} \tag{6.6}$$

Thereby the components u, v, w of the Bloch vector are given in a Cartesian coordinate system. The w component is called *inversion* and reflects to the occupancy of the upper level of the

[(a)] Later on, the rotating frame will be used and ρ_{10} will be transformed into $\tilde{\rho}_{01}$, which is already used in these equations.

system. The representation of the system's state as the bloch vector is also possible when the system is damped. Then the vector lies inside the sphere.

6.1.2 Interaction with the Light Field

When interacting with a light field, the Hamiltonian of the system is composed of the Hamiltonian of the undisturbed system $\hat{H}_0$ and the Hamiltonian $\hat{H}_L$, which describes the interaction between the TLS and the light field:

$$\hat{H} = \hat{H}_0 + \hat{H}_L. \tag{6.7}$$

The size of a QD is very small compared to the wavelength of the light field u sed for the excitation. Hence the variation of the field within a QD can be neglected, and one can take the field at the point $\boldsymbol{R}_0$ which determines the position of the QD as a whole. This is usually known as the *dipole approximation*.[103]

To model arbitrary laser pulses and pulse sequences with a center frequency ω_L, the light field $\boldsymbol{E}(t)$ is described by

$$\boldsymbol{E}(t) = \boldsymbol{\varepsilon} E_0(t) e^{-i\phi(t)} e^{-i\omega_L t} + c.c. \tag{6.8}$$

where $\boldsymbol{\varepsilon}$ is an unit polarization vector, and $\phi(t)$ the phase. The light field is described by its slowly varying envelope $E_0(t)$ which determines the temporal pulse shape. This especially limits this approach to not to short and well shaped laser pulses. For a typical ps laser pulse from a Ti:Sapphire laser, which is used here, an envelope with a Gaussian or hyperbolic secant shape can be assumed. If a sequence of laser pulses with different center wavelengths should be applied, $\boldsymbol{E}(t)$ simply has to be replaced by a sum of the different electric fields. For the here discussed cases, ϕ is only necessary if the system is interacting with two laser pulses with different phase, else it can be set to 0 without loss of generality.

The strength of the interaction between the light field a the TLS depends on the optical transition dipole matrix element $\boldsymbol{\mu}_{01}$. The transition between the lower and the upper state is then described by the polarization operator

$$\hat{\boldsymbol{P}} = \boldsymbol{\mu}_{01} |0\rangle \langle 1| + H.C. \tag{6.9}$$

The interaction Hamiltonian for optical excitation close to the resonance is given by

$$\hat{H}_L = -\boldsymbol{E}(t) \cdot \hat{\boldsymbol{P}}(t). \tag{6.10}$$

6.1.3 Solving the Liouville-von Neumann Equation

The dynamics of the system can be described by the Liouville-von Neumann equation of motion of the density matrix. It is given by

$$i\hbar\frac{d}{dt}\hat{\rho} = \left[\hat{H}, \hat{\rho}\right]. \tag{6.11}$$

When inserting the light field in the equations of the density matrix elements, terms with $E_0(t)\mu_{01}$ appear. It is convenient to define a parameter Ω, which is called *Rabi frequency*, by

$$\Omega(t) = \frac{E_0(t)\mu_{01}}{\hbar}. \tag{6.12}$$

This parameter determines the frequency, with which the system oscillates between the states $|0\rangle$ and $|1\rangle$ under resonant excitation. This oscillation is called *Rabi oscillation* and is a fundamental effect of a two-level system. To simplify the calculation, the *rotating-wave approximation* (RWA) is commonly used. Thereby, the contributions from the rapidly varying terms with $\exp(\pm 2i\omega t)$ (whereas $\omega \approx \omega_L \approx \omega_{10}$) are neglected (Riemann-Lebesgue Lemma[31,104]). This is generally a good approximation if not to short pulse are used and the excitation is close to the resonance, i.e. $\omega_L + \omega_{01} \approx 2\omega_L$ is valid. At the same time the detuning $\delta = \omega_L - \omega_{01}$ is introduced.

Usually the behavior of the system is easier to understand if the equations are transferred into a *rotating frame*, which rotates with the laser frequency ω_L.

$$\tilde{\rho}_{01}(t) = e^{-i\omega_L t}\rho_{01}(t) \tag{6.13}$$

Due to this transformation, the rotation of the Bloch vector of the system around the w-axis is reduced to the frequency of the detuning.

Finally, after some algebra, a set of ordinary differential equations is obtained, which describes the dynamics of the TLS for resonant and slightly detuned excitation:

$$\frac{d}{dt}\tilde{\rho}_{01} = i\frac{\Omega_0(t)}{2}e^{i\phi}(\rho_{11} - \rho_{00}) - i\delta\tilde{\rho}_{01} \tag{6.14}$$

$$\frac{d}{dt}\rho_{00} = i\frac{\Omega_0(t)}{2}(\tilde{\rho}_{10}e^{i\phi} - \tilde{\rho}_{01}e^{-i\phi}) \tag{6.15}$$

$$\frac{d}{dt}\rho_{11} = i\frac{\Omega_0(t)}{2}(\tilde{\rho}_{01}e^{-i\phi} - \tilde{\rho}_{10}e^{i\phi}) \tag{6.16}$$

This set of equations is called optical Bloch equations in the rotating wave approximation in a rotating frame.

6.1.4 Phenomenological Dephasing due to Recombination

The equations 6.14–6.16 are only valid for a system without relaxation. But, as indicated in figure 6.1a, the TLS can exhibit a damping, for example due to radiative decay from $|1\rangle$ to $|0\rangle$ at a rate γ_r. For such a system, a phenomenological dephasing term can be included by adding

$$-\frac{\rho_{01}}{T_2} \tag{6.17}$$

to the right side of equation 6.14 and the relaxation terms

$$\frac{\rho_{11}}{T_1} \quad \text{and} \quad -\frac{\rho_{11}}{T_1} \tag{6.18}$$

to the right side of the equations 6.15 and 6.16, respectively. The time constants T_1 and T_2 were first introduced in the Bloch equations of nuclear magnetic resonance and electron spin resonance. Thus, the terminology is taken from this field, where T_1 is called longitudinal lifetime, and T_2 transversal lifetime. For the atomic TLS presented here, T_1 is related to the population decay and T_2 to the loss of coherence. At this point, T_1 is the time constant of the radiative decay, and $\gamma_r = 1/T_1$.

The decay constants are not independent, because a decay of the population leads also to a loss of coherence. This relation is described by the equation

$$\frac{1}{T_2} = \frac{1}{2T_1} + \frac{1}{T_2^*}. \tag{6.19}$$

The constant $T_2^* = 1/\gamma_2^*$ corresponds to a dephasing of the coherence without loss of population and is called *pure-dephasing*. For the undisturbed QD system at a temperature of 4.2 K, no evidence of pure-dephasing has been found, but for the later presented coherent electric control, this constant is used to model the thereby induced additional dephasing.

6.2 Rabi Oscillations and Quantum Interference

Rabi Oscillations

When the system is excited coherently with a laser at resonance ($\delta = 0$), the TLS oscillates between the upper and the lower level with the frequency $\Omega(t)$. For a light field at resonance the dynamics of Bloch vector $\boldsymbol{R}$ of the upper and lower level is then given by

$$u = 0 \tag{6.20}$$

$$v = \sin[\Omega(t)t] \tag{6.21}$$

$$w = -\cos[\Omega(t)t]. \tag{6.22}$$

When a constant light field is applied for a time τ, the Bloch vector rotates an angle $\Theta = \Omega\tau$ around the u axis. Extending this relation for arbitrary pulses leads to

$$\Theta = \int_{t_{Start}}^{t_{End}} \Omega(t)dt. \tag{6.23}$$

The rotation angle Θ is commonly called *optical pulse area*. A pulse which results in a rotation angle of π or $\pi/2$ is called π-pulse and $\pi/2$ pulse, respectively.

Usually, one cannot measure these Rabi oscillations in the time domain[(b)], i. e. changing the pulse length continuously, but it is easy to change the intensity of the pulse. Therefore, the Rabi oscillations are recorded in the power domain.

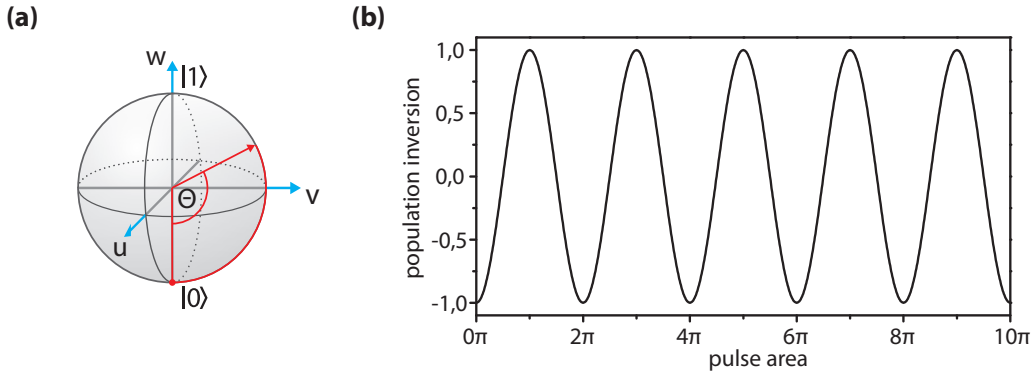

Figure 6.2: (a) Pulse area displayed on Bloch sphere. (b) Rabi-oscillation as a function of the pulse area.

Quantum Interference

To investigate the decoherence and quantum phase dynamics of the TLS, double pulse experiments are the favored method. A first laser pulse creates a coherent superposition of the upper and lower state. Thereby, the phase of the laser pulse is stored in TLS. After a delay time t_{delay}, the second laser pulse arrives and interferes with the quantum system. The resulting quantum state of the TLS depends now in the optical phase of a second laser pulse and of the phase of the quantum system at the time when the second laser pulse arrives. It is a good choice in such an experiment to use $\pi/2$-pulses, because then the interference contrast is the highest. In this case, constructive (destructive) interference will turn the system into the upper (lower) state, which is not the case for other pulse areas.

[(b)] There is a recent paper from A. Ramsay et al. who measured the beating exciton-dressed states in a time resolved fashion by a two-color experiment.[105]

The experiment can be very well explained by visualizing the trajectory of the state vector on the Bloch sphere, as shown in figure 6.3. The first $\pi/2$ pulse rotates the Bloch vector to the equator. During the delay time the quantum phase of the TLS might change, which will be extensively discussed later, but here the phase is assumed to be fixed. If the second laser pulse now has the same phase, the Bloch vector will be rotated to the upper state. Otherwise, if the phase of the second laser pulse has been shifted by π, the Bloch vector returns to the ground state.

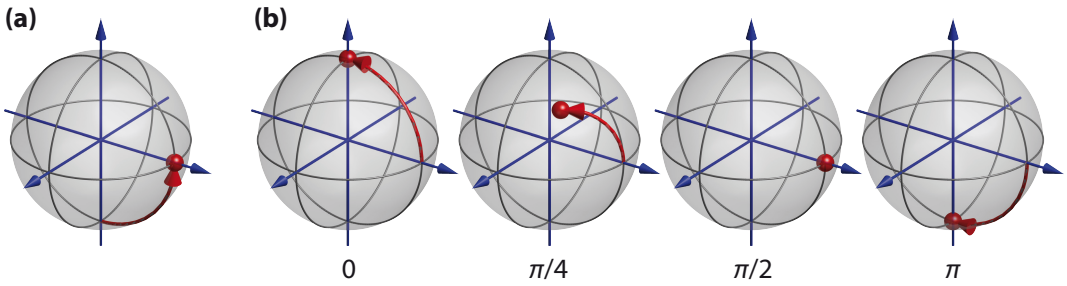

Figure 6.3: (a) Effect of the first $\pi/2$ laser pulse. (b) Result of the quantum interference due to a phase shifted second laser pulse. The phase shift between the two laser pulses is indicated below the Bloch spheres.

6.3 Exciton TLS with Electrical Access

The TLS, which is used in this work, is represented by the ground state of the QD ("empty" dot) and the single exciton ground state, as shown schematically in figure 6.4a. The general optical Bloch equations, derived in the previous section give in many situations an excellent qualitative description of the physics of this TLS under (near) resonant excitation. However, when the concrete system should be analyzed more precisely and quantitatively, the device structure around of the QD cannot be neglect. In particular in experiments where the dephasing plays an important role, deviations from the standard theory of a TLS become obvious and are nonsatisfying. Hence, the following section focuses on the physics of a quantum dot in a photodiode in more detail. Here, the decay of the exciton due to tunneling via the heavy-hole state and the excitation dependent damping of the Rabi oscillations are included into the theoretical model. To compare the theoretical results directly with the experiment, the values of the density matrix are mapped to the PC.

Please note, that the inclusion of the heavy-hole and electron state, as shown in figure 6.4 and explained in the next section, does not change the system to a (conventional) quantum mechanical three- or four-level system, because these state do not couple to the upper and lower state via the light field. Therefore, the exciton system is furthermore referred as a two-level system.

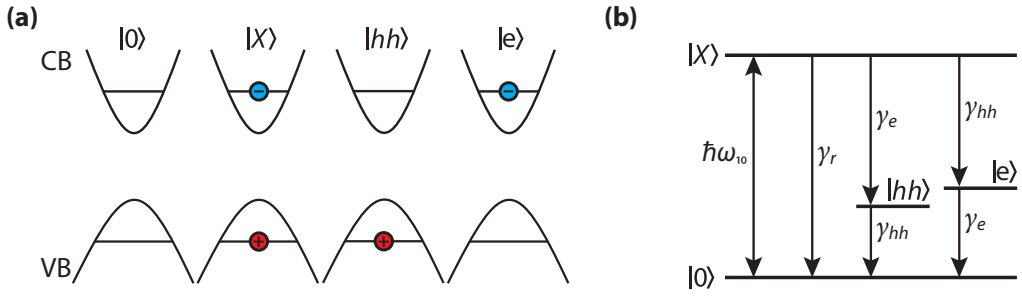

Figure 6.4: (a) The exciton TLS system in a QD; the ground state on the left is represented by the QD without an exciton, while the excited state $|1\rangle$ is represented by the single exciton ground state $|X\rangle$. During the relaxation process, the system can take the single heavy-hole state $|hh\rangle$ and the single electron state $|e\rangle$. (b) The excited state in a QD photodiode can decay either by radiative recombination or by tunneling of the exciton in a two-step relaxation process through the heavy-hole or electron state.

6.3.1 Tunneling Decay

When simulating double pulse experiments, in which the delay time between the two pulses is in the order of the electron tunneling time, the calculated data shows a significant deviation from the experiment. Especially in an inversion recovery experiment, presented in section 7.3.1, the experimental data cannot be fitted with the basic theory of a TLS. The reason for this is the tunneling process, which makes an extension of the general Bloch equations necessary.

The tunneling can be described as a *two-step relaxation process*, characterized by fast electron and slow heavy-hole tunneling. The following example emphasizes the problem: An exciton is created in the QD with a π pulse. After the time τ_e, the electron tunnels out of the dot, leaving the QD occupied with the heavy-hole ($|hh\rangle$). If now a second laser pulse arrives before the hole has tunneled out, the laser pulse would have to drive the $|hh\rangle \rightarrow |X^+\rangle$ transition, which is not resonant to the laser due to an energy renormalization of here about 0.5 meV. This is large enough, that a transform limited 2 ps laser pulse, which is used in this work, does not affect the state significantly.[(c)] Therefore, here only the two-step exciton decay via an intermediate state is included in the ordinary differential equations of the density matrix.

Although the electron tunneling is much faster than the heavy-hole tunneling, there is of course a non-zero probability that the hole tunnels first. In this case the QD is left in the single electron state $|e\rangle$, where the renormalization energy for the transition to $|X^-\rangle$ is 2.7 meV as compared to the neutral exciton transition. Because the occupancy of this state will always

[(c)] It should be noted, that if a shorter laser pulse would be used, there might be a contribution from this transition. In this case, the $|X^+\rangle$ state and its coupling with the light field have to be included in the equations.

decay very fast by the electron tunneling, the effect to the PC is much smaller than of the heavy-hole state. Nevertheless it can be easily included in the model in the same way as the $|hh\rangle$ state.

The variables ρ_{hh} and ρ_e represent the occupancy of the intermediate states. These states are filled by the decay from the upper state ρ_{11} with a rate $\gamma_e(V_{bias}) = 1/\tau_e(V_{bias})$ and $\gamma_{hh}(V_{bias}) = 1/\tau_{hh}(V_{bias})$ and decays to the ground state ρ_{00} with the rate $\gamma_{hh}(V_{bias})$ and $\gamma_e(V_{bias})$, respectively. Both rates depend strongly on the applied bias voltage, as indicated in section 2.3.2. In the following, $\gamma_e(V_{bias})$ and $\gamma_{hh}(V_{bias})$ are written as γ_e and γ_{hh}, to keep the equations simple.

The extended optical Bloch equations are then given by

$$\frac{d}{dt}\tilde{\rho}_{01} = i\frac{\Omega_0(t)}{2}e^{i\phi}\left(\rho_{11}e^{-i\phi} - \rho_{00}e^{i\phi}\right) - i\delta\tilde{\rho}_{01} - \left(\frac{\gamma_r + \gamma_e + \gamma_{hh}}{2} + \gamma_2^*\right)\tilde{\rho}_{01} \tag{6.24}$$

$$\frac{d}{dt}\rho_{00} = i\frac{\Omega_0(t)}{2}\left(\tilde{\rho}_{10}e^{i\phi} - \tilde{\rho}_{01}e^{-i\phi}\right) + \gamma_r\rho_{11} + \gamma_{hh}\rho_{hh} + \gamma_e\rho_e \tag{6.25}$$

$$\frac{d}{dt}\rho_{11} = i\frac{\Omega_0(t)}{2}\left(\tilde{\rho}_{01}e^{-i\phi} - \tilde{\rho}_{10}e^{i\phi}\right) - (\gamma_r + \gamma_e + \gamma_{hh})\rho_{11} \tag{6.26}$$

$$\frac{d}{dt}\rho_{hh} = \gamma_e\rho_{11} - \gamma_{hh}\rho_{hh} \tag{6.27}$$

$$\frac{d}{dt}\rho_e = \gamma_{hh}\rho_{11} - \gamma_e\rho_e \tag{6.28}$$

6.3.2 Calculating the Photocurrent

The occupancy of the upper level of the quantum dot can be determined by measuring the photocurrent (PC). This is a remarkable property, because it allows for a quantitative measurement of the quantum state. The photocurrent from the QD after a coherent state preparation is given by the key formula

$$I_{PC} = fe\rho_{11}, \tag{6.29}$$

where f is the laser repetition frequency and e the elementary charge. However, in this equation it is assumed, that all excitons tunnel out from the QD (i. e. no radiative recombinations), and the heavy-hole tunneling is considerably faster than the laser repetition time.

The meaning of the formula can be explained as follows: After the coherent state preparation, the QD is occupied with an exciton with the probability ρ_{11}. The exciton tunnels out from the QD and creates a net charge flow of one electron.[(d)] To calculate the current, one has to multiply with the repetition frequency of the experiment, which is given by the repetition frequency of the laser system. This equation also gives the maximum expected current from

[(d)] Although the exciton consist of two charge carriers—electron and hole—it is obvious that only a net charge flow of one elementary charge is created.

the QD, if the TLS is prepared in the upper state $\rho_{11} = 1$. For a laser repetition frequency of 80 MHz, which is used in the labs in Paderborn, this result in a maximum current of $I_{PC_{max}} = 12.82\,\text{pA}$.

Detection Efficiency

As described above, the radiative recombination is a competing process to the tunneling decay. If the tunneling time is in the order of the recombination time, a significant fraction of the excitions recombine and thus the photocurrent is reduced. To calculate the photocurrent without neglecting the radiative recombination, the voltage dependent detection efficiency η is introduced. It describes the probability that the exciton decays by tunneling, and therefore contributes to the photocurrent, instead of recombining radiatively.

$$\eta(V_{bias}) = \frac{\gamma_e + \gamma_{hh}}{\gamma_r + \gamma_e \gamma_{hh}} \tag{6.30}$$

Consequently, in equation 6.29, ρ_{11} has to be replaced by $\eta \times \rho_{11}$.

Photocurrent Created During the Coherent Manipulation

In the most interesting experiments—the double pulse experiments—a second issue emerges. Here a part of the excitons created by the first pulse relaxes during the delay time t_{delay} between the two pulses of usually 50–500 ps. To include these charges in the simulation one has to "count" the excitons, which relax through the heavy-hole state. This can be done by calculating the integral

$$I_{PC} = fe \int_{t_1}^{t_2} (\gamma_e + \gamma_{hh}) \rho_{11}(t) dt \tag{6.31}$$

or the equivalent differential

$$\frac{d}{dt} I_{PC} = fe(\gamma_e + \gamma_{hh}) \rho_{11}. \tag{6.32}$$

This latter expression can be simply included in the system of the ordinary differential equations 6.24–6.28 and solved parallel with them by the same algorithm. In principle, one would have to integrate from the beginning of the coherent manipulation until the QD has relaxed completely into the ground state. In order to save calculation time, the equations 6.31 and 6.29 (including η) can be combined to

$$I_{PC} = fe \left(\int_0^{t_{calc}} (\gamma_e + \gamma_{hh}) \rho_{11}(t) dt + \eta \rho_{11}(t_{calc}) \right), \tag{6.33}$$

where t_{calc} can denotes a time after the last pulse of the sequence. Usually the calculation is stopped at this point, because nothing else will happen as that the relaxation into the ground state.

Heavy-Hole Tunneling

Another issue is the slow tunneling of the heavy-hole, especially at low electric fields. In many experiments it is desirable to have a very long coherence time (equivalent to the electron tunneling time), but then also the tunneling time of the heavy-hole increases up to values comparable to the repetition time of the laser (T_{rep} = 12.5 ns). In this case, there is a considerable probability that the QD is occupied with the heavy-hole when the next laser pulse (or pulse train) arrives. As described above, in such a case the laser pulse does not affect the QD. This reduces the maximum possible occupancy of the upper level, and therefore reduces the photocurrent.

In the transition region from the PL to the PC regime the photocurrent for a π pulse increases steeply. This shape can only be explained if the slow tunneling of the heavy-hole is included in the theory.

A simple approach to include this issue in the calculation, is an iterative method. As a first step (n=1), the differential equations 6.24–6.28 and 6.32 are solved with the TLS completely relaxed into the ground state, expressed by:

$$\rho_{00}(t = 0, n = 1) = 1 \tag{6.34}$$
$$\rho_{11}(t = 0, n = 1) = 0 \tag{6.35}$$
$$\rho_{hh}(t = 0, n = 1) = 0 \tag{6.36}$$
$$\rho_{10}(t = 0, n = 1) = 0 \tag{6.37}$$
$$\rho_{e}\ (t = 0, n = 1) = 0 \tag{6.38}$$

Thereafter the iteration is done by using the value of the density matrix elements at the point of time T_{rep} as new start values:

$$\rho_{00}(t = 0, n + 1) = \rho_{00}(t = T_{rep}, n) \tag{6.39}$$
$$\rho_{11}(t = 0, n + 1) = \rho_{11}(t = T_{rep}, n) \tag{6.40}$$
$$\rho_{hh}(t = 0, n + 1) = \rho_{hh}(t = T_{rep}, n) \tag{6.41}$$
$$\rho_{e}\ (t = 0, n + 1) = \rho_{e}\ (t = T_{rep}, n) \tag{6.42}$$
$$\rho_{10}(t = 0, n + 1) = \rho_{10}(t = T_{rep}, n) \tag{6.43}$$

The iteration converges very quickly, usually the error in the photocurrent is less than 2% after the second step.

It is also possible to derived an analytical solution from the equations 6.39–6.43 for $n \to \infty$, at least for some special cases. In the following is assumed, that the system is coherently prepared with a sufficiently short pulse and the electron relaxation time is much shorter than T_{rep} (that means, $\rho_{11}(t = T_{rep} \approx 0)$ and $\rho_{e}(t = T_{rep}) \approx 0$). After the coherent manipulation,

the upper level takes the value

$$\rho_{11} = \Theta\big(1 - \rho_{hh}(t = 0, n \to \infty)\big), \tag{6.44}$$

where Θ is the pulse area. Therefore, the important value which has to be calculated is the occupancy of the heavy-hole. After some algebra the equation

$$\rho_{hh}(t = 0, n \to \infty) = \frac{\Theta p(T_{rep})}{1 - e^{-\gamma_{hh} T_{rep}} + \Theta p(T_{rep})} \tag{6.45}$$

is derived. Therein $p(t)$ is the probability that the occupation from the upper level (ρ_{11}) is transferred to the heavy-hole level (and is not transferred to the ground state) after the time t. The expression

$$p(t) = \frac{\gamma_e}{\gamma_{hh} - (\gamma_e + \gamma_r)} \left(e^{-\gamma_{hh} t} - e^{-\gamma_e t)}\right) \tag{6.46}$$

is derived from 6.25–6.28, with $\Omega_0(t) = 0$.

The photocurrent for a single pulse with the pulse area Θ can then be calculated by modifying equation 6.29 to

$$I_{PC} = f e \eta \big(1 - \rho_{hh}(t = 0, n \to \infty)\big), \tag{6.47}$$

using the equation 6.45 for the steady state occupancy of the heavy-hole state.

Incoherent Background

When measuring Rabi oscillations one observes with increasing incident power continuously increasing background current. This background current scales linear with the intensity and is therefore attributed to incoherent absorption processes in the photodiode (e. g. from other QDs in the surrounding). As the background is proportional to the intensity—and therefore proportional to $\Omega_0(t)^2$—it can be included by modifying equation 6.32 in the following way:

$$\frac{d}{dt} I_{PC} = \cdots + \alpha_{bg} \Omega_0(t)^2. \tag{6.48}$$

The coefficient α_{bg} depends on the applied bias voltage, because at high electric fields more incoherently excited charge carriers contribute to the signal. To achieve a very high correspondence with the experiments, it is sufficient to assume a linear dependency, although this might not be exact.

6.4 Summary – A Complete Set of Equations

In summary, the equations 6.24-6.28, 6.32, 6.48, and (the later derived equation) 7.11 are used to describe the exciton TLS. The following complete set of equations is obtained:

$$\frac{d}{dt}\tilde{\rho}_{01} = i\frac{\Omega_0}{2}e^{i\phi}\left(\rho_{11}e^{-i\phi} - \rho_{00}e^{i\phi}\right) - i\delta\tilde{\rho}_{01} - \left(\frac{\gamma_r + \gamma_e + \gamma_{hh}}{2} + \gamma_2^* + \gamma_I(\Omega_0)\right)\tilde{\rho}_{01} \tag{6.49}$$

$$\frac{d}{dt}\rho_{00} = i\frac{\Omega_0}{2}\left(\tilde{\rho}_{10}e^{i\phi} - \tilde{\rho}_{01}e^{-i\phi}\right) + \gamma_r\rho_{11} + \gamma_{hh}\rho_{hh} + \gamma_e\rho_e \tag{6.50}$$

$$\frac{d}{dt}\rho_{11} = i\frac{\Omega_0}{2}\left(\tilde{\rho}_{01}e^{-i\phi} - \tilde{\rho}_{10}e^{i\phi}\right) - \left(\gamma_r + \gamma_e + \gamma_{hh}\right)\rho_{11} \tag{6.51}$$

$$\frac{d}{dt}\rho_{hh} = \gamma_e\rho_{11} - \gamma_{hh}\rho_{hh} \tag{6.52}$$

$$\frac{d}{dt}\rho_e = \gamma_{hh}\rho_{11} - \gamma_e\rho_e \tag{6.53}$$

$$\frac{d}{dt}I_{PC} = \gamma_e\rho_{11} + \gamma_{hh}\rho_{11} + \alpha_{\mathrm{bg}}\Omega_0(t)^2 \tag{6.54}$$

These equations ares used to simulate the exciton TLS with all its features under consideration of equation 6.33 and 6.39–6.43. The numerical calculations are performed with MATLAB, using build-in a forth-order Runge-Kutta algorithm.[106] In the next chapter the experimental results from PC spectroscopy are compared to the simulation.

7 Quantum Optical Properties of a Single QD Exciton

In this chapter the quantum optical properties of a single exciton, confined in a QD, are discussed. By comparison of the experimental results with theoretical model, derived in the previous chapter, the assumptions of the model are confirmed.

7.1 Optical Properties Under Continuous Excitation

The optical properties of the exciton TLS under continuous excitation are regarded in this section. The corresponding experiments have been performed earlier, but the interpretation presented by E. Beham, S. Stufler and P. Ester[35,89,107,108] neglects the two-step relaxation. The new and more accurate model presented here leads to a significant deviation of the derived parameters (by a factor of about 2 for the slow tunneling constant), making a reinterpretation of the results necessary.

In case of continuous excitation with a spectral narrow (monochromatic) laser source, two important effects can be observed: *saturation* and *power broadening*. Both rely on the same mechanism: the average occupation of the upper level of a TLS cannot exceed 1/2 for resonant (or detuned) excitation due to stimulated emission.

The statistics of the occupation of the upper and lower levels can be derived in two ways. Either one analyzes the optical Bloch equations in the limit of long times $t \to \infty$, or by using rate equations using the Einstein-coefficients for absorption, simulated and spontaneous emission (and here also for the tunneling decay). A derivation without the single heavy-hole and the single electron level can be found in reference [102] for a two-level atom or in the dissertation of Patrick Ester,[35] where this derivation is adapted to an exciton TLS. The considerations in this section include the single heavy-hole and electron states, but the derivation follows more or less the same scheme. A general condition in all approaches is of course, that the sum of the occupancy of all involved quantum states is always 1:

$$\rho_{00}(t) + \rho_{11}(t) + \rho_{hh}(t) + \rho_{e}(t) = 1 \qquad \forall\, t \tag{7.1}$$

Saturation

To describe the saturation behavior for resonant excitation, the easiest way is to use the rate equation approach. Using the same nomenclature as before, and introducing and the excitation intensity $\widetilde{P}$ and the factor M, reflecting the probability for the stimulated processes

(following the convention from Beham et al.[109]), the rate equations can be written in the following form:

$$\frac{d}{dt}\rho_{00} = -\rho_{00}M\widetilde{P} + \rho_{11}M\widetilde{P} + \gamma_r\rho_{11} + \gamma_{hh}\rho_{hh} + \gamma_e\rho_e \tag{7.2}$$

$$\frac{d}{dt}\rho_{11} = +\rho_{00}M\widetilde{P} - \rho_{11}M\widetilde{P} - \left(\gamma_r + \gamma_e + \gamma_{hh}\right)\rho_{11} \tag{7.3}$$

$$\frac{d}{dt}\rho_{hh} = \gamma_e\rho_{11} - \gamma_{hh}\rho_{hh} \tag{7.4}$$

$$\frac{d}{dt}\rho_e \;\; = \gamma_{hh}\rho_{11} - \gamma_e\rho_e \tag{7.5}$$

Under the steady state condition, all derivation are zero. Hence, under continuous excitation the occupancy of ρ_{hh} and ρ_e can be expressed by

$$\rho_{hh} = \frac{\gamma_e}{\gamma_{hh}}\rho_{11}, \quad \text{and} \quad \rho_e = \frac{\gamma_{hh}}{\gamma_e}\rho_{11}, \tag{7.6}$$

respectively. The PC is given by the tunneling decay of the upper level times the elementary charge:

$$I_{PC} = e\rho_{11}(\gamma_e + \gamma_{hh}) \tag{7.7}$$

The occupancy of the upper level for the normalized incident intensity $\widetilde{P}$ is derived after some algebra

$$\rho_{11} = \frac{1}{2 + \frac{\gamma_e}{\gamma_{hh}} + \frac{\gamma_{hh}}{\gamma_e}} \times \frac{\widetilde{P}}{\widetilde{P} + \frac{\gamma_r+\gamma_e+\gamma_{hh}}{M\left(2+\frac{\gamma_e}{\gamma_{hh}}+\frac{\gamma_{hh}}{\gamma_e}\right)}} \tag{7.8}$$

The second term determines how fast the steady state is reached with increasing excitation intensity. In the limit of $\widetilde{P} \to \infty$ the second term equals 1, and the occupancy of the upper level is given by the first term, which is always smaller than $1/2$. Thus, with increasing intensity the PC saturates to a value determined by γ_{hh} and γ_e.

The here presented model is inconsistent with the model developed by Beham et al.[109] As a matter of fact, for the QD investigated in [35, 89, 108], which is also used in this thesis, the derived value for the heavy-hole tunneling differs by a factor of about 2. For example, in the experimental data presented in figure 7.1, the saturation current of 74.5 pA results in a heavy-hole tunneling time of about 2 ns, calculated using the new model, in contrast to the value of 1 ns, derived with the old model. The mathematical reason for the deviation is the two-step relaxation process which reduces the occupancy of the upper level to a value less than 1/2.

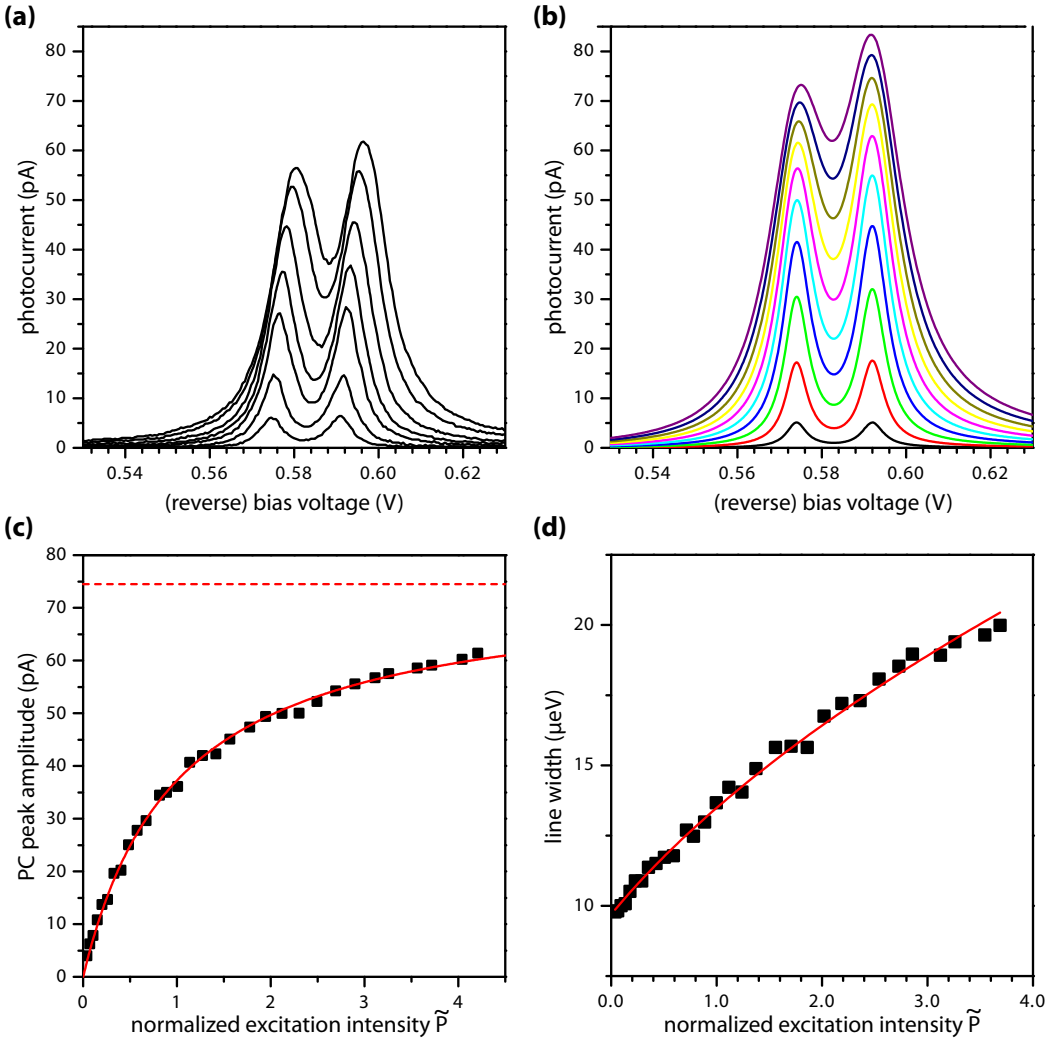

Figure 7.1: (a,b) Comparison of the experimental results and theoretical calculations. The calculation is based on the extended optical Bloch equation, which are solved numerically for a cw light field by integrating a long time. The asymmetric broadening is clearly visible, as well as the higher saturation current of the right peak due to the decreasing heavy-hole tunneling time at higher bias voltages. The slight shift of the peak position is not included in this theoretical model. (c) PC signal of the left peak with increasing power. Because the tunneling times of the theoretical model are derived from the fit curve, the theoretical model delivers, by construction, exactly the same curve. (d) Broadening of the peak

Power broadening

The inherent dephasing time of a TLS gives a lower limit for its homogeneous line width[110]

$$\Gamma_{hom} = \frac{2\hbar}{T_2}, \tag{7.9}$$

therefore, the dephasing constant, here composed of $\gamma_r + \gamma_e + \gamma_{hh}$, can be measured by analyzing the spectral width of the TLS. In the photocurrent regime the relation $\gamma_e > \gamma_r \gg \gamma_{hh}$ is valid, thus the dephasing can be attributed mainly to γ_e, with an error in the order of $\gamma_e/(\gamma_e + \gamma_r + \gamma_{hh})$. This corresponds to the earlier interpretations in[35, 89, 107, 108].

With increasing excitation power the linewidth of a TLS in the absorption (PC) spectrum broadens as a direct consequence of the saturation behavior at slightly detuned excitation. At resonance, the absorption saturates faster as compared to the saturation of the absorption at detuned excitation. This results in a broadening of the absorption line, referred as *power broadening* in the literature. For a Lorentzian line shape of the width Γ_0, the power broadened peak is again Lorentzian with the increased width[108]

$$\Gamma = \Gamma_0 \sqrt{1 + \widetilde{P}} \tag{7.10}$$

This equation can be derived form an analysis of the optical bloch equations for $t \to \infty$. Because the power broadening effect can be easily calculated with the presented model (6.24–6.28), a detailed analytic derivation is omitted here.

In the experimental data shown in figure 7.1c, a slight shift of the resonance energy towards hight voltages as the excitation power increases is obvious. An analysis of the peak position suggest electrostatic shielding to be responsible for this effect.[89]

7.2 Rabi Oscillations and Excitation Dependent Damping

Rabi oscillations are a fundamental example of coherent non-linear light matter interaction. The exciton TLS Rabi oscillation have been observed by several groups utilizing different detection methods.[36,42,111–115] In all experimental data the Rabi oscillations exhibit a dephasing at higher pulse areas (see figure 7.2). This driving-dependent dephasing is obviously not included in the theory presented above.

The phenomenon has been discussed controversially in several theoretical papers in the last years. One early proposal by J. Villas-Bôas et al. was, that this damping is related to the excitation of the biexciton.[116] Although their calculations can reproduce the experimental data from [117] very well, the damping also occurs when the biexciton generation is efficiently suppresses, which can be achieved by excitation with circular-polarized light.

A very common thesis concerning the damping mechanism is the coupling to acoustic phonons (see e.g. Förstner et al.[118] and Krügel et al.[119]). Remarkable on the phonon thesis are predictions of an undamping under special conditions,[120] which has not been observed

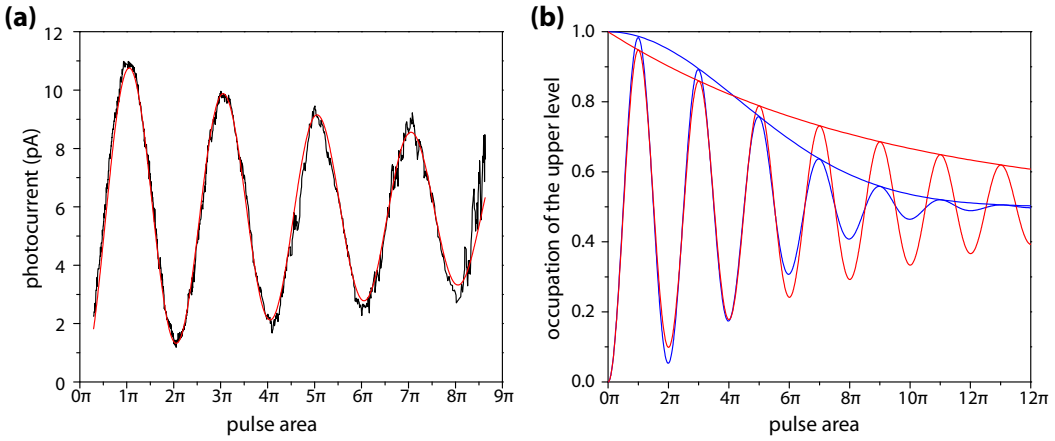

Figure 7.2: A comparison between the experimental data and the damping model

experimentally, yet. A proof of the interaction with phonons should be possible by temperature dependent measurements (see PhD thesis of M.C. Hübner[90]) and by using pulse shaping technics, to vary the laser pulse length. Very recently, A. Ramsay et al. published a paper which strongly support this thesis with experimental data acquired by such measurements.[121]

A more general approach, which is compatible to the phonon thesis, is presented by Mogilevtsev et al.[122,123] They showed that the coupling to a non-Markovian reservoir leads directly to a dependence of the dephasing on the excitation intensity.

To include the excitation dependent damping in the optical bloch equations, a field dependent damping constant γ_I is introduced:

$$\gamma_I(\Omega_0(t)) = \beta_1\Omega_0(t) + \beta_2\Omega_0(t)^2 \tag{7.11}$$

This has also been done by Brandi et al.[124] to resample the data form [117]. A more reliable data set from precise experiments is presented in figure 7.2a. The red curve in this diagram is a least square fit to the data using the expression

$$I_{PC} = I_{1/2} + I_A \sin(\omega\Theta + \phi)e^{-\gamma\Theta}, \tag{7.12}$$

where $I_{1/2}$ is the mean PC value of the oscillation. I_A, ω, and ϕ are the oscillation amplitude, frequency, and phase, respectively. The pulse area is denoted by Θ and the dephasing constant by γ. The fit correlates very well with experimental data, especially at low pulse areas. At higher pulse areas a small difference arise, but there also the noise in the data increases due to the increasing incoherent background, which has been subtracted here. The reason of this noise are small variation of the laser intensity of a few percent, which is linearly transferred to the background current and with the square root of the intensity to the coherent signal.

Thus, it turns out that the damping can be well described with a pure exponential decay with increasing pulse area, here. Therefore, the linear damping term in the equation 7.11 is sufficient to achieve a good coincidence between experiment and simulation. However, to test the significance of this result, the Rabi oscillations were also simulated with the quadratic dephasing term. Figure 7.2b shows the calculated result for a pure linear (red curve) and pure quadratic term (blue curve). The dashed lines correspond to the exponential decay part of the functions. For the red curve this is proportional to $\exp(-\gamma\Theta)$ and for the blue curve $\exp(-\gamma\Theta^2)$.[(a)] The decay is very similar for the first three periods, and a significant difference appears only a higher pulse areas.

To conclude this comparison, the intensity dependent damping of the Rabi oscillation as observed here at low temperature can be well described with a linear dephasing term in the optical Bloch equations. A pure quadratic dephasing term (which is proposed by A. Ramsay et al.[121]) seems very unlikely, as it does not fit very well to the data. However, an additional contribution from a quadratic damping term cannot be excluded, because a small quadratic dephasing will be only important at higher pulse areas.

7.3 Double-Pulse Experiments

As mentioned before in section 6.2, double pulse experiments are the method of choice to get information about the coherent dynamics of a TLS, here of the exciton system. In this section the three different experiments inversion recovery, quantum interference, and Ramsey interference are regarded. To simplify the things,the possibility that the heavy-hole could tunnel first is neglected in this section. The thereby introduced error is usually smaller than the experimental errors.

7.3.1 Inversion Recovery

In the inversion recovery experiment the occupation is measured as a function of the time delay between to resonant π pulses.The method is similar to the inversion recovery method used by NMR and electron spin resonance (ESR) spectroscopists.[125,126]

The sequence of the experiment can easily explained with the help of the Bloch sphere representation. The first pulse rotates the Bloch vector through an angle $\Theta = \pi$ around the u axis. The system starts in the lower level $|0\rangle$, and thus it is inverted to the upper level $|X\rangle$. During the delay time, the vector slides down the w axis due to the exciton decay with the rate $\gamma_e + \gamma_r + \gamma_{hh}$ (T_1 decay). The second pulse inverts the state vector again ($w \Rightarrow -w$). The final state is thereby independent of the optical phase between the laser pulses, because the state vector has no component in u and v direction (i. e. $\rho_{10} = 0$) after the first (and also the second) pulse and so the quantum system has no measurable phase.

[(a)] Please note, that the relation between γ and $\beta_{1/2}$ is non-trival and no analytic expression can be given here.

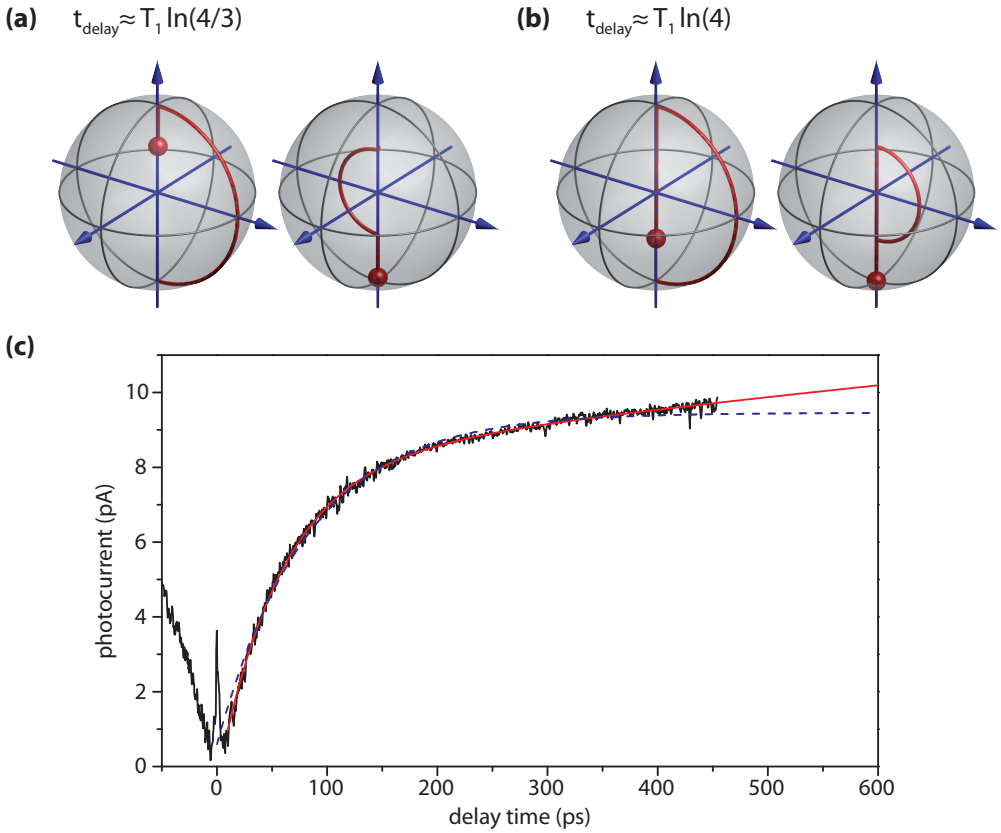

Figure 7.3: (a,b) Illustration of the inversion recovery experiment. *left spheres:* After the inversion by the first laser pulse the Bloch vector slides down along the *w* axis. *right spheres:* The second laser pulse performs a point reflection across the center of the Bloch sphere. After the second laser pulse the quantum state decays to the ground state. The resulting PC is proportional to the length of the vertical lines arising from the decay.
(c) PC signal of an inversion recovery experiment at 0.59 V. The incoherent background has been substracted from the PC. The red curve is a bi-exponential fit, delivering an electron and heavy-hole tunneling time of 60 ± 10 ps and 2050 ± 200 ps. The blue (dashed) curve is the best (mono-)exponential fit, revealing clearly the necessity of the two-step relaxation model.

The experiment can be used to characterize the decay of the upper level.[127] In the diagram 7.3, the PC is plotted against the delay time. The signature of a two-step decay through metastable level is visible in the bi-exponential curve shape. The PC curve can be fitted with the expression

$$I_{PC} = I_{2\pi} - A_e e^{-\gamma_e t_{delay}} - A_{hh} e^{-\gamma_{hh} t_{delay}} \tag{7.13}$$

For zero delay time, the PC should be equal to a 2π-pulse, which is—in theory—zero. However, if the delay time is shorter than the pulse length, the laser pulses can interfere optically. Therefore, the experiment is only evaluated for delay times larger than $2t_{delay}$. The experiment is in principle very simple, but the experimental realization is not trivial. For a solid data base, the delay time has to be changed from close to zero up to the order of the tunneling time of the heavy-hole. By doing so, the focus of the second laser pulse might change due to the divergence of the laser or a small misalignment of the interferometer. Then the second laser pulse is not a π pulse any more, but for example 0.9π or 1.1π pulse. Thus the experiment has to be carried out very carefully to avoid these errors. In conclusion, this experiment reveals the two-step relaxation process clearly. It is an interesting tool to get access to the heavy-hole tunneling time, which previously has only been obtained by cw measurement, which are not available for all material systems.

7.3.2 Quantum Interference

The basic quantum interference experiment is used to determine the coherence time of a quantum system. In this section it is assumed, that the quantum system is in (exact) resonance with the excitation ($\delta = 0$). As already explained in section 6.2, the first laser pulse shall create a coherent superposition between the $|0\rangle$ and $|X\rangle$ state. Thus, it is a fundamental requirement that it is not π pulse. As said before, $\pi/2$ pulses are an optimal choice for the investigation of the coherence time because the interference amplitude is maximum in this case. The first coherent manipulation determines the quantum phase of the exciton. Because of the assumption that the quantum system is in exact resonance with the light field, the azimuthal angle of the Bloch vector (representing the phase of the quantum system) does not change during the delay time. After the delay time t_{delay}, the second laser pulse arrives and interferes with the quantum system. The resulting quantum state of the exciton depends now in the optical phase of second laser pulse. If the system underlies a dephasing due to pure dephasing or population decay, a mixed quantum state is created which lies inside the Bloch sphere and the interference amplitude measured in the PC decreases.

The procedure of a quantum interference experiment is usually the following: For each delay time t_{delay}, the phase of the second laser pulse is varied by means of a precise additional delay, controlled via the nanopositioner. To evaluate the decoherence time, the interference amplitude is plotted against the delay time and fitted with an exponential decay expression. This procedure has the advantage, that the incoherent background current is not relevant for the evaluation of the dephasing rate.

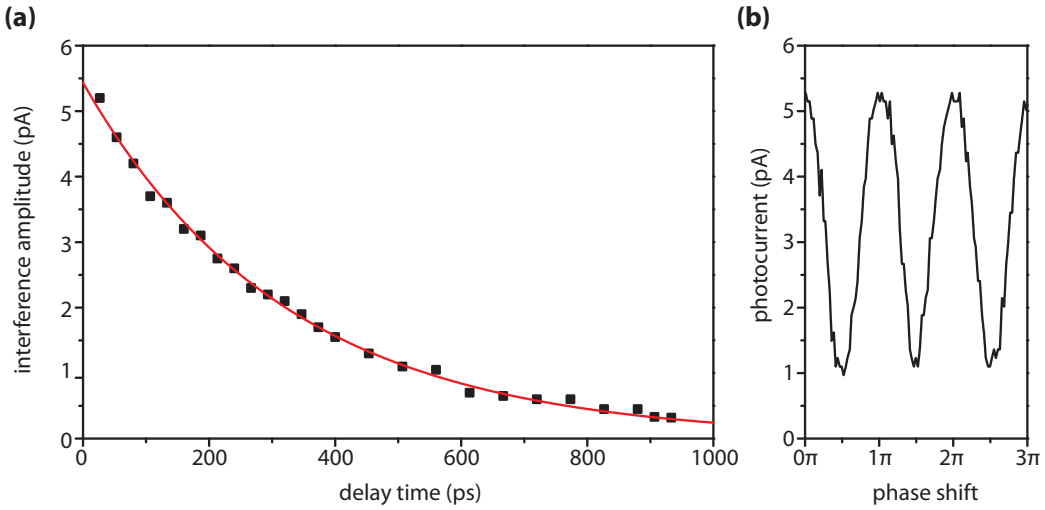

Figure 7.4: (a) Decay of the resonant quantum interference amplitude at a bias voltage of 0.4 V. The data is fitted with an exponential decay with a dephasing constant of 320 ± 5 ps. (b) The photocurrent signal of the quantum interference at a delay time of 55 ps.

Figure 7.4a shows the decay of the quantum interference amplitude at a bias voltage of 0.4 V. The data is fitted with an exponential decay, delivering a dephasing constant of 320 ± 5 ps. This dephasing constant is composed of the radiative decay constant and the electron tunneling constant.

7.3.3 Influence of Detuning

In case of (slightly) detuned excitation ($\delta \neq 0$), a single laser pulse rotates the Bloch vector not around the u axis but around the axis given by the vector $[-\Omega(t), 0, -\delta]$. Therefore, the complete inversion of the state cannot be reached any more with a single pulse. As a consequence, the Rabi frequency is increased to $\Omega' = \sqrt{\Omega^2 + \delta^2}$. Figure 7.5a visualizes the trajectory of a detuned 2π pulse. In a quantum interference experiment, the effect of detuning can result in a quite complex trajectory of the Bloch vector. In reference [128], we showed this for the excitation with two partly overlapping 0.8π pulses. By changing phase and detuning, the obtained final states can cover the whole Bloch sphere.

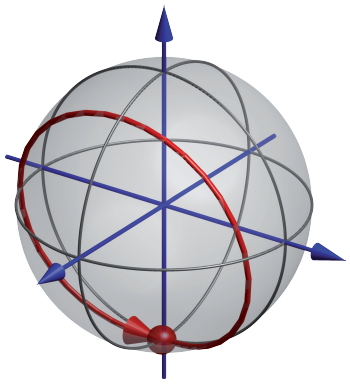

Figure 7.5: Trajectory of a detuned 2π pulse.

8 Coherent Optoelectronic Control

In the previous chapters the exciton in a QD has been treated as a two-level system, and by comparison of the experimental data with the theoretical model this perception has proven its eligibility. In the field of quantum information a quantum mechanical TLS is regarded as a qubit, and so the here presented exciton TLS can be considered as a qubit implementation.

The exciton qubit can be coherently controlled by resonant and detuned excitation with a very high fidelity by ultrafast laser pulses, as shown before. However, it is impossible or at least very difficult to control such ultrafast laser pulses from pulse to pulse concerning intensity, energy, and phase. In this chapter it is demonstrated, that a coherent phase control can be achieved by electric interaction. Thereby, it is possible to restrict the optical excitation to a fixed optical clock with constant intensity, energy, phase, and pulse distance, while a synchronous electric gate signal controls the coherent manipulation.

At first, the Ramsey interference experiment is described, from which the basic principle of the coherent electric manipulation is derived. Afterwards, the concept of the coherent electric control is explained and a new quantity—the *electric pulse area*—is introduced. The concept is proven by an experimental demonstration of a quantum phase gate, which is capable to shift the exciton qubit phase between 0 and π, controlled by the electric parameters of a 2.4 GHz RF signal. In the last part of this chapter, the concept is generalized and it is explained, how an universal single qubit control can be achieved by the presented scheme.

8.1 Ramsey Interference: Static Phase Shift

The basic principle of the coherent electric control is derived for the *Ramsey interference* experiment, which is a remarkable modification of the quantum interference experiment. Thereby, the delay time between the two laser pulses, as well as their phase relation, is fixed and the energy of the quantum system is moderately detuned. N. F. Ramsey discovered, that in such a configuration the spectral sensitivity of a TLS is substantially enhanced.[129] The effect is well known from atomic optics and has nowadays several applications in precision spectroscopy and atomic clocks. N. F. Ramsey was awarded the Nobel Prize in 1989 for the discovery of this effect.

The optical pulse sequence is the same as for the basic quantum interference experiment. At first, a $\pi/2$-pulse turns the qubit in a superposition state between $|0\rangle$ and $|1\rangle$, which falls on the equator of the Bloch sphere. In the terminology of QIP, this coherent manipulation is also known as Hadamard gate. The quantum phase of the exciton qubit in this superposition is defined by the optical phase of the laser pulse, and the phase is stored in the exciton qubit

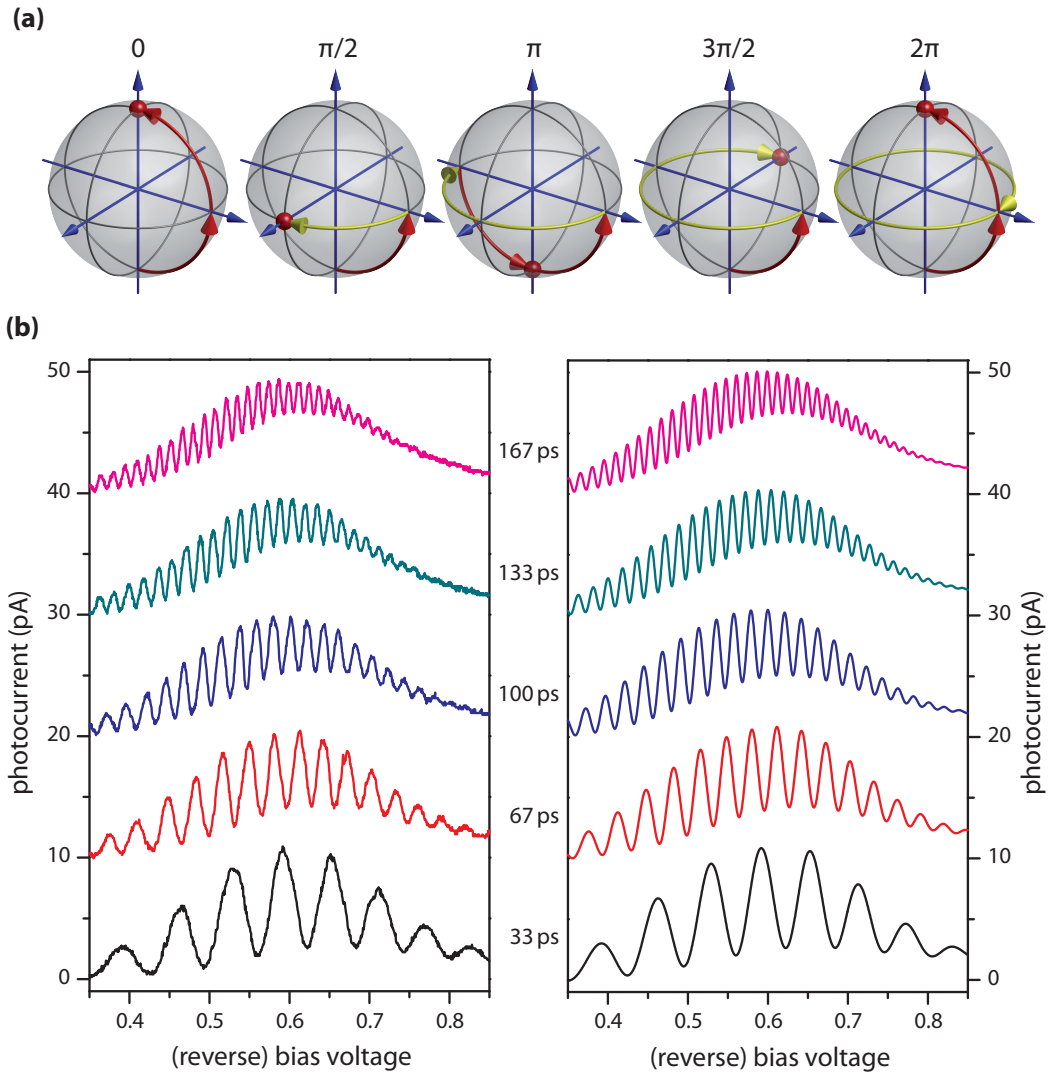

Figure 8.1: (a) Trajectories of the Bloch vector on the Bloch sphere during a Ramsey experiment for different detuning: from resonance (left) to a detuning, which leads to a phase shift of 2π (right). The yellow arrow indicates the rotation of the Bloch vector during the delay time due to the detuning. The final state is indicated by the red ball.
(b) *left*: PC signal of a Ramsey experiment with increasing delay time (published in [130–133]). *right*: corresponding theoretical calculation, based on the equations 6.49–6.54. The phase relation between the two laser pulses is not constant for the different delay times, in order to fit to the experimental data. The dephasing constants were taken from the cw experiments and quantum interference experiments.

during the coherence time. After a time delay, the phase of the exciton qubit is probed by quantum interference with a second $\pi/2$ laser pulse (second Hadamard gate operation). Depending on the momentary phase of the exciton after the delay time, and the optical phase relation between two pulses, the second $\pi/2$-pulse will rotate the Bloch vector to its final state.

In the case of detuning, the Bloch vector will rotate along the equator of the Bloch sphere with detuning δ, defined by $\delta = \omega_{laser} - \omega_{01}$, during the delay time of the two laser pulses. Thus, within the delay time t_{delay} between the two laser pulses, a phase difference of

$$\Delta\phi = \delta \times t_{delay} \tag{8.1}$$

between the laser field and the exciton qubit is acquired. For two in-phase laser pulses, the trajectory of the Bloch vector on the Bloch sphere is displayed for different effective phase shifts (but without dephasing) in figure 8.1a. The in-plane rotation of the Bloch vector due to the detuning is indicated by the yellow arrows on the Bloch spheres.

The detuning is controlled by the bias voltage V_{bias} via the QCSE. As a function of the detuning the phase changes, which leads to an oscillation of the final state between $|0\rangle$and $|1\rangle$. This oscillation appears as Ramsey fringes in the photocurrent. From equation 8.1 one can conclude, that the frequency of the fringes increases directly proportional to the delay time between the two pulses. Figure 8.1b show a measurement of Ramsey fringes at delay times ranging from 33 ps to 167 ps. The corresponding calculated data is shown besides the experimental data. In the lowest curve of theoretical data the resonance ('0') and the phase shifts of the adjacent minimum ('π') and maximum ('2π') are marked.

At a low bias voltage (close to 0.4 V), where the dephasing times are longer, it is possible to record the Ramsey fringes at a very long delay time. As previously shown (e. g. in the PhD thesis of S. Stufler[89]), it is possible to achieve a resolution (here defined as half period of the Ramsey fringes) which is smaller than the homogeneous linewidth of the system (5 μeV).

In a detailed analysis of the data one notices a slight increase of the frequency of the Ramsey fringes towards higher voltages. This is caused by the quadratic dependence of the QCSE with the voltage. The simultaneous decrease of the interference amplitude is caused by the voltage dependence of the dephasing times. The envelope of the PC signal corresponds basically to the spectrum of a single pulse with a pulse area of $\pi = 2 \times \pi/2$. The non-oscillatory part of the PC is determined by the dephasing of the exciton qubit between the two laser pulses. It becomes the dominant part of the PC signal for longer delay times and higher voltages.

Figure 8.2 shows a detail of a Ramsey fringes dataset, recorded with a delay time of 208 ps. The red line marks the bias voltage V_{res}, at which the exciton qubit is in resonance with the light field, in this case $V_{res} = 0.456$ V. Below the bias voltage scale, the frequency detuning between the quantum system and the light field is indicated. The scaling of the frequency axis is derived from the QCSE. In this case, the QCSE is approximated as a linear effect, which is a good assumption for the here regarded relative small detuning range. At resonance, the exciton, as well as the light field, has a frequency of 323.4449 THz. Detuning the qubit to 323.4401 THz, which is 4.8 GHz below the resonance frequency, implies, that the qubit

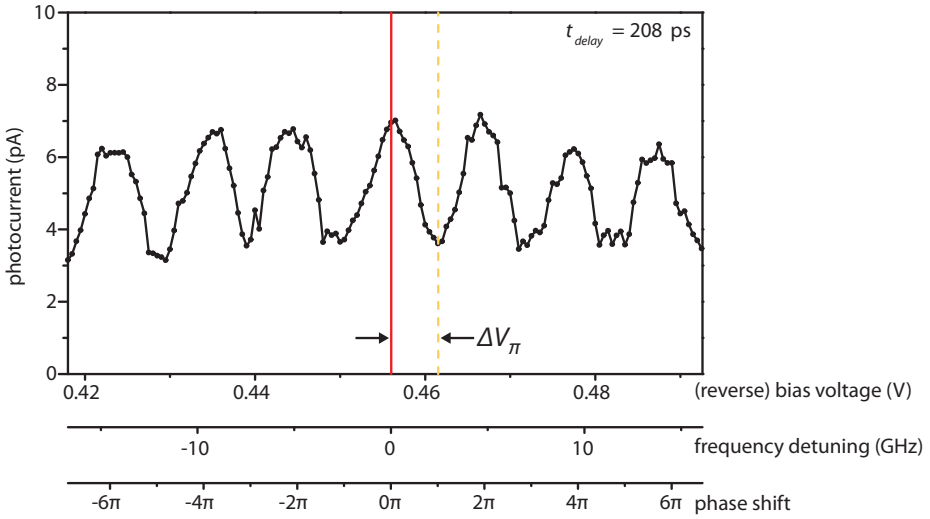

Figure 8.2: Detail of a Ramsey interference data set. The upper axis shows the (reverse) bias voltage. The corresponing frequency shift from the resonance (vertical red line) is plotted on the middle axis. The lower axis denotes the relative phase shift between the quantum system and the light field. The orange dashed line indicates the offset voltage required to achieve a phase shift of π.

performs one oscillation less than the light field during the given delay time. The acquired phase shift is given by:

$$\phi = 2\pi \times (\nu_{qubit} - \nu_{laser}) \times t_{delay} = 2\pi \times 4.8\,\text{GHz} \times 208.3\,\text{ps} = 2\pi \times 1. \tag{8.2}$$

Thus, the qubit has acquired a phase shift of 2π during the delay time in respect to the reference phase of the light field, and the frequency shift can be converted to a phase shift, shown on the lower axis of the diagram.

The dashed orange line indicates a phase shift of π, which is necessary to switch from constructive to destructive interference. The difference between V_{res} and the bias voltage, which is required for a phase shift of π during the delay time t_{delay}, is here called ΔV_π.

8.2 Coherent Electric Phase Manipulation

The coherent electric phase manipulation is based on the adiabatic temporal detuning of the system within the delay time between two laser pulses. The schematic timeline of the concept of the coherent manipulation by an electric pulse is shown in figure 8.3. Throughout this chapter, the optical manipulation is indicated in red, while the coherent electrical manipulations is

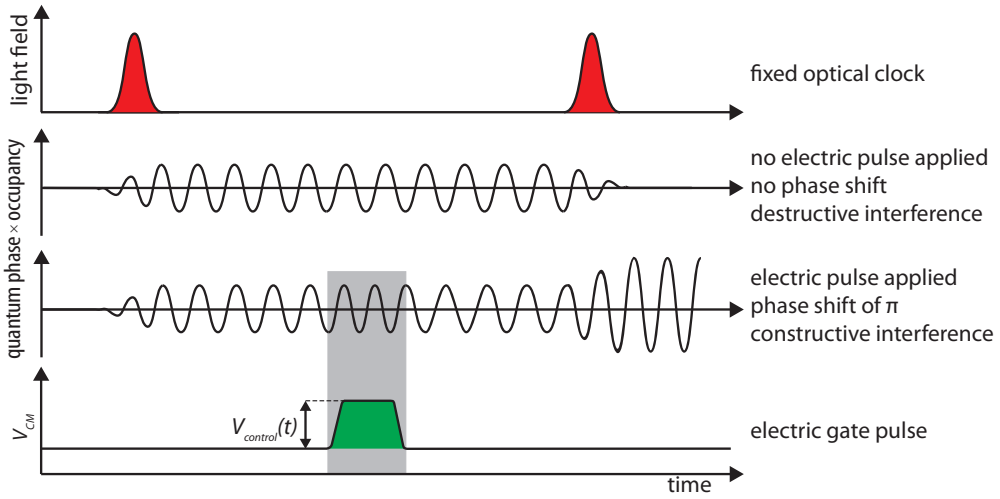

Figure 8.3: Schematic timeline of the optoelectronic phase control (not to scale). The pulse area (red) of the first pulse of the optical clock creates a coherent superposition state, indicated by product of the occupancy of the upper level ρ_{11} and the quantum phase. The second pulse probes the quantum phase. Depending on the coherent manipulation of the quantum phase of the qubit due to the electric pulse area (green), the qubit shows constructive or destructive interference.

indicated in green.

The detuning is controlled by the applied coherent manipulation voltage $V_{CM}(t)$, which is the difference between the applied voltage between the applied voltage $V_{control}(t) + V_{bias}$ and the voltage V_{res}, at which the exciton qubit is in resonance with the light field:

$$V_{CM}(t) = V_{control}(t) + V_{bias} - V_{res}. \tag{8.3}$$

To describe the optoelectronic phase control, it is convenient to define an electric pulse area analogous to the optical pulse area, introduced in chapter 6. The optical pulse area describes the rotation of the Bloch vector around an axis in the uv-plane (for resonant excitation and depending on the phase) in contrast to the electric pulse area, which is responsible for the rotation of the Bloch vector around the w-axis, which is essentially the quantum phase of the qubit. The total phase shift (equal to the rotation angle) induced by electric manipulation during the delay time of the two pulses is given by

$$A_{el} = C_{CM} \int_0^{t_{delay}} V_{CM}(t)dt. \tag{8.4}$$

where $V_{CM}(t)$ is responsible for the coherent manipulation and C_{CM} is the coherent electric

manipulation coefficient (EMC). The unit of the EMC is $[C_{CM}]$ = 1/Vs; its magnitude is controlled by the steepness of the voltage induced shift of the transition energy resulting from the Stark effect. The EMC can be obtained from voltage controlled Ramsey experiments as inverse product of t_{delay} and the necessary voltage shift to achieve a qubit phase shift of π:

$$C_{CM} = \frac{1}{V_\pi t_{delay}}. \tag{8.5}$$

From the data shown in figure 8.2 a (inverse) EMC of $1/C_{CM} = 1.15 \pm 0.05$ V ps is obtained for the specific exciton qubit.

8.3 Experiment

To detect the electric phase manipulation, Ramsey interference experiments are performed, similar to the experiments explained before. Within these experiments, coherent qubit manipulations by transient electric control for the condition of fixed optical excitation conditions are demonstrated. The optical excitation from the mode-locked Ti:Sapphire laser is thereby used as an optical clock signal, with consists of a stream of double pulses from the Michelson interferometer with constant delay, constant phase relation, and constant pulse area ($\pi/2$). Further, an electric control signal, applied synchronously to the optical clock, is required for the demonstration of the coherent optoelectronic control of the exciton qubit. For the electric qubit manipulation, only the electric signal applied during the time interval between the ps pulse pair effects the quantum interference.

8.3.1 Single Pulse Experiment

The first and obvious approach is to use a short electric pulse, placed between the two laser pulses (like in figure 8.3). Considering the dephasing time of the exciton qubit, the delay time is limited to approximately 600 ps for low bias voltages. With the electronics described in chapter 4.5 it is possible to create an electric pulse with a FWHM of less than 450 ps, analyzed directly behind the second comparator with a 6 GHz real-time oscilloscope. This pulse is transferred to the QD photodiode by the RF network shown in figure 8.4a. It turns out, that the electric signal is capable to switch the PC signal from the constructive interference to the PC value expected for destructive interference. However, due to the LRC-time constants of the sample and its wiring, it is expected that the electric pulse underlies a dispersion. To analyze the dispersion, the electric pulse is shifted in respect to the optical clock signal by the electronic control and an external delay box, as shown in figure 8.4b. Thereby, the quantum system is utilized as a kind of oscilloscope. The diagram (figure 8.4c) shows the resonant PC response of the QD at a bias voltage of $V_{bias} = V_{res} = 0.5$ V and a delay time of $t_{delay} = 50$ ps between the two laser pulses. The grey curve represents the original obtained PC data, while the red curve is derived by smoothing this data to reduce the noise.

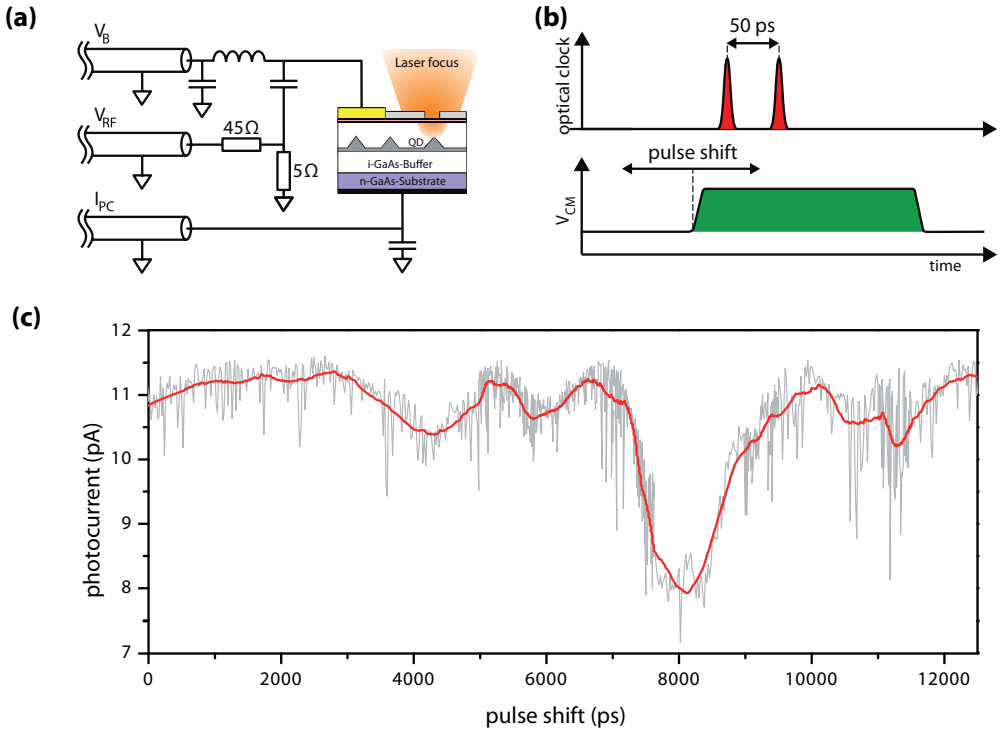

Figure 8.4: (a) The photodiode with the RF coupling network. (b) Sketch of the timeline of the experiment. (c) PC response as a function of the pulse delay of the electric pulse in respect of the optical clock.

In the region of a pulse shift of 5000 ps to 7000 ps the PC is lowered to the level of destructive interference in a quantum interference, thus the quantum phase is shifted by π at this point. The FWHM of this dip is approximately 1.2 ns, meaning that the electric pulse has broadened due to the dispersion. At other pulse shifts, the PC signal is also affected, thus the signal of the electric pulse is not limited to the dip (e. g. at 4000 ps).

In a strict interpretation of this experiment, there is no essential difference to the classical Ramsey interference experiment, because although an electric pulse is applied to the photodiode, the electric field between the two laser pulses remains (more or less) constant. Due to the broadening of the electric pulse to more than a nanosecond, it is not possible to increase the optical delay time to an appropriate value, so that the electric pulse is enclosed between the optical pulses.

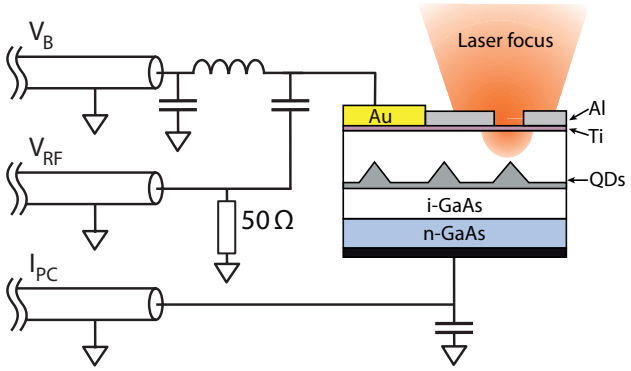

Figure 8.5: The photodiode with the coupling network for the 2.4 GHz RF signal.

8.3.2 RF Signal Experiment

To avoid the problems arising from the dispersion of the electric signal, now a single frequency RF signal is used to demonstrated the coherent phase manipulations. Such a signal underlies of course also a dispersion due to the inductances and capacities of the sample and its wiring, however, these change only phase and amplitude of the signal, which can be compensated in advance.

The fundamental requirement to the signal is its synchronism with the optical clock, thus one has to take a higher harmonic of the laser repetition frequency. For the creation of the time correlated electric signal, here the 30th harmonic of the laser repetition frequency (80 MHz) is used, as explained in chapter 4.5. The thereby obtained 2.4 GHz radio frequency (RF) signal has a defined phase relation with respect to the laser pulses. The phase of this signal can be swept continuously by electronic control and the amplitude can be adjusted by a series of attenuators. The signal can be described by

$$V_{RF}(t) = V_{RF_0} \sin(\omega_{RF} t + \phi_{RF}), \tag{8.6}$$

where V_{RF_0} and ω_{RF} are the amplitude and angular frequency of the RF signal, respectively. The phase ϕ_{RF} is define to be zero for the situation displayed in figure 8.6a.[(a)] The RF signal is applied to the QD PD by superimposing it with the DC bias voltage V_{bias}. As shown in figure 8.5, V_{RF} is terminated (50 Ω) and capacitively coupled to the gate electrode of the PD. It is important to note, that the chosen time delay between the two laser pulses (t_{delay} = 208 ps) is set exactly to the half period time of the RF signal. This means in particular that one can continuously sweep between the situations, where the upper or the lower half wave of the RF signal is lying exactly between the two laser pulses.

[(a)] Here, $t = 0$ is the point of time of the first laser pulse.

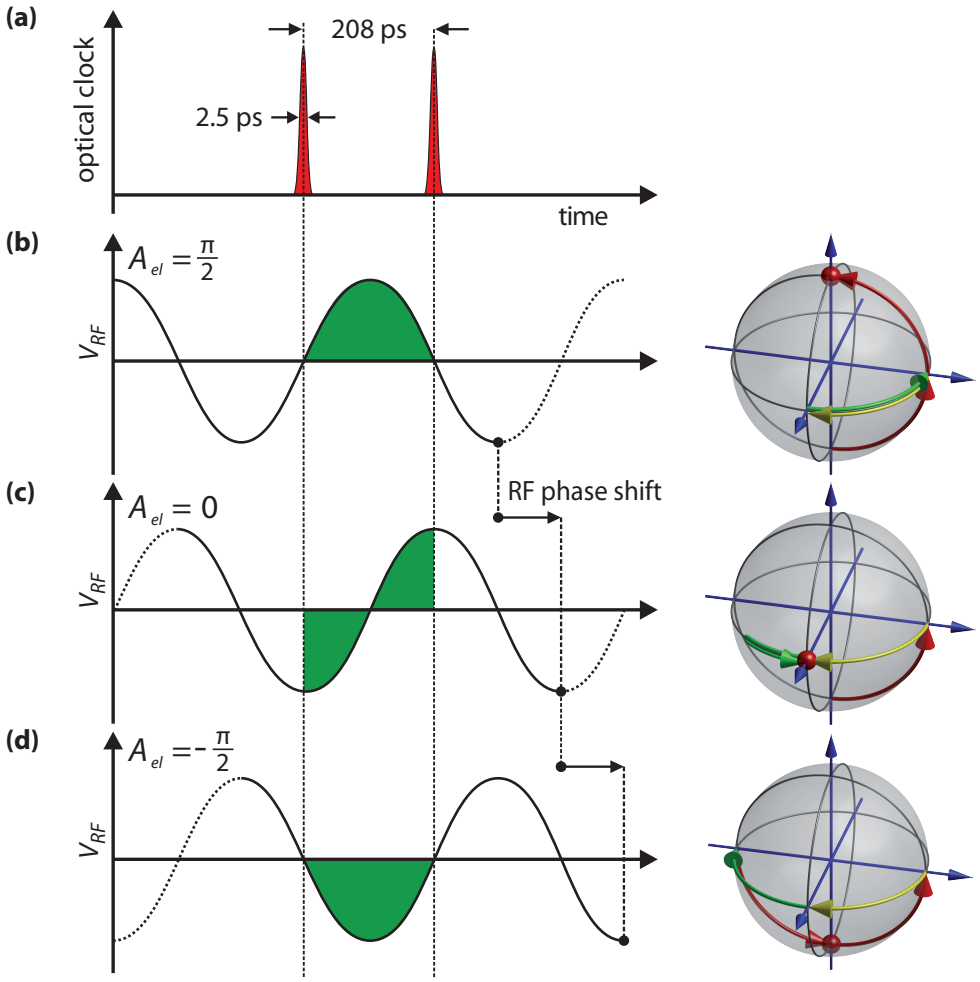

Figure 8.6: Schematic presentation of the electric phase manipulation with an RF signal. (a) The optical clock signal on the time line. (b),(c) and (d) Show different optoelectronic manipulations, as described in the text. On the Bloch spheres, the red and yellow arrows indicate the coherent optical manipulations and the constant offset phase shift, respectively. The green arrows describe the coherent manipulations for different pulse areas A_{el} as sketched along the time line. The final stat of the qubit is indicated by the red ball on each Bloch sphere.

In figure 8.6 a detailed description of the experiment is presented. Therein, the optical clock, consisting of two in-phase $\pi/2$ laser pulses, results in constructive quantum interference, if the phase of the resonant quantum system remains unchanged. This is *not* a fundamental requirement of the experiment, because as a phase shift between the two laser pulses can be compensated by a static quantum phase shift by a constant bias voltage. However, this condition makes it easier to explain the experiment.

In order to achieve a higher sensitivity for small phase shifts of coherent electric manipulation, an additional constant phase shift is introduced. It is induced by a static offset voltage V_{offset}, which leads to an additional phase shift of $-\pi/2$ ($V_{offset} = -2.75$ mV in this case). This phase shift is illustrated on the Bloch spheres by yellow arrows. Essentially, this can regarded as a shift of the operation point of the quantum device to a point where the derivation of the PC signal has a maximum (or minimum). The same effect can be achieved by introducing a $\pi/2$ phase shift between the two laser pulses.

In the situation shown in figure 8.6b, the positive half-wave of the RF signal is located between the two laser pulses. Hence, the quantum phase shift induced by V_{RF} is maximum. In the shown case, this corresponds to a RF-induced phase shift of $+\pi/2$, which is compensated by the offset phase shift to 0, leading to constructive quantum interference. In the second case (figure 8.6c), the RF-induced phase was changed to zero. Here the Bloch vector is at

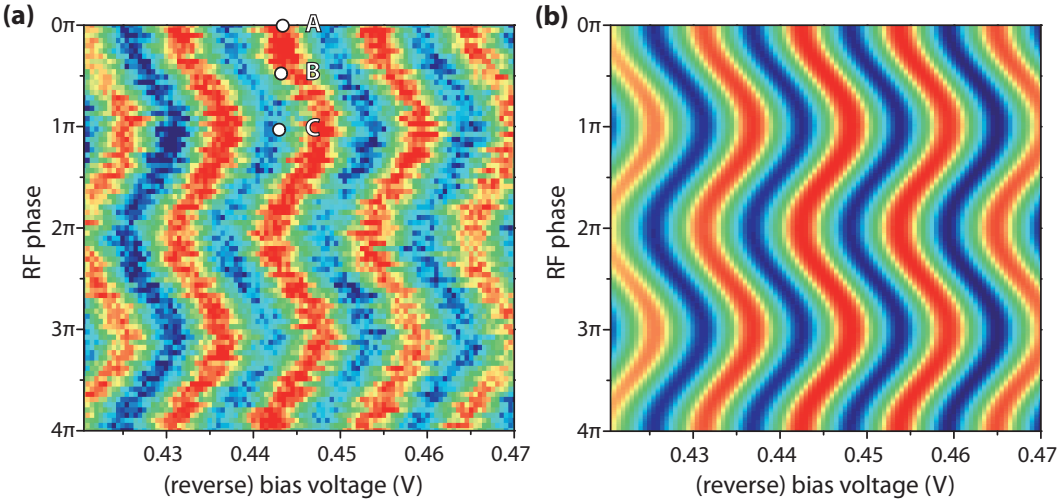

Figure 8.7: (a) The coherent optoelectronic manipulation measured in the photocurrent. The marked points A, B, and C correspond to the situations presented in figure 8.6. These points indicate, that the phase of the system can be inverted by electric manipulation. The minima drift in the data from 0π to 2π can be attributed to a small drift in the laser energy and/or the Michelson interferometer. (b) Corresponding theoretical calculation.

first moved clock-wise, then stopped and moved counter-clock-wise to end up at the starting point. Therefore no additional quantum phase shift is created by the RF voltage. Due to the action of V_{offset}, the total phase shift is $\pi/2$ and the second laser pulse leaves the exciton qubit in the superposition state. In the third case (figure 8.6d), the induced phase shift of – $\pi/2$ adds up with the action of V_{offset}, resulting in a total phase shift of π. Therefore, the quantum interference is destructive, rotating the Bloch vector to $|0\rangle$.

In the experiment shown in figure 8.7a the electric phase is varied from 0 to 4π. For each electric phase setting V_{bias} was tuned from 0.42 to 0.47 V in order to obtain Ramsey fringes. In the resulting color diagram, color coded photocurrent data (red=5.7 pA, blue=4.4 pA) is plotted as a function of V_{bias} and the RF phase ϕ_{RF}. In the experiment V_{RF_0} has been adjusted in such a way, that a sweep of the electric RF phase from 0 to π in fact results in an inversion of the observed Ramsey pattern. This inversion is related to an electrically induced quantum phase shift of π. The observed oscillation amplitude is slightly smaller as compared to the conventional Ramsey experiment due to weak RF-induced heating.

A simulation of the resulting PC response was performed by solving these extended optical Bloch equations from chapter 6. The slight dephasing due to the heating of the sample is modeled in the equations as a pure dephasing term (γ_2^*). The only free fit parameter in this model is the amplitude of the RF signal V_{RF_0}, applied to the gate electrode. Due to the influence of parasitic contributions to the RF impedance of the photodiode (bond wire, internal capacitance), the exact magnitude of V_{RF_0} on the gate electrode remains unknown. By comparing the result of the calculations (figure 8.7b) with the experimental data (figure 8.7a), one finds that the presented model can reproduce the experiment with high accuracy. The best agreement is found for an applied RF amplitude of $V_{RF_0} = 4.4 \pm 0.1$ mV, which corresponds to $1/C_{CM} = 1.17 \pm 0.03$ V ps. This is in very good agreement with the EMC obtained from conventional Ramsey experiments described before.

In summary, the presented new scheme for the coherent optoelectronic manipulation has been verified by the above explained experiment, using an optical clock and a synchronous RF voltage.

8.4 Generalization of the Scheme

8.4.1 Universal Single Qubit Control

The presented concept can be easily extended towards an universal single qubit control. To explain this, the laser pulses and the electrical pulse in the scheme in figure 8.3 is decomposed into single gate operations. The two $\pi/2$ laser pulses represent Hadamard gate operations. The second Hadamard gate is thereby utilized for the quantum interference experiment. As demonstrated experimentally, the electric gate pulse represents an arbitrary phase shifter gate, whereas the phase angle can be controlled by the electric pulse area. It is of course not necessary, that the gates are used is this particular order. For a functional quantum operation, these gate might be applied in any order and might be repeated several times.

From an theoretical point of view, it is trivial that thereby an universal single qubit control can be constructed. As mentioned in chapter 3, an universal single qubit control can be achieved by a finite (but potentially high) number of Hadamard (the $\pi/2$ laser pulse) and $\pi/8$ phase shifter gates (which requiring only an appropriate electric pulse). Due to the fact, that the phase angle can be easily controlled by the electric pulse area, it is possible to achieve the universal control with a sequence of only two Hadamard gates and two phase gates. One possible sequence is presented in figure 8.8. The first Hadamard gate turns the Bloch vector on the equator. The following phase gate rotates the Bloch vector along the equator, so that the second Hadamard gate can reach every height on the Bloch sphere. A second phase shifter gate can now reach ever point on the Bloch sphere on this height. So, by controlling only the two electrical phase gates, it is possible to reach every point on the Bloch sphere, which is equivalent to an universal coherent control of a single qubit.

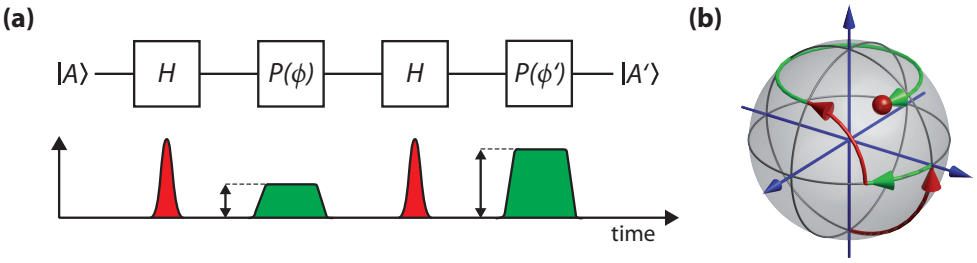

Figure 8.8: (a) Sequence for an universal single qubit control, using the coherent electric manipulation as an arbitrary phase shifter quantum gate. (b) Corresponding, exemplary trajectory of the Bloch vector.

8.4.2 Scaling the Approach

One of the most remarkable features of the presented scheme is its scalability. For instance, one can imagine a qubit register, in which the phase of each qubit is coherently controlled by an individual electric signal while all qubits are clocked by the same optical excitation. This is a big advantage over an individual optical control, which is much more difficult to achieve.

Furthermore, the electric control of the eigenenergies of the qubits, whereby two neighboring qubits can be brought into resonance. Although the exact concept of a two-qubit gate has to be developed in the future, the resonant coupling of two qubits is a fundamental step towards two-qubit gates, for example a quantum CNOT or SWAP gate.

9 Conclusion and Outlook

Quantum information is a rapidly growing field and new theoretical and experimental concepts are developed by research groups all over the world. A major topic is thereby the precise coherent state control, which is a fundamental requirement for the implementation of quantum devices.

In this work, a new scheme for the coherent optoelectronic control of an exciton qubit has been described and experimentally demonstrated. It was shown, that it is possible to manipulate the quantum phase of an optically clocked exciton qubit by applying an electric RF signal. Besides the experimental verification of the approach, a theoretical model of the exciton two-level system was developed and compared to the experimental data, yielding an outstanding coincidence. The model is based on the optical Bloch equations and includes the two-step relaxation mechanism, which is characteristic for the tunneling of the QD exciton in a photodiode.

To confirm the theoretical approach, previously developed experiments were also compared to the model. Thereby, the model allows for a more detailed analysis of the previous results, in particular, the evaluation of the heavy-hole tunneling time from the cw saturation spectroscopy is now more reliable. Moreover, a detailed analysis of the excitation dependent damping of the Rabi-oscillations at low temperature was given in the context of the theoretical model. At this time, the results seem to be contradictory to recent results of the group of M. Skolnick. Thus, further experiments have to be carried out, focussing on Rabi oscillations at high pulse areas and at different temperatures or excited with shaped laser pulses.

In this thesis the coherent manipulation of an exciton qubit by optoelectronic control has been proven. Anyhow the new optoelectronic quantum gate can be further optimized. The next step is the improvement of the RF-properties of the QD photodiode, enabling the coherent electric control with short electric pulses. Very likely, the pulse width can be reduced to less than 100 ps by using a MSM-photodiode for the pulse creation and an appropriate QD photodiode design. Furthermore, an integrated “on-chip” creation of the electric control signal can be considered.

In the future, the proposed scalability of the new concept has to be evaluated, which will require a precise lithography to contact two nearby QDs separately. The long-term objective in this context will be to couple to neighbored exciton qubits. Although it is not clear how this goal can be achieved, the individual control of the energies of the qubits by an applied electric gate signal will play an important role.

Quantum key distribution for secure communication is an interesting application in quantum information. For long-distance quantum communication a quantum repeater is required, in order to avoid decoherence of the transmitted quantum signal. A key task for the develop-

ment of such a device is the interconversion of the quantum state of a photon to a stationary qubit. The exciton qubit system provides an excellent coupling the photons, and basic concepts for the interconversion have been recently proposed in the master thesis of D. Mantei and are going to be patented. The further development of these concepts will be an important task in the future.

The principles of the new scheme are not limited to the exciton qubit. Thus, a transfer of the concept to a qubit system which provides longer coherence times, for example a single electron spin, is a worthwhile objective.

In addition, CdSe/ZnSe QD photodiodes have been introduced in this thesis. This kind of photodiodes may provide advantages in certain aspects as compared to InGaAs/GaAs QD photodiodes. The CdSe/ZnSe material system provides higher confinement and Coulomb correlation energies than the InGaAs/GaAs systems and possess the potential for coherent operation at elevated temperatures. The results from the voltage dependent PL indicate, that the QD photodiode is in principle functional. However, the material system is not as easy to handle as the traditional InGaAs/GaAs system, regarding processing and spectroscopy.

Nevertheless, taking into account the very recent results, which will be presented by M. Panfilova, it seems possible to perform experiments in the photocurrent regime. Although it is not clear, whether excitons in CdSe QDs will provide longer coherence times at elevated temperature than III-V semiconductor systems, the research on the CdSe/ZnSe material system might deliver some interesting results helping to understand the decoherence mechanisms.

The presented scheme for the coherent optoelectronic manipulation of exciton qubits is an innovative and fundamental method for the quantum state control. It opens up for new promising concepts in the area of quantum information research.

Symbols and Abbreviations

Symbols

A_{el}	electric pulse area
C_{CM}	coherent manipulation coefficent
δ	detuning between laser energy and QD-resonance ($\delta = \omega_{laser} - \omega_{01}$)
e	representation for an electron or the elementary charge (1.6022×10^{-19} C)
$\boldsymbol{F}$	electric field
f_{laser}	repetition frequency of the laser (80 MHz)
Γ	linewidth
Γ_0	natural linewidth
h	PLANCK's constant (4.1357×10^{-15} eVs)
$\hbar$	$h/2\pi$ (6.5821×10^{-16} eVs)
hh	heavy-hole
λ	wavelength
$\boldsymbol{\mu}$	dipole moment
Ω, Ω_0	RABI-frequency (on resonance)
ω	angular frequency of the laser radiation or the optical transition
ν	frequency of the laser radiation or the optical transition
ϕ	phase angle
P	(optical) excitation intensity
$\widetilde{P}$	standardized excitation intensity
T_1	life time
T_2	dephasing time
T_2^*	time scale of pure dephasing (no life time induced dephasing)
Θ	(optical) pulse area
u	dispersive component of the BLOCH-vector
v	absorptive component of the BLOCH-vector
w	occupation component of the BLOCH-vector
V_{bias}	bias voltage of the photo diode
V_{res}	bias voltage at the resonance
V_{CM}	coherent manipulation voltage
X^-	negative charged exciton
X	neutral uncharged ground state exciton
X^+	positive charged exciton
$2X$	biexciton (neutral, uncharged, ground state)

Abbreviations

AFM	atomic force microscope
cw	continuous excitation (continuous wave)
FSS	fine structure splitting
FWHM	full width half maximum
MBE	molecular beam epitaxy
NA	numerical aperture
PC	photocurrent (spectroscopy)
PL	photoluminescence (spectroscopy)
PLE	photoluminescence-excitation (spectroscopy)
QCSE	quantum confined Stark effect
QD	quantum dot
RF	radio frequency
RHEED	reflection high energy electron diffraction
TEM	transmission electron microscope
WL	wetting layer

Bibliography

[1] R. Feynman, *There's plenty of room at the bottom*, Annual meeting of the American Physical Society, Caltech, Pasadena, CA (1959)

[2] intel Corp., *Introduction to Intel's 32nm Process Technology*, Press release, <http://download.intel.com/pressroom/kits/32nm/westmere/Intel_32nm_Overview.pdf>, (2009)

[3] intel Corp., *Intel Developer Forum 22nm News Facts Sheet*, Press release, <http://download.intel.com/pressroom/kits/events/idffall_2009/pdfs/22nm_factsheet.pdf>, (2009)

[4] J. R. Arthur, Jr., *Interaction of Ga and As_2 Molecular Beams with GaAs Surfaces*, J. Appl. Phys. **39**, 4032 (1968)

[5] R. Dingle, W. Wiegmann, and C. Henry, *Quantum States of Confined Carriers in Very Thin $Al_xGa_{1-x}As$-GaAs-$Al_xGa_{1-x}As$ Heterostructures*, Phys. Rev. Lett. **33**, 827–830 (1974)

[6] K. Klitzing, G. Dorda, and M. Pepper, *New method for high-accuracy determination of the fine-structure constant based on quantized Hall resistance*, Phys. Rev. Lett. **45**, 494–497 (1980)

[7] Y. Arakawa and H. Sakaki, *Multidimensional quantum well laser and temperature dependence of its threshold current*, Appl. Phys. Lett. **40**, 939 (1982)

[8] J. Lott, N. Ledentsov, V. Ustinov, N. Maleev, A. Zhukov, A. Kovsh, M. Maximov, B. Volovik, Z. Alferov, and D. Bimberg, *InAs-InGaAs quantum dot VCSELs on GaAs substrates emitting at 1.3μm*, Electronics Letters **36**, 1384–1385 (2000)

[9] M. Pelton and Y. Yamamoto, *Ultralow threshold laser using a single quantum dot and a microsphere cavity*, Phys. Rev. A **59**, 2418–2421 (1999)

[10] V. Ryzhii, *The theory of quantum-dot infrared phototransistors*, Semicond. Sci. Tech. **11**, 759–765 (1996)

[11] R. Laghumavarapu, A. Moscho, A. Khoshakhlagh, M. El-Emawy, L. Lester, and D. Huffaker, *GaSb/GaAs type II quantum dot solar cells for enhanced infrared spectral response*, Appl. Phys. Lett. **90**, 173125 (2007)

[12] E. A. Zibik, T. Grange, B. A. Carpenter, N. E. Porter, R. Ferreira, G. Bastard, D. Stehr, S. Winnerl, M. Helm, H. Y. Liu, M. Skolnick, and L. R. Wilson, *Long lifetimes of quantum-dot intersublevel transitions in the terahertz range*, Nature Materials **8**, 803 (2009)

[13] M. Nielsen, *Quantum Computation and Quantum Information*, Cambridge University Press (2000)

[14] L. Vandersypen, M. Steffen, G. Breyta, C. Yannoni, M. Sherwood, and I. Chuang, *Experimental realization of Shor's quantum factoring algorithm using nuclear magnetic resonance*, Nature **414**, 883–887 (2001)

[15] C. Bennett and G. Brassard, *Quantum cryptography: Public key distribution and coin tossing*, Proceedings of IEEE International Conference on Computers, Systems and Signal Processing **175**, (1984)

[16] L. Vandersypen, *Spin based quantum computing in nanostructures*, DPG Physics School on Quantum information and simulation, Bad Honnef (2007)

[17] E. Klarreich, *Biologists join the dots*, Nature **413**, 450–452 (2001)

[18] F. Findeis, *Optical spectroscopy on single self-assembled quantum dots*, PhD thesis, TU München (2001)

[19] A. Yacoby, M. Heiblum, D. Mahalu, and H. Shtrikman, *Coherence and phase sensitive measurements in a quantum dot*, Phys. Rev. Lett. **74**, 4047–4050 (1995)

[20] J. Elzerman, R. Hanson, L. V. Beveren, B. Witkamp, L. Vandersypen, and L. Kouwenhoven, *Single-shot read-out of an individual electron spin in a quantum dot*, Nature **430**, 431–435 (2004)

[21] M. Dahan, S. Levi, C. Luccardini, P. Rostaing, B. Riveau, and A. Triller, *Diffusion Dynamics of Glycine Receptors Revealed by Single-Quantum Dot Tracking*, Science **302**, 442 (2003)

[22] C. Arens, N. Roussau, D. Schikora, and K. Lischka, *Colloidal nanocrystals integrated in epitaxial nanostructures: structural and optical properties*, phys. stat. sol. (c) **3**, 861–864 (2006)

[23] I. N. Stranski and L. Krastanow, *Zur Theorie der orientierten Ausscheidung von Ionenkristallen aufeinander*, Sitzungsberichte der Akademie der Wissenschaften in Wien, Mathematisch-naturwissenschaftliche Klasse Abteilung IIb 146 (1-10), 797 (1937)

[24] M. Mehta, D. Reuter, A. Melnikov, A. D. Wieck, and A. Remhof, *Site-selective growth of self-assembled InAs quantum dots on focused ion beam patterned GaAs*, Physica E **40**, 2034–2036 (2008)

[25] D. Bimberg, *Semiconductor Nanostructures*, Springer (2008)

[26] A. Wojs, P. Hawrylak, S. Fafard, and L. Jacak, *Electronic structure and magneto-optics of self-assembled quantum dots*, Phys. Rev. B **54**, 5604–5608 (1996)

[27] S. Reimann and M. Manninen, *Electronic structure of quantum dots*, Rev. Mod. Phys. **74**, 1283–1342 (2002)

[28] P. Hawrylak, *Excitonic artificial atoms: Engineering optical properties of quantum dots*, Phys. Rev. B **60**, 5597–5608 (1999)

[29] S. M. de Vasconcellos, P. Ester, L. Lackmann, M. Hübner, M. Bichler, and A. Zrenner, *Dephasing Properites of Excited States in InGaAs Quantum Dots*, ICPS-28 (2008)

[30] V. Kulakovskii, G. Bacher, R. Weigand, T. Kümmell, A. Forchel, E. Borovitskaya, K. Leonardi, and D. Hommel, *Fine structure of biexciton emission in symmetric and asymmetric CdSe/ZnSe single quantum dots*, Phys. Rev. Lett. **82**, 1780–1783 (1999)

[31] T. Meier, *Coherent Semiconductor Optics*, Springer (2006)

[32] Q. Xie, J. Brown, R. Jones, J. V. Nostrand, and K. Leedy, *Growth of vertically self-organized InGaAs quantum dots with narrow inhomogeneous broadening*, Appl. Phys. Lett. **76**, 3082–3084 (2000)

[33] M. Mehta, *Intentionally positioned self-assembled InAs quantum dots in a electroluminscent p-i-n-junction diode*, privat communication (2009)

[34] R. Schmidt, U. Scholz, M. Vitzethum, R. Fix, C. Metzner, P. Kailuweit, D. Reuter, A. Wieck, M. C. Huebner, S. Stufler, A. Zrenner, S. Malzer, and G. Dohler, *Fabrication of genuine single-quantum-dot light-emitting diodes*, Appl. Phys. Lett. **88**, 121115 (2006)

[35] P. Ester, *Coherent Properties of Singe Quantum Dot Transitions and Single Photon Emission*, PhD thesis, Universität Paderborn (2008)

[36] H. Htoon, T. Takagahara, D. Kulik, O. Baklenov, A. Holmes, and C. Shih, *Interplay of Rabi oscillations and quantum interference in semiconductor quantum dots*, Phys. Rev. Lett. **88**, 087401 (2002)

[37] R. Melet, V. Voliotis, A. Enderlin, D. Roditchev, X. L. Wang, T. Guillet, and R. Grousson, *Resonant excitonic emission of a single quantum dot in the Rabi regime*, Phys. Rev. B **78**, 073301 (2008)

[38] S. Seidl, M. Kroner, K. Karrai, and R. J. Warburton, *Voltage-controlled optics of a quantum dot*, Phys. Rev. Lett. (2004)

[39] S. Seidl, M. Kroner, P. Dalgarno, A. Högele, J. Smith, M. Ediger, B. Gerardot, J. Garcia, P. Petroff, and K. Karrai, *Absorption and photoluminescence spectroscopy on a single self-assembled charge-tunable quantum dot*, Phys. Rev. B **72**, 195339 (2005)

[40] N. Bonadeo, A. Lenihan, G. Chen, J. Guest, D. Steel, D. Gammon, D. Katzer, and D. Park, *Single quantum dot states measured by optical modulation spectroscopy*, Appl. Phys. Lett. **75**, 2933–2935 (1999)

[41] P. Borri and W. Langbein, *Four-wave mixing dynamics of excitons in InGaAs self-assembled quantum dots*, J. Phys.: Condens. Mat. **19**, 295201 (2007)

[42] P. Borri, W. Langbein, S. Schneider, U. Woggon, R. Sellin, D. Ouyang, and D. Bimberg, *Rabi oscillations in the excitonic ground-state transition of InGaAs quantum dots*, Phys. Rev. B **66**, 81306 (2002)

[43] W. Langbein and B. Patton, *Heterodyne spectral interferometry for multidimensional nonlinear spectroscopy of individual quantum systems*, Opt. lett. **31**, 1151 (2006)

[44] W. Langbein and B. Patton, *Microscopic measurement of photon echo formation in groups of individual excitonic transitions*, Phys. Rev. Lett. **95**, (2005)

[45] F. Findeis, M. Baier, E. Beham, and A. Zrenner, *Photocurrent and photoluminescence of a single self-assembled quantum dot in electric fields*, Appl. Phys. Lett. (2001)

[46] P. W. Fry, I. E. Itskevich, S. R. Parnell, J. J. Finley, L. R. Wilson, K. L. Schumacher, D. J. Mowbray, M. Skolnick, M. Al-Khafaji, A. G. Cullis, M. Hopkinson, J. C. Clark, and G. Hill, *Photocurrent spectroscopy of InAs/GaAs self-assembled quantum dots*, Phys. Rev. B **62**, 16784–16791 (2000)

[47] S. Benner and H. Haug, *Influence of external electric and magnetic fields on the excitonic absorption spectra of quantum-well wires*, Phys. Rev. B **47**, 15750–15750 (1993)

[48] T. Arakawa, Y. Kato, F. Sogawa, and Y. Arakawa, *Photoluminescence studies of GaAs quantum wires with quantum confined Stark effect*, Appl. Phys. Lett. **70**, 646 (1997)

[49] D. Miller, D. Chemla, T. Damen, T. Wood, C. Burrus, A. Gossard, and W. Wiegmann, *Band-edge electroabsorption in quantum well structures: The quantum-confined Stark effect*, Phys. Rev. Lett. **53**, 2173–2176 (1984)

[50] D. Miller, D. Chemla, T. Damen, A. Gossard, W. Wiegmann, T. Wood, and C. Burrus, *Electric field dependence of optical absorption near the band gap of quantum-well structures*, Phys. Rev. B **32**, 1043–1060 (1985)

[51] C. Weisbuch, *Quantum Semiconductor Structures*, Academic Press (1991)

[52] J. Seufert, M. Obert, M. Scheibner, N. Gippius, G. Bacher, A. Forchel, T. Passow, K. Leonardi, and D. Hommel, *Stark effect and polarizability in a single CdSe/ZnSe quantum dot*, Appl. Phys. Lett. **79**, 1033–1035 (2001)

[53] S. Ritter, P. Gartner, N. Baer, and F. Jahnke, *Anomalous Stark effect in semiconductor quantum dots*, Phys. Rev. B **76**, 165302 (2007)

[54] S. M. de Vasconcellos, A. Pawlis, C. Arens, M. Panfilova, A. Zrenner, D. Schikora, and K. Lischka, *Exciton spectroscopy on single CdSe/ZnSe quantum dot photodiodes*, Microelectron. J. **40**, 215–217 (2009)

[55] A. Hogele, S. Seidl, M. Kroner, K. Karrai, R. J. Warburton, B. Gerardot, and P. M. Petroff, *Voltage-controlled optics of a quantum dot*, Phys. Rev. Lett. **93**, 217401 (2004)

[56] F. Findeis, M. Baier, A. Zrenner, and M. Bichler, *Optical excitations of a self-assembled artificial ion*, Phys. Rev. B, (2001)

[57] P. A. Dalgarno, J. M. Smith, J. McFarlane, B. D. Gerardot, K. Karrai, A. Badolato, P. M. Petroff, and R. J. Warburton, *Coulomb interactions in single charged self-assembled quantum dots: Radiative lifetime and recombination energy*, Phys. Rev. B **77**, 245311 (2008)

[58] A. Shabaev, E. A. Stinaff, A. S. Bracker, D. Gammon, A. L. Efros, V. L. Korenev, and I. Merkulov, *Optical pumping and negative luminescence polarization in charged GaAs quantum dots*, Phys. Rev. B **79**, 035322 (2009)

[59] Snow, B. Shanabrook, D. Katzer, and D. Park, *Fine structure splitting in the optical spectra of single GaAs quantum dots*, Phys. Rev. Lett. (1996)

[60] M. Bayer, A. Kuther, A. Forchel, A. Gorbunov, V. Timofeev, F. Schafer, J. Reithmaier, T. Reinecke, and S. Walck, *Electron and hole g factors and exchange interaction from studies of the exciton fine structure in In0.60Ga0.40As quantum dots*, Phys. Rev. Lett. **82**, 1748–1751 (1999)

[61] D. Bouwmeester, *The Physics of Quantum Information*, Springer (2000)

[62] G. P. Berman, G. D. Doolen, R. Mainieri, and V. I. Tsifrinovich, *Introduction to Quantum Computers*, World Scientific Publishing Company (1998)

[63] G. Jaeger, *Quantum Information*, Springer (2007)

[64] P. Benioff, *Quantum mechanical models of Turing machines that dissipate no energy*, Phys. Rev. Lett. (1982)

[65] R. Feynman, *Simulating physics with computers*, International Journal of Theoretical Physics, (1982)

[66] R. Feynman, *Quantum mechanical computers*, Foundations of Physics, (1986)

[67] D. Deutsch, *Quantum theory, the Church-Turing principle and the universal quantum computer*, Proc. Roy. Soc. Lond. A, 97–117 (1985)

[68] D. Deutsch, *Quantum theory as a universal physical theory*, International Journal of Theoretical Physics **24**, 1 (1985)

[69] D. Deutsch and R. Jozsa, *Rapid solution of problems by quantum computation*, Proceedings: Mathematical and Physical Sciences, (1992)

[70] P. Shor, *Algorithms for quantum computation: Discrete log and factoring*, Proceedings of the 35th Annual Symposium on the Foundations of Computer Science, (1994)

[71] P. Shor, *Polynomial-time algorithms for prime factorization and discrete logarithms on a quantum computer*, SIAM Review, (1999)

[72] B. Schumacher, *Quantum Coding*, Phys. Rev. A **51**, 2738–2747 (1995)

[73] Y. Shi, *Both Toffoli and controlled-NOT need little help to do universal quantum computation*, Arxiv preprint quant-ph, (2002)

[74] A. Barenco, C. Bennett, and R. Cleve, *Elementary gates for quantum computation*, Phys. Rev. A, (1995)

[75] D. DiVincenzo, *Two-bit gates are universal for quantum computation*, Phys. Rev. A, (1995)

[76] S. Lloyd, *Almost any quantum logic gate is universal*, Phys. Rev. Lett. (1995)

[77] R. Cleve, A. Ekert, C. Macchiavello, and M. Mosca, *Quantum algorithms revisited*, P Roy Soc Lond A Mat **454**, 339–354 (1998)

[78] L. Grover, *A fast quantum mechanical algorithm for database search*, Proceedings of the twenty-eighth annual ACM symposium on Theory of computing, 219 (1996)

[79] T. Kleinjung, *On polynomial selection for the general number field sieve*, Math Comput **75**, 2037–2047 (2006)

[80] C. H. Bennett and G. Brassard, *Quantum public key distribution system*, IBM Tech. Discl. Bull. **28**, 3153 (1985)

[81] H. Briegel, W. Dur, J. Cirac, and P. Zoller, *Quantum repeaters: The role of imperfect local operations in quantum communication*, Phys. Rev. Lett. **81**, 5932–5935 (1998)

[82] L. Childress, J. Taylor, A. Sorensen, and M. Lukin, *Fault-tolerant quantum communication based on solid-state photon emitters*, Phys. Rev. Lett. **96**, 070504 (2006)

[83] P. van Loock, T. Ladd, K. Sanaka, F. Yamaguchi, K. Nemoto, W. Munro, and Y. Yamamoto, *Hybrid quantum repeater using bright coherent light*, Phys. Rev. Lett. **96**, 240501 (2006)

[84] L. Jiang, J. M. Taylor, K. Nemoto, W. J. Munro, R. V. Meter, and M. D. Lukin, *Quantum repeater with encoding*, Phys. Rev. A **79**, 032325 (2009)

[85] S. Stufler, P. Ester, A. Zrenner, and M. Bichler, *Quantum optical properties of a single InxGa1-xAs-GaAs quantum dot two-level system*, Phys. Rev. B **72**, 121301 (2005)

[86] Analog Devices, *AD549 Data Sheet*, (Ultralow Input Bias Current Operational Amplifier, 2008)

[87] J. G. Graeme, *Photodiode Amplifiers: OP AMP Solutions*, (1995)

[88] Maxim, *MAX132 Data Sheet*, (±18-Bit ADC with Serial Interface, 1995)

[89] S. Stufler, *Kohärente optische Eigenschaften einzelner Halbleiter Quantenpunkte*, PhD thesis, Universiät Paderborn (2005)

[90] M. C. Hübner, *Temperaturabhängige Eigenschaften einzelner Halbleiter-Quantenpunkte im kohärenten Regime*, PhD thesis, Universiät Paderborn (2009)

[91] M. Panfilova, PhD thesis, Universiät Paderborn (2010)

[92] D. Schikora, S. Schwedhelm, D. As, K. Lischka, D. Litvinov, A. Rosenauer, D. Gerthsen, M. Strassburg, A. Hoffmann, and D. Bimberg, *Investigations on the Stranski–Krastanow growth of CdSe quantum dots*, Appl. Phys. Lett. **76**, 418 (2000)

[93] B. Patton, W. Langbein, and U. Woggon, *Trion, biexciton, and exciton dynamics in single self-assembled CdSe quantum dots*, Phys. Rev. B **68**, 125316 (2003)

[94] J. Seufert, M. Rambach, G. Bacher, A. Forchel, T. Passow, and D. Hommel, *Single-electron charging of a self-assembled II–VI quantum dot*, Appl. Phys. Lett. **82**, 3946 (2003)

[95] I. Robin, R. Andre, and J. Gérard, *Relation between growth procedure and confinement properties of CdSe/ZnSe quantum dots*, Phys. Rev. B **74**, 155318 (2006)

[96] M. Panfilova, S. Michaelis de Vasconcellos, A. Pawlis, K. Lischka, and A. Zrenner, *Resonant photocurrent-spectroscopy of individual CdSe quantum dots*, Physica E, submitted (2009)

[97] I. I. Rabi, *Space Quantization in a Gyrating Magnetic Field*, Phys. Rev. **51**, 625–654 (1937)

[98] F. Bloch, *Nuclear Induction*, Phys. Rev. **70**, 460 (1946)

[99] W. Vogel and D.-G. Welsch, *Quantum Optics*, 3rd ed., Wiley-VCH (2006)

[100] M. O. Scully and M. S. Zubairy, *Quantum Optics*, Cambridge University Press (1997)

[101] P. Meystre, M. Sargent, and M. Sargent III, *Elements of Quantum Optics*, 2nd, Springer-Verlag Berlin and Heidelberg GmbH & Co. K (1991)

[102] L. Allen and J. H. Eberly, *Optical resonance and two-level atoms*, Dover Publications, Inc., New York (1987)

[103] L. Mandel and E. Wolf, *Optical Coherence and Quantum Optics*, Cambridge University Press (1995)

[104] I. S. Gradshteyn and I. Ryzhik, *Tables of Integrals, Series, and Products*, 6th ed., San Diego, CA: Academic Press (2000)

[105] S. Boyle, A. Ramsay, A. Fox, and M. Skolnick, *Beating of Exciton-Dressed States in a Single Semiconductor InGaAs/GaAs Quantum Dot*, Phys. Rev. Lett. (2009)

[106] The MathWorks Inc., *MATLAB R2009a Manual*, (2009)

[107] E. Beham, *Photostromspektroskopie an einzelnen Quantenpunkten*, PhD thesis, (2003)

[108] S. Stufler, P. Ester, A. Zrenner, and M. Bichler, *Power broadening of the exciton linewidth in a single InGaAs/GaAs quantum dot*, Appl. Phys. Lett. **85**, 4202–4204 (2004)

[109] E. Beham, A. Zrenner, F. Findeis, and M. Bichler, *Nonlinear ground-state absorption observed in a single quantum dot*, Appl. Phys. Lett. (2001)

[110] U. Woggon, *Optical Properties of Semiconductor Quantum Dots (Springer Tracts in Modern Physics)*, Springer (1996)

[111] T. Stievater, X. Li, D. Steel, D. Gammon, D. Katzer, D. Park, C. Piermarocchi, and L. Sham, *Rabi oscillations of excitons in single quantum dots*, Phys. Rev. Lett. **87**, 133603 (2001)

[112] H. Takagi, T. Nakaoka, K. Watanabe, N. Kumagai, and Y. Arakawa, *Coherently driven semiconductor quantum dot at a telecommunication wavelength*, Opt. Express. **16**, 13949–13954 (2008)

[113] H. Kamada, H. Gotoh, J. Temmyo, T. Takagahara, and H. Ando, *Exciton Rabi oscillation in a single quantum dot*, Phys. Rev. Lett. **87**, 246401 (2001)

[114] B. Patton, U. Woggon, and W. Langbein, *Coherent control and polarization readout of individual excitonic states*, Phys. Rev. Lett. **95**, 266401 (2005)

[115] Q. Wang, A. Muller, P. Bianucci, E. Rossi, Q. Xue, T. Takagahara, C. Piermarocchi, A. MacDonald, and C. Shih, *Decoherence processes during optical manipulation of excitonic qubits in semiconductor quantum dots*, Phys. Rev. B **72**, 035306 (2005)

[116] J. Villas-Boas, S. Ulloa, and A. Govorov, *Decoherence of Rabi oscillations in a single quantum dot*, Phys. Rev. Lett. **94**, 057404 (2005)

[117] A. Zrenner, E. Beham, S. Stufler, F. Findeis, M. Bichler, and G. Abstreiter, *Coherent properties of a two-level system based on a quantum-dot photodiode*, Nature **418**, 612–614 (2002)

[118] J. Förstner, C. Weber, J. Danckwerts, and A. Knorr, *Phonon-assisted damping of Rabi oscillations in semiconductor quantum dots*, Phys. Rev. Lett. **91**, 127401 (2003)

[119] A. Krugel, V. M. Axt, T. Kuhn, P. Machnikowski, and A. Vagov, *The role of acoustic phonons for Rabi oscillations in semiconductor quantum dots*, Appl. Phys. B **81**, 897–904 (2005)

[120] A. Vagov, M. D. Croitoru, V. M. Axt, T. Kuhn, and F. M. Peeters, *High pulse area undamping of Rabi oscillations in quantum dots coupled to phonons*, phys. stat. sol. (b) **243**, 2233–2240 (2006)

[121] A. J. Ramsay, A. V. Gopal, E. M. Gauger, A. Nazir, B. W. Lovett, A. M. Fox, and M. Skolnick, *Excitation-induced-dephasing of quantum dot excitonic Rabi rotations*, arXiv, cond-mat.mes-hall **0903.5278v1**, (2009)

[122] D. Mogilevtsev, A. P. Nisovtsev, S. Kilin, S. B. Cavalcanti, H. S. Brandi, and L. E. Oliveira, *Driving-dependent damping of rabi oscillations in two-level semiconductor systems*, Phys. Rev. Lett. **100**, 017401 (2008)

[123] D. Mogilevtsev, A. P. Nisovtsev, S. Kilin, S. B. Cavalcanti, H. S. Brandi, and L. E. Oliveira, *Non-Markovian damping of Rabi oscillations in semiconductor quantum dots*, J. Phys.: Condens. Mat. **21**, 055801 (2009)

[124] H. Brandi, A. Latge, Z. Barticevic, and L. Oliveira, *Rabi oscillations in two-level semiconductor systems*, Solid State Commun. **135**, 386–389 (2005)

[125] A. Schweiger and G. Jeschke, *Principles of Pulse Electron Paramagnetic Resonance Spectroscopy*, Oxford University Press, New York (2001)

[126] H. Y. Carr, *Effects of Diffusion on Free Precession in Nuclear Magnetic Resonance Experiments*, Phys. Rev. **94**, 630–638 (1954)

[127] R. S. Kolodka, A. J. Ramsay, J. Skiba-Szymanska, P. W. Fry, H. Y. Liu, A. M. Fox, and M. Skolnick, *Inversion recovery of single quantum-dot exciton based qubit*, Phys. Rev. B **75**, 193306 (2007)

[128] S. M. de Vasconcellos, S. Stufler, S. A. Wegner, P. Ester, A. Zrenner, and M. Bichler, *Quantum interferences of a single quantum dot in the case of detuning*, Phys. Rev. B **74**, 081304 (2006)

[129] N. Ramsey, *Experiments with separated oscillatory fields and hydrogen masers*, Reviews of Modern Physics, (1990)

[130] S. Stufler, P. Ester, A. Zrenner, and M. Bichler, *Ramsey fringes in an electric-field-tunable quantum dot system*, Phys. Rev. Lett. **96**, 037402 (2006)

[131] A. Zrenner, S. Stufler, P. Ester, S. M. de Vasconcellos, M. C. Huebner, and M. Bichler, *Recent developments in single dot coherent devices*, phys. stat. sol. (b) **243**, 3696–3708 (2006)

[132] A. Zrenner, P. Ester, S. M. de Vasconcellos, M. C. Huebner, L. Lackmann, S. Stufler, and M. Bichler, *Coherent optoelectronics with single quantum dots*, J. Phys.: Condens. Mat. **20**, 454210 (2008)

[133] P. Ester, S. Stufler, S. M. de Vasconcellos, M. Bichler, and A. Zrenner, *Ramsey fringes in a single InGaAs/GaAs quantum dot*, phys. stat. sol. (b) **243**, 2229–2232 (2006)

List of Publications

1. **Ramsey fringes in a single InGaAs/GaAs quantum dot**
   P. Ester, S. Stufler, ***S. Michaelis de Vasconcellos****, M. Bichler, and A. Zrenner*
   physica status solidi (b) Vol. **243**, Issue 10, p. 2229

2. **Recent developments in single dot coherent devices**
   A. Zrenner, S. Stufler, P. Ester, ***S. Michaelis de Vasconcellos****, M. Hübner, and M.Bichler*
   physica status solidi (b) Vol. **243**, Issue 14, p. 3696

3. **Quantum interferences of a single quantum dot in the case of detuning**
   S. Michaelis de Vasconcellos*, S. Stufler, S.-A. Wegner, P. Ester, A. Zrenner, and M. Bichler*
   Phys. Rev. B **74**, 081304 (2006)

4. **High resolution photocurrent-spectroscopy of a single quantum dot**
   P. Ester, S. Stufler, ***S. Michaelis de Vasconcellos****, M. Bichler, and A. Zrenner*
   physica status solidi (c) Vol **3**, Issue 11, p. 3722 (2006)

5. **Quantum interferences of a single quantum dot in the case of detuning**
   S. Michaelis de Vasconcellos*, S. Stufler, S.-A. Wegner, P. Ester, M. Bichler and A. Zrenner*
   physica status solidi (c) Vol. **3**, Issue 11, p. 3730 (2006)

6. **Single photon emission based on coherent state preparation**
   P. Ester, L. Lackmann, ***S. Michaelis de Vasconcellos****, M. C. Hübner, A. Zrenner, and M. Bichler*
   Appl. Phys. Lett. **91**, 111110 (2007)

7. **p-shell Rabi-flopping and single photon emission in an InGaAs/GaAs quantum dot**
   P. Ester, L. Lackmann, M.C. Hübner, ***S. Michaelis de Vasconcellos****, A. Zrenner and M.Bichler*
   Physica E: Low-dimensional Systems and Nanostructures, Volume **40**, Issue 6, April 2008, Pages 2004-2006

8. **Micro-Raman imaging and micro-photoluminescence measurements of strain in ZnMgSe/ZnSe microdiscs**
   M. Panfilova, A. Pawlis, C. Arens, ***S. Michaelis de Vasconcellos****, G. Berth, K.P. Hüsch, V. Wiedemeier, A. Zrenner and K. Lischka*
   Microelectronics Journal **40**, 221 (2009)

9. **Exciton spectroscopy on single CdSe/ZnSe quantum dot photodiodes**
   ***S. Michaelis de Vasconcellos**, A. Pawlis, C. Arens, M. Panfilova, A. Zrenner, D. Schikora and K. Lischka*
   Microelectronics Journal **40**, 215 (2009)

10. **Resonant photocurrent-spectroscopy of individual CdSe quantum dots**
    *M. Panfilova, **S. Michaelis de Vasconcellos**, A. Pawlis, K. Lischka, A. Zrenner*
    Microelectronics Journal **40**, 215 (2009)

11. **Optoelektronisches Quantengatter (Patent)**
    ***S. Michaelis de Vasconcellos**, A. Zrenner*
    submitted to the German Patent and Trademark Office, Jul. 2009

12. **Resonant photocurrent-spectroscopy of individual CdSe quantum dots**
    *M. Panfilova, **S. Michaelis de Vasconcellos**, A. Pawlis, K. Lischka, A. Zrenner*
    submitted to Physica E (2009), accepted

13. **Coherent optoelectronic control of an exciton**
    ***S. Michaelis de Vasconcellos**, S. Gordon, M. Bichler, T. Meier, A. Zrenner*
    submitted to Nature Photonics (2009)